



Exploration du traitement au laser femtoseconde de supports transparents de nouveaux composants laser

Wendwesen Gebremichael

► To cite this version:

Wendwesen Gebremichael. Exploration du traitement au laser femtoseconde de supports transparents de nouveaux composants laser. Automatique. Université de Bordeaux, 2019. Français. NNT : 2019BORD0082 . tel-02340701

HAL Id: tel-02340701

<https://theses.hal.science/tel-02340701>

Submitted on 31 Oct 2019

HAL is a multi-disciplinary open access archive for the deposit and dissemination of scientific research documents, whether they are published or not. The documents may come from teaching and research institutions in France or abroad, or from public or private research centers.

L'archive ouverte pluridisciplinaire **HAL**, est destinée au dépôt et à la diffusion de documents scientifiques de niveau recherche, publiés ou non, émanant des établissements d'enseignement et de recherche français ou étrangers, des laboratoires publics ou privés.

UNIVERSITÉ DE BORDEAUX
CENTRE LASERS INTENSES ET APPLICATIONS (CELIA)

THÈSE

présentée en vue d'obtenir le grade de DOCTEUR
spécialité "Lasers, Matière et Nanosciences"
par

Wendwesen GEBREMICHAEL

EXPLORATION DU TRAITEMENT AU LASER FEMTOSECONDE DE SUPPORTS TRANSPARENTS DE NOUVEAUX COMPOSANTS LASER

(Exploring Femtosecond Laser Processing of Transparent Media for
Novel Laser Components)

Date de soutenance prévue le 06 Juin 2019 devant le jury composé de :

Dr. Olivier UTEZA	LP3 - Lasers, Plasmas et Procédés Photoniques Aix-Marseille Université, Marseille, France	(Rapporteur)
Dr. rer. nat. Jörn BONSE	Bundesanstalt für Materialforschung und -prüfung (BAM), Berlin, Germany	(Rapporteur)
Prof. Jean OBERLÉ	Laboratoire Ondes et Matière d'Aquitaine (LOMA), Université de Bordeaux, Talence, France	(Examineur)
Prof. Peter KAZANSKY	Optoelectronics Research Centre, University of Southampton, Southampton, UK	(Examineur)
Dr. Inka MANEK-HÖNNINGER	Centre Lasers Intenses et Applications (CELIA), Université de Bordeaux, Talence, France	(Co-Directeur)
Prof. Lionel CANIONI	Centre Lasers Intenses et Applications (CELIA), Université de Bordeaux, Talence, France	(Directeur)

Résumé

L'inscription par laser femtoseconde directe dans les cristaux laser offre une nouvelle opportunité de conception et développement de sources laser intégrées. Elle conduit à un prototypage rapide et à un bon rapport coût-efficacité, conformément aux futures feuilles de route de la photonique. Cependant, les défis liés au dépôt d'énergie d'un laser intense dans des milieux transparents et les modifications qui s'ensuivent restent encore des questions ouvertes. Ces défis ont été relevés en partie grâce à une étude minutieuse et systématique des zones modifiées par laser femtoseconde dans les matériaux transparents. Le fluorure de calcium (CaF_2), en raison de sa symétrie cubique et de ses excellentes propriétés de luminescence en tant que cristal laser, a été choisi comme matériaux de référence dans cette thèse. L'inscription laser en régime femtoseconde de guides d'ondes à l'intérieur de ce cristal a été réalisée pour une conception future de source laser intégrée. Pour la première fois, des écritures laser « lisses » et non réciproques ont été observées à l'intérieur de certains échantillons « coupés spécialement » de cristaux de CaF_2 . De plus, un guidage de la lumière dépendant de la polarisation a été identifié et est présenté. Un modèle et une méthode ont été développés pour caractériser quantitativement et qualitativement ces guides d'ondes, en particulier pour les mesures de perte de transmission, ainsi que les cartographies tridimensionnelles de l'indice de réfraction des zones modifiées.

Abstract

Femtosecond laser micromachining inside laser crystals offers a new platform to miniaturize highly compact laser sources. It leads to rapid prototyping and cost-effectiveness in line with the future photonics roadmaps. However, the challenges in relation to an intense laser pulse energy deposition within transparent media and the modifications that follow still remain open-ended questions. These challenges have been addressed with a careful and systematic study of femtosecond modified zones inside transparent materials. Due to its cubic symmetry and excellent luminescence properties as laser crystal, Calcium Fluoride (CaF_2) was selected, and ultrafast laser inscription of waveguides inside this crystal was realized. Smooth and non-reciprocal writings were observed inside certain “specially cut” samples of the CaF_2 crystals for the first time. Additionally, polarization dependent guiding is identified and presented. Furthermore, an authentic model and concept was engaged for the quantitative and qualitative characterization of the waveguides, particularly for the transmission loss measurements and the three-dimensional refractive index mappings of the modified zones.

Dedication

To my mom, family, friends and professors.

Acknowledgements

First and foremost, I praise God, the almighty for giving me the strength to keep going in various phases of my life inspite of the good and the bad, some were blessing and others were lessons. This thesis appears in its present form due to the assistance and guidance of several people. I would, therefore, like to offer my sincere thanks to all of them.

I greatly appreciate my research advisors, Prof. Lionel Canioni and Dr. Inka Manek-Hönninger for their continuous intellectual support, patience and motivation throughout the thesis work. Thank you so much for believing in me until the end. Thank you Lionel for being always present whenever I wanted you and your encouragement which enabled me to escalate beyond my imaginations in every personal, theoretical or experimental steps I embarked on. Inka, thank you for being whenever I needed you despite your busy schedules, for providing me this opportunity and you are more than a supervisor for me.

I would also like to pay great deal of gratitude for my excellent colleagues of Short-pulse Lasers Applications and Materials (SLAM) group under Centre Lasers Intenses et Applications (CELIA) labratory. I am thankful for Dr. Yanick Petit specially for the discussions we have on Chapters 5 and 6, if not for the theoretical discussions and comments you have given me since the beginning, and offcourse I remember Neuchatel. I would also like to thank Prof. Bruno Bousquet for his encouragement and yes I can see now there is a light at the end of the tunnel.

Sophie, Julian and Delphine, when I start the thesis, all I wanted was very good colleagues and good working ambience instead I have close friends now. I would also like to extend my gratitude to Alain, Arthur, Brice, Chang-Hun, Joyce, Laura, Lena, Sonia and Celine. You were all exceptionally nice and friendly to me all the time and it has been a blessing to work and laugh with you.

I would also like to thank Dr. Patrick Mounaix from Laboratoire de l'Intégration du Matériau au Système (IMS) for providing us the CaF_2 samples. Dr. Sylvian Danto, Alexander Fargue and Stanislav Pechev from ICMCB for helping me during polishing, preparation and cytallographic characgterization of the samples.

I am highly in debt for the the support I received from Forschungsinstitut für mineralische und metallische Werkstoffe Edelsteine/Edelmetalle GmbH (FEE) specially Sophie Vernay and her colleagues. Thank you for slicing and preparing the CaF_2 within the framework of an actual R&D project, for free, which was rather very expensive and a risky task given the highly brittle nature of the crystal.

The works presented in the thesis were the result of the collaboration of Association Nationale Recherche Technologie (ANRT) and Amplitude Laser Group, formerly known as Amplitude Systèmes. I am thankful for Dr. Clemens Hönninger, Dr. Guillaume Machinet, Sebastien Courtois and members of the R&D team for the help and assistance you have offered me during my stay at the company.

Finally, this phase of my life journey was exceptionally demanding and had it not been for the love, support, and encouragement I received from my family and friends, I wouldn't have had the strength to complete the task. Thank you Tigist Atbek OKE my mom, Habte Gebremichael (Dad), Tizita Habte Gebremichael, Samuel Siyoum and Selam Habte Gebremichael. I would exceptionally like to thank my friends in Bordeaux for sharing this adventure, specially Eskinder and Selam for welcoming me in to rather a new city. Weyni, Ezana, Thomas and Wedi, you guys are crazy in your own ways and thank you for putting a smile on my face no matter how much struggles I had. At last, I promise to live a fair life that will do justice to the sacrifices and benevolence of everyone surrounding my life.

Table of Contents

RÉSUMÉ	II
ABSTRACT	III
ACKNOWLEDGEMENTS	IV
TABLE OF CONTENTS	VI
SYNOPSIS	IX
NOMENCLATURE	XV
LIST OF FIGURES	XVII
LIST OF TABLES	XXIII
1 INTRODUCTION	1
1.1 MOTIVATION AND AIM	1
2 LASER-MATTER INTERACTION IN CRYSTALS	6
2.1 FUNDAMENTAL PRINCIPLES OF LASER-MATTER INTERACTION	6
2.1.1 <i>Nonlinear Propagation and Filamentation</i>	8
2.1.2 <i>Nonlinear Photon Absorption and Propagation</i>	11
2.1.3 <i>Thermalization and Heat Dissipation</i>	19
2.1.4 <i>Parameters Affecting the Femtosecond Laser-Matter Interaction</i>	22
2.2 TYPES OF MODIFICATIONS IN CRYSTALS	25
2.3 PROPERTIES OF CRYSTALS	27
2.4 CRYSTALS OF INTEREST: ND:YAG AND CaF_2	32
2.5 STATE-OF-THE-ART OF DIRECT LASER WRITING INSIDE CRYSTALS	35

3	EXPERIMENT IN FEMTOSECOND LASER STRUCTURING	38
3.1	EXPERIMENTAL SET-UP	38
3.1.1	<i>High Power Source</i>	38
3.1.2	<i>Beam and Pulse Control</i>	40
3.1.3	<i>3D Trajectory</i>	41
3.1.4	<i>Power and Trajectory Control</i>	41
3.2	PROTOCOL FOR LASER STRUCTURING	41
4	FABRICATION OF WAVEGUIDES	44
4.1	MODIFICATION THRESHOLD AND CRACK FORMATION	44
4.2	WAVEGUIDE INSCRIPTION	46
4.3	SMOOTH MODIFICATIONS AND NON-RECIPROCITY OF DLW INSIDE CaF_2	52
4.3.1	<i>Smooth Modification</i>	55
4.3.2	<i>Non-reciprocity</i>	58
4.4	CONCLUSION	63
5	GUIDING CHARACTERISTICS OF THE WAVEGUIDES	64
5.1	INTRODUCTION TO WAVEGUIDING	64
5.2	GEOMETRIES OF WAVEGUIDES IN CRYSTALS	66
5.3	MODES IN WAVEGUIDES	68
5.3.1	<i>Setup</i>	70
5.3.2	<i>Mode Field Diameter Measurements</i>	74
5.4	TRANSMISSION LOSSES	76
5.4.1	<i>Modeling Guided and Unguided Modes</i>	77
5.4.2	<i>Setup</i>	79
5.4.3	<i>Calculation and Result</i>	80
5.5	POLARIZATION BEHAVIOR OF THE WAVEGUIDES	84
5.6	CONCLUSION	85
6	REFRACTIVE INDEX CHANGE MEASUREMENT OF DOUBLE TRACK CaF_2 WAVEGUIDES	86
6.1	REFRACTIVE INDEX MEASUREMENT TECHNIQUES	86
6.2	PRINCIPLE OF QUADRIWAVE LATERAL SHEARING INTERFEROMETRY (QWLSI)	88
6.3	QWLSI EXPERIMENTAL SETUP	89
6.4	OPD MEASUREMENTS	90
6.5	OPD MEASUREMENTS TO 3D REFRACTIVE INDEX MAP	94
6.5.1	<i>Thickness of Longitudinal Elements</i>	94
6.5.2	<i>Thickness of Lateral Elements</i>	104

6.5.3	<i>3D Refractive Index Change Profile</i>	105
6.6	SIMULATION	107
6.6.1	<i>Method of Simulation</i>	108
6.6.2	<i>Comparison between Experiment and Simulation of Guided Modes</i>	110
6.7	CONCLUSIONS	113
7	CONCLUSION AND FUTURE WORK	114
	APPENDIX A	116
	BIBLIOGRAPHY	124

Synopsis

1 MOTIVATION ET OBJECTIF

Le chapitre 1 introduit le sujet de thèse et son contexte.

2 INTERACTION LASER-MATIERE DANS LES CRISTAUX

Le Chapitre 2 détaille les bases et outils théoriques permettant de comprendre et appréhender « interaction en régime femtoseconde dans les cristaux transparents.

3 EXPÉRIENCE DE STRUCTURATION LASER FEMTOSECONDE

La configuration et le protocole d'inscription par laser femtoseconde sont présentés dans le chapitre 3.

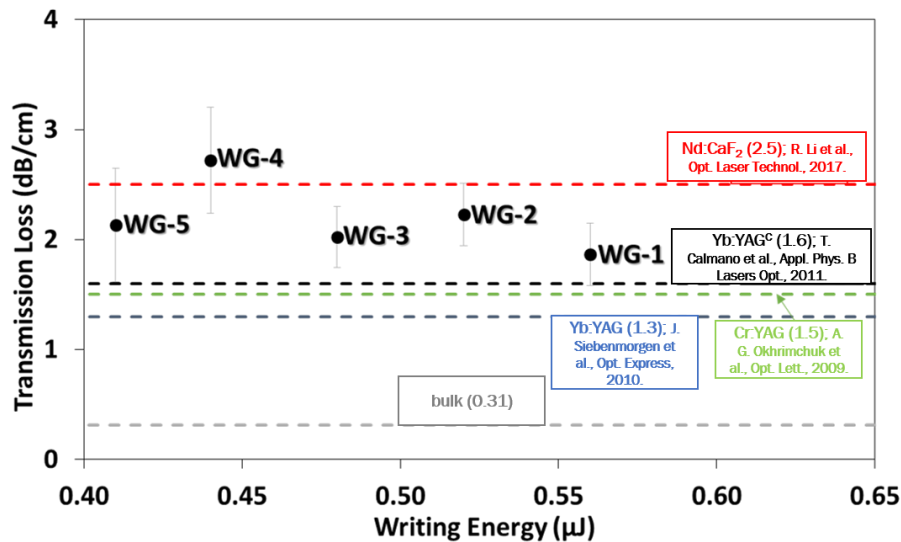
4 FABRICATON DE GUIDES D'ONDES

Le chapitre 4 présente une application de l'inscription laser sur deux échantillons de CaF_2 coupés différemment pour inscrire des guides d'ondes à double piste, abordé aux sections 4.1 et 4.2. Bien que la tâche principale ait été d'identifier les paramètres d'écriture, les échantillons de cristaux qui ont été coupés le long des axes principaux définis présentaient des anomalies, à savoir des modifications lisses et une écriture non réciproque, qui n'ont été observées que très rarement jusqu'ici. Ce point est détaillé à la section 4.3. Dans ce chapitre, bien que la principale motivation soit d'inscrire des guides d'ondes CaF_2 à double piste avec différents paramètres d'écriture, nous avons observé une modification non réciproque et lisse des échantillons coupés le long des principaux axes cristallographiques. La méthode d'approche

expérimentale et analytique pour identifier la fenêtre de modification à l'intérieur de ces échantillons a été discutée. De fortes modifications lisses ont été observées lorsque la direction d'écriture est parallèle à la direction de polarisation en général, et des fenêtres d'inscription plus larges sont obtenues le long de l'axe x cristallographiques en particulier. En comparaison, une forte écriture non réciproque a été observée le long de l'axe cristallographique y.

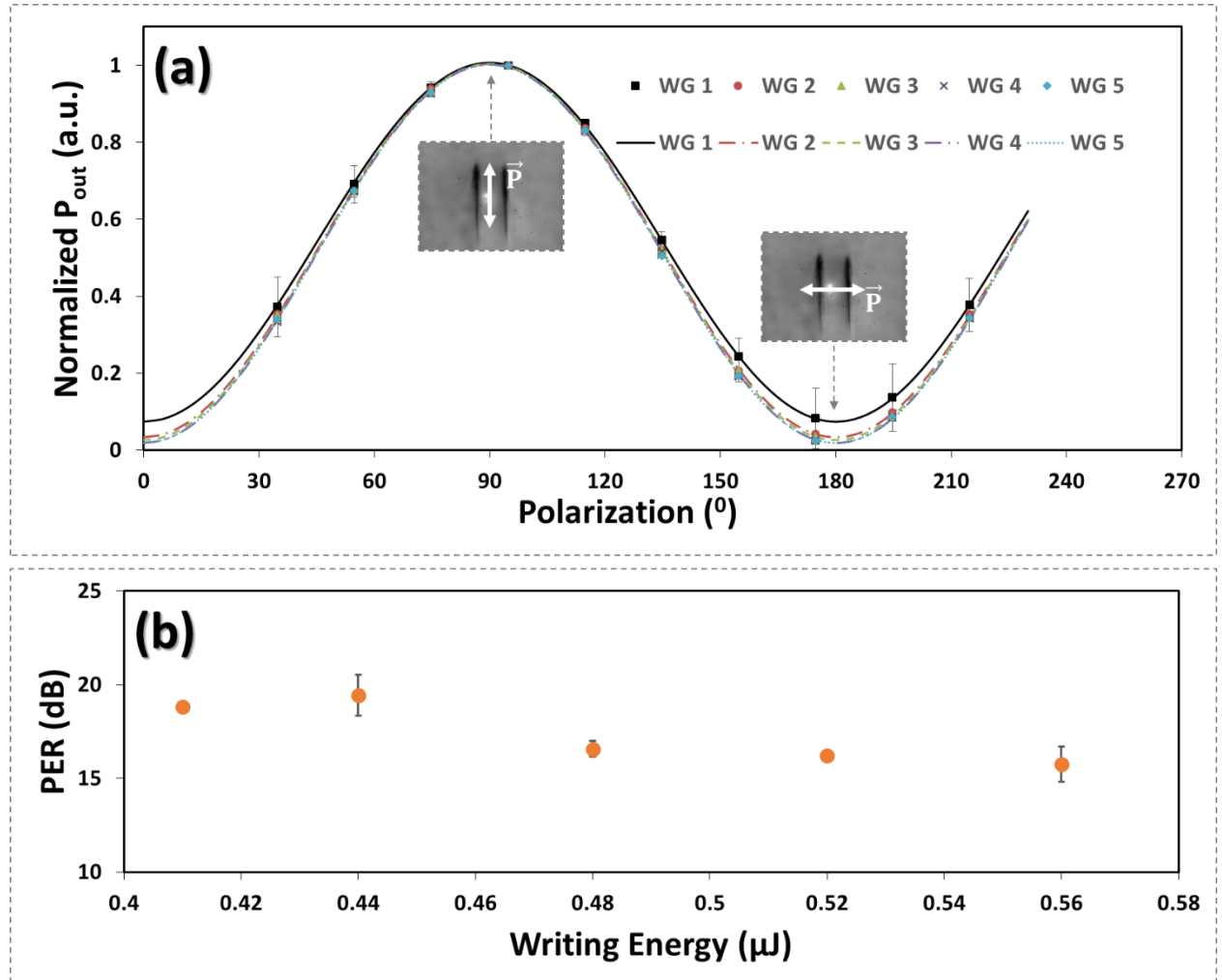
5 PROPRIETES DES GUIDES D'ONDES

Dans le chapitre 5, la théorie et la démonstration expérimentale des mécanismes de guidage d'onde sont décrites. La perte de transmission des modes guidés à l'intérieur des guides d'onde à double ligne induits par laser femtoseconde dans le CaF₂ est exploitée. La première partie du chapitre donne un aperçu des paramètres de guidage suivant différentes géométries de guides d'ondes à l'intérieur des matériaux cristallins dans les sections 5.1 et 5.2, respectivement. La section 5.3 traite de la théorie et de la caractérisation des modes guidés et présente les profils des modes en champ proche des guides d'ondes inscrits. En outre, la section 5.4 traite d'un dispositif simple de mesure de la perte de transmission avec sa modélisation théorique, et d'une comparaison des résultats avec des mesures antérieures obtenus par d'autres groupes. Enfin, la section 5.5 présente la dépendance de polarisation des guides d'ondes.



Transmission loss (dB/cm) of the CaF₂ undoped crystal double-track waveguides in comparison with some previously reported transmission losses where red is a Nd:CaF₂ crystal [75]; black is a Yb:YAG ceramics [101]; green is a Cr:YAG crystal [109] and blue is a Yb:YAG crystal [106]. The gray line at 0.31 dB/cm is the transmission loss of the CaF₂ substrate.

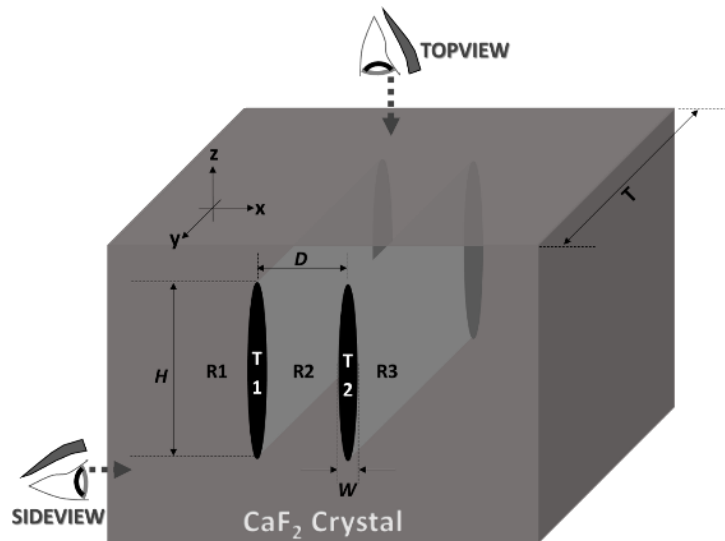
En conclusion de ce chapitre, les propriétés des guides d'onde des structures fabriquées ont été étudiées à la longueur d'onde de 633 nm en couplant la lumière polarisée linéairement d'une source laser HeNe dans ces guides avec un objectif, $NA = 0,15$. Les profils de mode guidé en champ proche sont elliptiques, avec une ellipticité inférieure à 60 %. Les pertes de transmission maximales des guides ont été déterminées à l'aide d'un modèle tenant compte des modes non guidés, ce qui permet d'obtenir une mesure plus précise de la transmission des guides. La perte de transmission des cinq guides d'ondes à doubles pistes de CaF_2 se situe entre 1,9 dB/cm pour le WG-1 et 2,7 dB/cm pour le WG-4, ce qui est proche des mesures de perte de transmission précédemment rapportées dans les cristaux YAG. De plus, une étude de la dépendance de polarisation du guidage des guides a montré que ces guides agissent presque comme des polariseurs parfaits.



Polarization dependent guiding of the five double track waveguides inscribed inside undoped CaF_2 . (a) Normalized transmitted power based on the maximum value of transmitted power as a function of direction of light polarization. (b) Polarization Extinction Ratio (PER) of each waveguide.

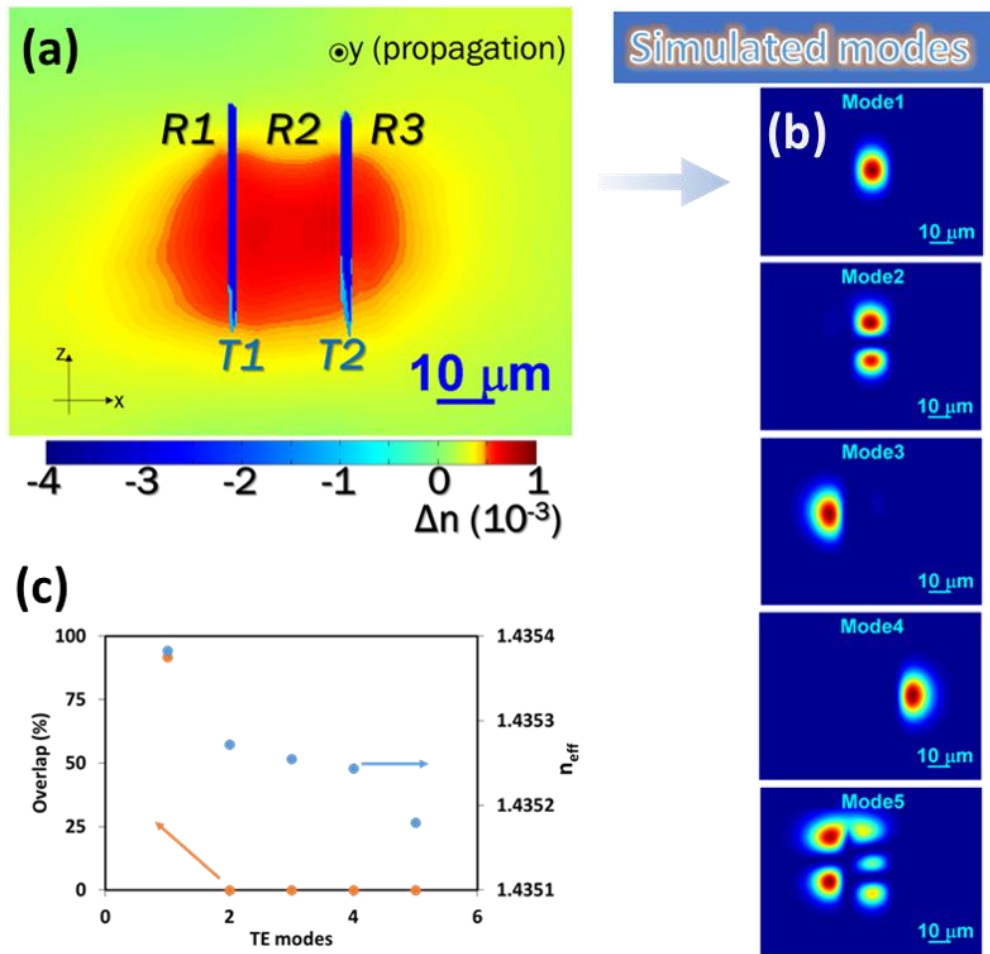
6 MESURE DIRECTE DU CHANGEMENT DE L'INDICE DE RÉFRACTION DES GUIDES D'ONDES CaF_2 À DOUBLE PISTE

Dans le prolongement de la caractérisation des propriétés des guides d'ondes, le chapitre 6 présente les mesures directes de l'indice de réfraction des guides d'ondes mettant en œuvre la technique de microscopie à contraste de phase ainsi qu'une approche par diffraction de Fresnel pour déterminer la carte tridimensionnelle, 3D, de l'indice de réfraction du cristal CaF_2 dans le voisinage des pistes modifiées. La section 6.1 présente brièvement diverses techniques de mesure du changement de l'indice de réfraction et l'avantage comparatif de l'interférométrie par décalage latéral en quadriondes, QWLSI, qui est une nouvelle application de la microscopie par imagerie en phase pour la détection du front d'onde. Les sections 6.2 et 6.3 présentent la théorie et le montage expérimental de l'IQEEQ, respectivement. Les mesures OPD des guides d'ondes à double voie utilisant l'IQEEQ sont présentées à la section 6.4. La section 6.5 présente une discussion détaillée sur l'effet de la diffraction de Fresnel sur les mesures OPD pour la détermination de l'épaisseur des éléments des guides d'ondes contribuant à la mesure de différence de phase. De plus, le profil complet de l'indice de réfraction 3D est présenté. Enfin, la section 6.6 confirme cette nouvelle approche pour la mesure du changement de l'indice de réfraction des guides d'ondes à double piste à l'intérieur des cristaux en comparant les profils de champ de mode de la simulation, obtenu par le solveur en mode propre à différence finie (FDE), et les résultats expérimentaux du chapitre précédent.



3D schematic of the double track waveguide inscribed inside the CaF_2 crystal. T1 and T2 are the modified pairs of track; R2 is the region in between the tracks; R1 and R3 are the sidelobe regions of the tracks T1 and T2, respectively; $W \approx 6 \mu\text{m}$ and $H \approx 40 \mu\text{m}$ are the average width and height of the tracks, respectively; $D = 20 \mu\text{m}$ is the distance between the tracks T1 and T3; and $T = 1.37 \text{ mm}$ is the thickness of the sample.

Jusqu'à présent, plusieurs tentatives ont été faites pour déterminer le changement d'indice de réfraction des guides d'ondes modifiés par laser ultra-court à l'intérieur des cristaux. Cela a été un grand défi. Dans ce chapitre, nous avons présenté une nouvelle approche pour la mesure du changement de l'indice de réfraction et nous avons démontré expérimentalement la précision des résultats.



(a) Spatial map of refractive index change (Δn) measurement of the double track waveguide inside CaF_2 . (b) The first five TE modes of the waveguide determined by simulation. (c) The plot of overlap between the gaussian HeNe source at 633 nm with a waist of 7.5 μm , and the effective refractive index of the five TE modes of the waveguide.

En conclusion de ce chapitre en utilisant une technique de mesure directe de l'indice de réfraction, qui fait appel à la méthode de détermination du nombre de Fresnel, nous pouvons obtenir une carte complète à haute résolution de l'indice de réfraction des microguides qui, autrement, auraient nécessité un polissage coûteux et difficile des échantillons à des dizaines de microns d'épaisseur.

7 CONCLUSION

En conclusion, nous avons présenté une technique de fabrication de dispositifs photoniques à l'aide d'une expérience d'écriture laser femtoseconde. Une fois de plus, cette technique s'est avérée simple et efficace pour la miniaturisation de composants optiques afin d'ouvrir la voie à des solutions photoniques intégrées. La majeure partie des travaux de cette thèse est consacrée à l'inscription femtoseconde de guides d'ondes à double piste à l'intérieur des cristaux de CaF_2 et à leur caractérisation qualitative et quantitative. Une description détaillée des méthodes de caractérisation est également donnée. En plus des inscriptions de guide d'ondes à double piste à l'intérieur de ces cristaux de CaF_2 , des modifications lisses et une écriture non réciproque ont été observées. De plus, la fenêtre de traitement pour ces types de modifications est systématiquement identifiée en ce qui concerne les paramètres d'écriture et les orientations cristallographiques. Au chapitre 5, le modèle simplifié de couplage de la lumière polarisée linéairement dans le guide d'ondes a été utilisé et mis en œuvre pour trouver une limite supérieure des pertes de transmission. Ces estimations ont été calculées entre 1,9 dB/cm et 2,7 dB/cm, ce qui est comparable aux propriétés de propagation des guides d'ondes à double piste dans des cristaux laser similaires. Le chapitre 6 présente une méthode élégante pour la détermination de la modification tridimensionnelle de l'indice de réfraction, Δn , carte spatiale le long et à proximité des guides d'ondes à double voie. Un type spécial de microscopie à contraste de phase, QWLSI, a été utilisé pour obtenir la carte OPD détaillée des guides d'ondes. Ceci a été couplé à une approche analytique pratique pour déterminer l'épaisseur des éléments et a abouti à une carte spatiale tridimensionnelle détaillée Δn avec des valeurs qui sont de l'ordre de 10^{-3} . Ces résultats ont été confirmés par la similitude d'une simulation en mode propre et de modes fondamentaux guidés expérimentalement.

Nomenclature

Symbols

n	Refractive index
n_0	Linear refractive index
n_2	Nonlinear refractive index
λ	Wavelength of the source
P_{cr}	Critical threshold power
m_e	Effective electron mass
e	Fundamental electron charge
γ	Keldysh parameter
c	Speed of light in vacuum
I	Laser intensity
β	Avalanche ionization coefficient
σ_m	Absorption cross-section related to multiphoton process
E_g	Bandgap energy/ ionization potential of the dielectric material
N_c	Critical density of electrons in the plasma
ω	Angular frequency of the laser source
ω_p	Plasma angular frequency
D_{th}	Thermal diffusion coefficient
κ	Thermal conductivity
ρ_0	Density of the medium
C_p	Specific heat capacity at constant pressure
τ_D	Heat diffusion time
ω_0	Diffraction limited beam waist
E_{th}	Threshold energy
I_{th}	Intensity for the modification threshold
NA	Numerical aperture
τ	Pulse duration
f	Repetition rate of the laser source
Δn	Refractive index change
σ_{ij}	Stress tensor
S	Elastic compliance
\mathcal{E}_i	Strain tensor
c_{ij}	Elastic constant
λ_l	Wavelength at laser emission
v	Speed of writing

F	Fluences
Z_R	Rayleigh length
N_f	Fresnel number
n_{eff}	Effective refractive index

Acronyms

CPA	Chirped pulse amplification
UV	Ultraviolet
IR	Infrared radiation
3D	Three dimensional
Nd:YAG	Neodymium-doped Yttrium Aluminium Garnet
CaF ₂	Calcium Fluoride
MPA	Multiphoton absorption
SEFI	Strong electric field ionization
CW	Continuous wave
RF	Radio frequency
AOM	Acousto-optic modulator
GUI	Graphic user interface
CCD	Charged coupled device
MFD	Mode field diameter
PDD	Power density distribution
ISO	International organization for standardization
DLW	Direct laser writing
PER	Polarization extinction ratio
TE	Transverse electric
TM	Transverse magnetic
dB	Decibels
QWLSI	Quadriwave lateral shearing interferometer
MHM	Modified Hartmann Mask
OPD	Optical path difference
MTF	Modulation transfer function
DoF	Depth of field

List of Figures

<i>Figure 2-1 : Timestamp of the physical phenomena during ultrafast laser interaction with transparent dielectric materials [9].</i>	7
<i>Figure 2-2 : Schematic representation of Filamentation processes by the intense core of the beam. The solid lines show the diameter of the intense core while the dashed line indicates the root mean square radius of the full beam for linear propagation. The arrowed line in the middle shows the direction of illumination. Modified from [23].</i>	10
<i>Figure 2-3 : Periodic trends for ionization energy (IE) vs. atomic number {copied from https://en.wikipedia.org/wiki/Ionization_energy}</i>	12
<i>Figure 2-4 : Schematic diagram of the photoionization of an electron in an atomic Coulomb potential for different values of the Keldysh parameter. The grey broken line indicates the potential barrier. (Inspired by [22], [25]).</i>	14
<i>Figure 2-5 : The photoionization rate and the Keldysh parameter as a function of laser intensity for 800 nm light in fused silica (7.5 eV band-gap). The black dotted line describes tunneling only (equation (40) in [28]); the dotted red line shows multiphoton ionization only (equation (41) in [28]); and the solid blue line is for the full expression from Keldysh (equation (37) in [28]){modified from [22] and [27]}.</i>	15
<i>Figure 2-6 : Nonlinear ionization process dominating ultrafast laser writing. (a) and (b) show direct photoionization processes with multiphoton and tunneling ionization processes, respectively. (c) shows the avalanche ionization process [8].</i>	17
<i>Figure 2-7 : Schematic diagram of two modification regimes in DLW. Athermal and thermal regimes of writing with low and high repetition rate of the pulses, respectively (inspired by [10], [26]).</i>	22
<i>Figure 2-8 : Transmission microscope bright-field (BF) images of the damage tracks produced in a Nd:YAG sample by 120-fs pulses at a writing speed of 200 $\mu\text{m/s}$. The beam was focused from the top. (modified from [16]).</i>	24
<i>Figure 2-9 : Refractive index distribution of waveguides written inside LiNbO₃ with type I and type II modification regimes in (a) and (c). The respective beam profiles that are guided along the modified zones are shown in (b) and (d), respectively. The broken line in (b) shows the modified track in (a) and the red ellipses in (d) depict the double damage tracks shown in (c). (modified from [49])</i>	25
<i>Figure 2-10 : Simplified depiction of a crystal.</i>	28

Figure 2-11 : Portion of a lattice. a , b and c are lengths of the cell edges and α , β and γ are cell angles between them.-----	28
Figure 2-12 : Representation of Bravais Lattices of cubic crystal system. (i) The simple/primitive cubic (sc), (ii) the body centered cubic (bcc) (iii) the face centered cubic (fcc) lattices. -----	29
Figure 2-13 : (a) General three-dimensional representation of second rank tensor, e.g. stress. (b) Two-dimensional representation of strain with a square that is deformed to a parallelepiped. -----	30
Figure 2-14 : (a) Tensor representation of the form of the elastic compliance tensor for cubic crystallographic systems. Standalone dots represent zeros; dot and a line represent equal components; X represents 2 fold (S_{11} - S_{12}) approximately while the interconnecting line indicates that they are equal (inspired by [79]) . (b) and (c) show elasticity, 10^{-12}Pa^{-1} , of CaF_2 and YAG respectively (data from [80]). -----	31
Figure 2-15 : Unit cell of CaF_2 . The black balls represent the Ca atoms, and the green balls represent the F atoms [83]. -----	33
Figure 3-1 : The summary sketch of the 3D direct laser writing setup. $\lambda/2$ – half-wave plate; f_1 – 1000 mm convex lens; f_2 – 500 mm convex lens; AOM – Acousto Optic Modulator; DM – dichroic mirror; LPF – long pass filter; MO – microscope objective; M – mirror. The AOM and 3-axis stage are synchronized and computer controlled. An LED white light source and a CCD camera enable in-situ imaging of the sample during fabrication. -----	39
Figure 3-2 : Relationship between AOM RF Voltage and the fraction of peak power delivered. -----	42
Figure 4-1 : Optical micrograph of femtosecond inscription of matrix of number of pulses/speed of writing ($\mu\text{m/s}$) and RF voltage (v)/energy of writing(μJ) for undoped CaF_2 sample. (a) shows coarse modifications; (b) shows fine tuning around the threshold of modification. The red rectangle shows crack formation while the green rectangle shows the threshold of modification. -----	45
Figure 4-2 : Sketch of two undoped CaF_2 samples used for waveguide track fabrication. (a) shows the sample Group A with polished faces parallel to $[112]$, $[110]$ and $[111]$. Similarly, (b) shows the sample Group B with polished faces parallel to $[043]$, $[134]$ and $[611]$. -----	47
Figure 4-3 : Schematic diagram of a conical shaped beam focused at $150\ \mu\text{m}$ mechanical depth below the sample. LEFT: Beam focused inside the sample; RIGHT: beam focused at the edge of the sample. d is the beam diameter at the surface of the sample. -----	50
Figure 4-4 : Microscope images of all the five tracks written inside undoped CaF_2 crystal. (a) and (b) are side (xz) and top (xy) bright field (BF) images in transmission of written tracks with different energies, respectively. (R) - reference single track written to locate the double tracks. (c) shows dark field (DF) image in reflection of a dual track waveguide written with $0.44\ \mu\text{J}$. (d) shows the 20X BF image of a transversally sliced part of the sample with thickness, t , of $1.37\ \text{mm}$. -----	51

Figure 4-5 : Example of the inscribed tracks with a number of pulses of 2280 per spot and a fluence of 12 J/cm ² . The polarization is along the y- and x-axis of Sample A in (Case 1, 3) and (Case 2,4), respectively. Furthermore, a and b indicate the scanning directions.-----	52
Figure 4-6 : The fraction of smooth modification for the track inscribed with $N \approx 2000$, and $F = 12 \text{ J/cm}^2$.-----	53
Figure 4-7 : All smoothly modified tracks with non-zero fractions as a function of number of pulses and fluence. (a) and (b) show the two directions of scanning in each axis. -----	53
Figure 4-8 : Plot of all the smooth modifications inside CaF ₂ and the contour, at 30% of the smooth modification ratio, shows windows for the writing parameters with respect to the direction of scanning, crystallographic axes, number of pulses per spot and fluence. The gray scale indicates the percentage of the track that is smoothly modified.-----	54
Figure 4-9 : Bright field microscopic image of double tracks. (a) shows section of a smoothly modified track inscribed with case 2 at 240 $\mu\text{m/s}$ ($N \approx 2400$) and energy of 0.47 μJ ($F = 11.4 \text{ J/cm}^2$); (b) shows part of modified track inscribed with case 2 at 10 $\mu\text{m/s}$ ($N \approx 57000$) and energy of 0.67 μJ ($F = 16.4 \text{ J/cm}^2$) with no smooth modification.-----	56
Figure 4-10 : Double track written at speed of 240 $\mu\text{m/s}$ ($N \approx 2400$) and energy of 0.47 μJ ($F = 11.4 \text{ J/cm}^2$) with case 2. (a) shows the two-dimensional refractive index change map of the portion of the double track as viewed from the top; (b) shows the line profile of the refractive index change map. -----	57
Figure 4-11 : Illustration of the differential heating of a crystal as a result of the bulk photothermal effect (copied from [123]).-----	59
Figure 4-12 : Non-reciprocity of writing based on the pixel counts of the written tracks. In the color scale, 0 and 1 show no or smooth modification and the maximum modification in each case, respectively.-----	60
Figure 4-13 : Near field profile images of light guided inside double track waveguides inside CaF ₂ crystal with writing directions shown above the sketch of the tracks with circle and x and circle and dot for the inward and outward directions of writing, respectively. (a) HeNe source at 633 nm; (b) and (c) are tracks written by opposite directions of writing with polarizations parallel and perpendicular to the elongation of the tracks, respectively; (d) and (e) are tracks written by same directions of writing with polarizations parallel and perpendicular to the elongation of the tracks, respectively. -----	61
Figure 5-1 : Schematic plots of the fabrication of the three categories of guiding inside crystal materials by femtosecond laser irradiation and the spatial locations of the waveguide modes: a) waveguides based on Type I modification in single-line geometry, b) waveguides based on Type II modification in dual-line geometry, and c) waveguides based on Type II modification in depressed cladding Type III geometry. [132] -----	66
Figure 5-2 : (a) OPD measurement of double track waveguide, (b) OPD measurement of single track, (c) simple arithmetic addition of two single track OPD measurements and (d) line profiles of the OPD spatial maps of	

double track (Solid black line), single track (broken green line and a point) and generated double track (broken violet line).----- 67

Figure 5-3 : Refraction and reflection of light at a dielectric interface. The proportion between reflected and refracted beam power can be calculated using Fresnel equations. ----- 69

Figure 5-4 : Waveguiding setup. The source @ 633 nm is a HeNe Laser; $\lambda/2_1$ and $\lambda/2_2$ are half-wave plates; BB1 and BB2 are beam blockers/screens; PBS is a polarization beam splitter; M is a mirror at 45°; OBJ 1 is an Olympus Neo SPlan 5x injecting/focusing objective with NA = 0.13; S is the sample; SH is the sample holder with x-y-z 3D linear translations in addition to rotary translations with polar angle ϑ and azimuthal angle ϕ ; OBJ 2 is an Olympus UPlanFLN 20x imaging with NA = 0.5; P is a pinhole; BP is a Thorlabs BC106N-VIS Charge-Coupled Device (CCD) Beam Profiler.----- 71

Figure 5-5 : Intensity images/ profiles of a micro-scale ruler on the CCD camera position. (a) shows the HeNe laser at 633 nm as a source while (b) shows illumination with white light. I_{min} and I_{max} are the normalized intensity values at the maximum and minimum radiation intensity; the dark marks are the marks of the micro-scale ruler with 10 μm between them.----- 72

Figure 5-6 : Normalized intensity of measured and smoothed data points for determination of pixel distances between the scales of the micro ruler. (a) blue markers show measured data intensity vertically binned, continuous red lines represent the smoothed data and green discrete line at 35 % of maximum; (b) smoothed data trimmed at 35 % to avoid errors due to background and smoothing.----- 73

Figure 5-7 : PDDs of the injected HeNe laser source and the guided modes of five waveguides. Light blue broken lines show the boundary at $1/e^2$ of the maximum amplitude. ----- 74

Figure 5-8 : Near Field, NF, MFD of modeled power density distributions. (a) Evolved unguided circular Gaussian mode in 2D, (b) Guided elliptical Gaussian mode in 2D, (c) Modeled unguided mode at the exit facet of the sample in 2D and (d) the 3D view of the modeled unguided mode. ----- 78

Figure 5-9 : Transmission loss setup. (a) P_{out1} is the power output measured as the sum of all the unguided mode and guided mode collected by focusing optics. (b) P_{out2} is the power output measured as the sum of a portion of the unguided mode and all of the guided. ----- 79

Figure 5-10 : (a) The profile of WG-1 with the pinhole edges encircling the guided mode. (b) Binary image of edges and (c) The numerically fitted circle, $2r_{pin} = 64.8 \mu\text{m}$, to completely encapsulate the edges. ----- 80

Figure 5-11 : Transmission loss (dB/cm) of the CaF_2 undoped crystal double-track waveguides in comparison with some previously reported transmission losses where red is a $\text{Nd}:\text{CaF}_2$ crystal [75]; black is a $\text{Yb}:\text{YAG}$ ceramics [101]; green is a $\text{Cr}:\text{YAG}$ crystal [109] and blue is a $\text{Yb}:\text{YAG}$ crystal [106]. The gray line at 0.31 dB/cm is the transmission loss of the CaF_2 substrate.----- 83

Figure 5-12 : Polarization dependent guiding of the five double track waveguides inscribed inside undoped CaF_2 . (a) Normalized transmitted power based on the maximum value of transmitted power as a function of direction of light polarization. (b) Polarization Extinction Ratio (PER) of each waveguide. -----	84
Figure 6-1 : Schematic layout of QWLSI setup for determination of OPD. MHM - Modified Hartmann Mask [150].-----	88
Figure 6-2: (a) 1D interferogram formation by a MHM in the case of a disturbed input wavefront; geometrical approach. (b) Interferogram obtained with an aberrant wavefront. (c) Zoom on a part of (b), visualization of the local frequency modulations. (d) Fourier Transform of (b). (e) Obtaining of 2 OPD orthogonal gradients by Inverse Fourier Transform of 2 sub-images of (b). (f) 2D Integration of the gradients to reconstruct the OPD and intensity (I) images. The figure is copied and modified from [150].-----	89
Figure 6-3 : 3D schematic of the double track waveguide inscribed inside the CaF_2 crystal. T1 and T2 are the modified pairs of track; R2 is the region in between the tracks; R1 and R3 are the sidelobe regions of the tracks T1 and T2, respectively; $W \approx 6 \mu\text{m}$ and $H \approx 40 \mu\text{m}$ are the average width and height of the tracks, respectively; $D = 20 \mu\text{m}$ is the distance between the tracks T1 and T3; and $T = 1.37 \text{ mm}$ is the thickness of the sample.-----	91
Figure 6-4 : OPD measurements along the double tracks of the waveguides. (a) and (b) show the OPD measurement in the lateral (xy-plane), while (c) and (d) show the longitudinal (xz-plane) measurements. (a) and (c) are measurements with the polarization parallel to the track while (b) and (d) show OPD measurements for the polarization perpendicular to the tracks. -----	92
Figure 6-5 : Line profile of the OPD measurements. (a) xy-plane. (b) xz-plane. The solid line shows WG-1; the broken line with one dot shows WG-2; the broken line shows WG-3; the broken line with two dots shows WG-4; and the dotted line shows WG-5. Black color indicates measurements with the polarization parallel to the track, while green color indicates measurements perpendicular to the tracks.-----	93
Figure 6-6 : Near-Field and far field diffraction of a plane wavefront at an aperture slit of diameter $2a$. -----	95
Figure 6-7 : (a) Sketch of waveguides with the OPD contributions with discrete elements for different Fresnel zones. (b) The plot of evolution of the OPD contributions from different layers of discrete Fresnel zones with radii $b > a$. -----	96
Figure 6-8 : $0.5 \mu\text{m}$ long stairs written with $0.15 \mu\text{J}$ at 10 MHz with different distance between them (d_s) and different step in depth (Z). -----	97
Figure 6-9 : OPD (nm) measurement of stairs with an d_s of $2 \mu\text{m}$ and mechanical depth step of $0.1 \mu\text{m}$. -----	98
Figure 6-10 : (a) Raw measurement of OPD (nm) of the stairs of Exp # 5 ($d_s = 3 \mu\text{m}$ and step of depth = $0.5 \mu\text{m}$) with $0.15 \text{ NA}_{\text{condenser}}$, (b) Normalized, inverted and selected stairs after transformation.-----	100
Figure 6-11 : 2D- and 3D-images of post processing of the selected stairs (Exp#5). (a) Selected and normalized stairs. (b) Fitted stairs to find the smallest element and (c) masked stairs based on the smallest element. (d), (e) and (f) show the respective 3D-images. -----	101

Figure 6-12 : Equivalent OPD contribution of the stairs in Exp # 5 with blue dots – equivalent OPD calculated as the height of the elliptical cylinder for the same volume of the masked stair; solid blue line – fitted parabolic curve to find the Z intercept, and the red broken line indicates the z intercept at $-0.29 \mu\text{m}$. -----	102
Figure 6-13 : The OPD contribution of stairs of different experiments with different step and distance between stairs superimposed together. -----	103
Figure 6-14 : Generating a binary mask of double tracks of WG-1. (a) Intensity image of WG-1; (b) Binary mask of double tracks after post processing. The scale bar represents the normalized intensity based on the maximum intensity values. -----	105
Figure 6-15 : Spatial map of refractive index change (Δn) measurement of WG-3. (a) Spatial map of Δn along the tracks. (b) Spatial map of Δn in the vicinity of the tracks. (c) Spatial map of Δn by blending (a) in to (b). (d) Line profile Δn at the middle of the tracks along the x-axis. -----	106
Figure 6-16 : The three-dimensional spatial Δn of all the five waveguides.-----	107
Figure 6-17 : (a) Line profile of Δn for all the waveguides as it is shown in Figure 6-16 above. (b) The minimum and maximum Δn values of the waveguides. -----	107
Figure 6-18 : Importing the 3D spatial map of waveguides for simulation using Mode Solutions of Lumerical Inc. (a) screenshot of the (n,k) material import wizard; (b) File format for isotropic material and on the left example for WG-1; and (c) Index monitor to view the imported material (in this case for WG-1).-----	109
Figure 6-19 : (a) - (e) show the first five TE modes of WG-1 determined by simulation. (f) shows the plot of overlap between the assumed HeNe source at 633 nm with a radius of $7.5 \mu\text{m}$, and the effective refractive index of the five TE modes of WG-1. -----	110
Figure 6-20 : Fundamental power density distribution (PDD) of both simulated (a) and experimental (b) profiles of all the five waveguides. -----	111
Figure 6-21 : Mode-Field diameters of both simulated (squared marks) and measured (circular marks) PDDs.-----	111
Figure 7-1: (a) Image of the cross section and (b) radial refractive index profile of a depressed cladding waveguide inscribed in sapphire. The profile is computed along the solid blue line, and data are plotted symmetrically on both sides of the central axis. (copied from [155])-----	115

List of Tables

<i>Table 2-1 : The seven crystal systems and the restrictions on their cell dimensions. -----</i>	<i>29</i>
<i>Table 2-2 : Comparison of properties of Yb-doped YAG and CaF₂ (copied and modified from [13])-----</i>	<i>34</i>
<i>Table 4-1 : DLW waveguide inscription parameters of CaF₂ waveguides. Crack th. – threshold of crack formation; Mod. th. – Modification Threshold; E_p (μJ) – Energy per pulse; E_D (mJ) – Total Energy Delivered at focal point; F (J/cm²) – fluence; E_v (J/cm³) – Total Energy Deposition per unit volume and I (TW/cm²) – Irradiance. -----</i>	<i>49</i>
<i>Table 5-1 : Near-Field MFD of double-track waveguides inside CaF₂ and the HeNe source. -----</i>	<i>75</i>
<i>Table 5-2 : Transmission loss experiment measured values for three independent experiments. Where DLW E is the writing energy for each waveguide in μJ. -----</i>	<i>82</i>
<i>Table 6-1: Different parameters of the stairs selected for post processing. Exp # - Experiment parameter number; d_s – distance between the stairs; Estimated z (μm) – mechanical depth multiplied by the refractive index of CaF₂ at the wavelength of 1030 nm; Measured z (μm) - measured depth under the microscope; P (W) is the writing power measured just after the AOM in the writing setup; Total # stairs is the number of stairs inscribed for each given parameter. -----</i>	<i>99</i>
<i>Table 6-2 : Calculated Depth of Field for the xz-plane of refractive index measurements. -----</i>	<i>104</i>
<i>Table 6-3 : Simulated results of the effective refractive index (n_{eff}) of all the five waveguides for fundamental modes. The third row shows the effective numerical aperture (NA_{eff}) that should be considered. The last row shows the overlap between the source and the fundamental modes. -----</i>	<i>112</i>

1 Introduction

1.1 Motivation and Aim

Light is a form of radiant energy or energy that travels in waves. Throughout the ages, from the Greek philosophers Socrates, Plato, Euclid to the times of Ibn al-Haytham, who disproved the emission theory of vision from ancient Greek to the recent times of Newton, Huygens, Maxwell and Einstein, many researchers have taken up the challenge to define the nature of Light.

Progress of the study of light over 2000 years leads to the accumulated knowledge which consequently leads to the discovery of the true nature of light, namely photons which are defined as the quanta of light. The photons have many mysterious properties, for example, dual properties of a wave and a particle depending on the type of experiments and interactions with matter. This leads to categorizing light based on its different properties like polarization, wavelength, power, and so on. In accordance with the various properties of light, materials can be made to respond differently for these traits. The property of materials exhibited to light exposure to attain different features distinctly from the non-excited or non-exposed materials, that is relevant to many phenomena and applications, is called photosensitivity. Photosensitivity is essential for applications ranging from photosynthesis and lithography to ultrafast laser writing.

The discovery of lasers, that emit light coherently, gives rise to more effective and diverse applications of light. High power laser applications like laser cutting, drilling, welding and also lithography were possible with lasers thanks to the spatial coherent property which enabled a laser to be focused to a tight spot. Similarly, the temporal coherence property of lasers can be used to generate very short femtosecond pulses as well as single-frequency sources.

The advent of powerful lasers that can produce coherent pulses in the femtosecond regime when mode-locked have opened new frontiers in material research with extremely short temporal and high spatial resolutions. In fact, the breakthrough of the amplification technique called “CPA” (chirped pulse amplification) has been awarded the Nobel prize in 2018. Concurrently, laser-induced damages in transparent materials have been subject of numerous studies over more than the past two decades. Since the 1970s, experimental and theoretical investigations related to damages in silica glasses by the effect of UV radiation, that are equivalent in energy per photon with interband transitions from the valence to the conduction band, have been underway [1]. However, in 1996, following the pioneer work of Hirao’s group on the laser damage inside transparent dielectric materials, there was a breakthrough in femtosecond laser dielectric material processing, materials that do not have any linear absorption at the wavelength of the femtosecond laser, by visible and IR lasers with high-energy-density femtosecond sources [2]. Following this paradigm shift, there have been rapid developments and applications of both surface and volume processing of dielectric materials using ultrafast lasers thanks to the fast growth in wide implementation and advancement of ultrafast lasers for both fundamental research and practical applications during the same period [3]. As a result, dramatic progresses and intensive studies with more modified systematic approaches and techniques of ultrafast laser writing have shifted ultrafast laser writing from scientific curiosity to standard fabrication techniques. For example, recently ultrafast laser written waveguides are becoming comparable with quality to those produced with other more conventional techniques while being less expensive [4].

The generalized model of bulk damage in homogenous dielectric materials by ultrafast lasers involves a combination of nonlinear absorption processes resulting in the excitation and heating of electrons followed by transfer of this heat energy to the surrounding lattice. The deposition

of this energy induces, by a variety of mechanisms, refractive index modifications localized over a micrometer-sized volume of the material. By combining these localized modifications with the 3D movement of the focal volume of the ultrafast laser beam, it is possible to inscribe optical waveguides or more complex photonic circuits.

In comparison with other material modification techniques, e.g. photolithography, there are unique advantages in favor of ultrafast laser micromachining of bulk transparent materials [5] to mention but a few:

- **Damages are extremely confined:** The nonlinear nature of the absorption confines any induced changes to the focal volume in combination with laser-beam scanning or sample translation making it a simpler and less expensive device production technique for compact photonic systems [6].
- **Enables rapid prototyping:** The setup usually gives access to simple software control of the writing patterns and parameters. This results in a significant cost reduction of production with respect to standard techniques.
- **Intrinsically a three-dimensional (3D) technique:** Since the nonlinear absorption process is more or less independent of the type of material and localized to the focal volume, the refractive index changes can be induced at any point inside the bulk material, 10 μm to 10 mm from the surface. This capability can be manipulated to implement fabrication of novel devices, for example an ‘optical motherboard’ [7]–[9].

Consequently, these advantages resulted in a rapid progress of ultrafast laser micromachining which gives rise to realization of vast ranges of photonic devices. This is a driving force behind industrial interest for rapid prototyping of optical components [10]. Among its vast implementations, there have been a growing number of applications for high repetition rate laser systems which can be achieved through functionalization of laser systems and subsystems by miniaturizing photonic components. Highly efficient crystalline waveguide lasers have been demonstrated and can be realized with waveguides inside optically active media [11]. For

instance, waveguides, that can be inscribed using ultrafast laser micromachining techniques, offer a confinement and an excellent overlap between pump and laser modes over the entire length of the medium. Thus, given the very small pump and laser mode diameters, a large gain can be achieved, resulting in laser systems with small laser thresholds. Moreover, resonator mirrors can be achieved by coating end facets of the waveguides, inscribing Bragg structures or with optical contact. The integration of saturable absorbers to the combination of a waveguide and integrated mirrors can result in cost effective, highly efficient, stable and robust high repetition rate mode-locked lasers. In general, this is the motivation behind this thesis work.

The entirety of this thesis project is dedicated to crystalline materials due to the superiority in thermomechanical properties and higher emission/absorption cross sections of rare earth doped crystalline materials as compared to glasses. The method to identify parameters of ultrafast laser inscription of waveguides inside crystalline materials has been presented. In parallel, the thesis aspired to refine the approaches for qualitative and quantitative characterizations of the waveguiding properties of modified transparent materials, namely transmission loss of the guided modes and a very accurate determination of the three-dimensional refractive index change of the modified material.

This thesis commenced with the study of double track waveguides inside Neodymium-doped Yttrium Aluminium Garnet (Nd:YAG). As it is a common crystal widely used as gain medium in solid state lasers, several studies had already been done and presented on Nd:YAG [12]. Thus, a study of double track waveguides was performed with the intention to confirm and attest our experimental and theoretical approaches. Furthermore, due to its scalability during crystal growth and competitive spectroscopic, mechanical and thermo-optical advantages specially for diode- pumped large-scale high-energy lasers, CaF_2 , as “new old laser material”, is blooming to become a better candidate as a host material [13]. We chose to study both YAG and CaF_2 , the large part of the project was dedicated to CaF_2 . Taking into account that both crystals are cubic, owing to their crystallographic structures, optical specificities and restrictions of low-symmetry crystal optics are neglected which enables a more simplified

systematic approach to study modifications due to ultrafast laser micromachining along the micro-modified zones of the crystals.

In Chapter 2, a brief theory on laser matter interaction during ultrafast laser micromachining, and the properties of crystals of interest is presented followed by the experimental procedures to inscribe waveguides in Chapter 3. In Chapter 4, anomalies during ultrafast laser micromachining which resulted in non-reciprocal, ‘quill’, writing and smooth modification is discussed together with double track waveguide inscription at different pulse energies inside CaF_2 crystals. While Chapter 5 is dedicated to briefly summarize a refined quantitative and qualitative modeling of the approach and result for transmission loss measurements of the guided modes inside double track waveguide in CaF_2 crystals. Followed by Chapter 6, which is also dedicated to characterizing the waveguides using the Fresnel number approach to generate the 3D map of refractive index change measurements implementing the phase-contrast microscopy method. Chapter 7 concludes the main tasks accomplished during the thesis. Finally, the work on Nd:YAG by our group is briefly presented in the Appendix A.

2 Laser-Matter Interaction in Crystals

Despite the promise of femtosecond laser pulses in processing wide bandgap dielectric materials for a variety of applications, understanding the fundamental aspects of intense femtosecond laser interactions with dielectrics has been a challenging task. It is the objective of this chapter to provide the theoretical overview of recent efforts at uncovering the subtleties of femtosecond laser interactions with wide bandgap dielectrics, crystals in particular. In the upcoming Section 2.1, the ultrafast time-resolved studies of the dynamics of electronic excitation and pulse propagation that are related to material modification are discussed. Moreover, types of modifications in crystals and the fundamental aspect of crystals together with the crystals of interest and the state-of-the-art are discussed in Sections 2.2, 2.3, 2.4 and 2.5, respectively.

2.1 Fundamental Principles of Laser-matter Interaction

Due to historical reasons, and in relation to semiconductor light sources used for telecommunications, most lasers, for example Yb/Nd:YAG lasers, many fiber lasers and the most powerful laser diodes, emit near-infrared light. Comparatively, there are fewer laser sources for the mid- and far-infrared spectral regions and also in the UV regime. However, most dielectric materials used for photonics systems and subsystems are transparent to near-IR lasers. Consequently, for the ease of its accessibility, the study of the processes of material response following exposure to intense near-IR femtosecond laser irradiation are far more complex, particularly for wide bandgap dielectrics, which are transparent for photons at this wavelength. However, when a dielectric material is subjected to focused femtosecond laser irradiation with a sufficiently high pulse peak intensity, the absorption of the material becomes intensity dependent, and a large amount of excited electrons are generated as free carriers. This

phenomenon followed by relaxation channels of electronic excitation in wide bandgap materials in relation to heat deposition to the surrounding lattice produces photo induced defects in the otherwise “defect-free” medium [14].

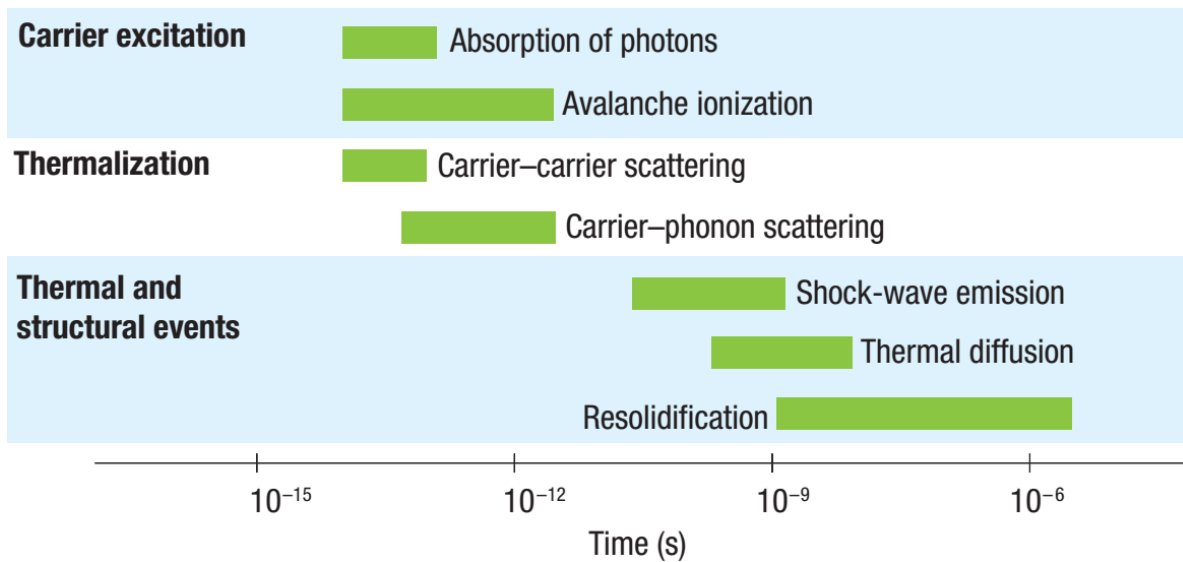


Figure 2-1 : Timestamp of the physical phenomena during ultrafast laser interaction with transparent dielectric materials [9].

The underlying physical phenomena that describe an intense ultrafast laser beam writing inside a dielectric material is accepted as a three-stage process resolved temporally as electronic (carrier) excitation followed by thermalization and localized structural modifications as shown in Figure 2-1. Understanding the timescale of different physical phenomena provides a detailed insight into why femtosecond laser pulses are useful for micromachining applications of dielectric materials. In addition, the nonlinear excitation gives femtosecond laser-induced damage confinement and repeatability. Firstly, the intense laser beam focused into the material, gets absorbed and generates electrons. These electrons then form a plasma and consequently transfer their kinetic energy to the lattice over a picosecond timescale. Within a couple of nanoseconds, a pressure or a shock wave due to subsequent relaxation of stress [9] separates from the focal volume followed by a large density distribution change coupled with accompanying the heat diffusion out of the focal volume at a nanosecond and microsecond scale. For sufficiently high pulse energy, these thermodynamic processes result in material melting and microexplosions, leaving behind permanent structural changes [9], [15].

2.1.1 Nonlinear Propagation and Filamentation

For large pulse powers, provided that the ultrafast laser beam will also undergo nonlinear propagation inside the dielectric material which modifies the spatial intensity distribution that can rather be described with linear terms, the process of laser-matter interaction at high intensities is much more complex [16]. The main nonlinear mechanisms affecting the propagations are:

1. **Nonlinear Polarization for self-focusing (Optical Kerr effect):** When light propagates inside a transparent dielectric material, it induces oscillating electric dipoles at a microscopic level that give rise to a cumulative macroscopic polarization. The polarization vector could be expanded as a Taylor series whose coefficients are the nonlinear susceptibilities. Thus in dielectric materials which have an inversion center ($\chi^{(2)} \approx 0$), the polarization vector, \mathbf{P} , can be approximated as [17]:

$$\mathbf{P} \approx \epsilon_0 \left[\chi^{(1)} + \frac{3}{4} \chi^{(3)} |\mathbf{E}|^2 \right] \mathbf{E} \quad (2.1)$$

Where \mathbf{E} is the electric field vector; $\mathbf{P}^L = \epsilon_0 \chi^{(1)} \mathbf{E}$ is the linear part of the polarization; while $\mathbf{P}^{NL} = \epsilon_0 \chi^{(3)} |\mathbf{E}|^2 \mathbf{E}$ represents the nonlinear part of the polarization. Thus, the total distribution of refractive index can be given as [8]:

$$n = \sqrt{1 + \chi^{(1)} + \chi^{(3)} |\mathbf{E}|^2} \approx n_0 + n_2 I \quad (2.2)$$

Where $n_0 = \sqrt{1 + \chi^{(1)}}$ is the linear refractive index, $n_2 = 3\chi^{(3)}/\epsilon_0 c n_0^2$ is the nonlinear refractive index and $I = \epsilon_0 n_0 c |\mathbf{E}|^2 / 2$ is the laser intensity. According to the expression above, the spatially varying refractive index relative to the intensity of the beam acts as a positive lens, for positive n_2 in most dielectric materials, and further focusing the beam on itself. However, it should be noted that the nonlinear refractive

index is exclusively related to the local intensity or simple peak power of the beam. Thus, as the peak power of the laser beam increases, self-focusing of the beam plays a role to overcome the beam diffraction and it might lead to collapse if the input peak power exceeds a critical threshold, P_{cr} , defined as [18]:

$$P_{cr} = \frac{3.72\lambda^2}{8\pi n n_2} \quad (2.3)$$

Where λ is the wavelength of the source; n and n_2 are the linear and nonlinear refractive indices, respectively. The origin of such a critical power is the dependence of the refractive index of the material on its polarizability in which this critical point is also the indication of saturation of the effective polarizability, i.e. the point where all molecules are aligned with their “easy” axes of polarizability [18]. For example, this critical point is calculated for both CaF_2 and YAG as 5.3 MW and 0.8 MW, respectively.

2. **Plasma defocusing:** In reality, the self-focusing of the beam is usually sufficient enough for an abrupt onset of multiphoton absorption instantaneously followed by electron plasma formation. The free electrons inside the plasma will then contribute to a negative refractive index gradient which can be approximately expressed as [19]:

$$n_p = n - \frac{N(r, t)}{2N_c} \quad (2.4)$$

Where n_p is plasma refractive index; n is the refractive index of the bulk material; $N(r, t)$ is the density of free electrons, . The critical density of carriers, N_c , can be given as [20]:

$$N_c = \frac{(4\pi^2 \epsilon_0 m_e c^2)}{(e^2 \lambda^2)} = 1.11 \times 10^{21} / (\lambda / \mu\text{m})^2 \text{ cm}^{-3} \quad (2.5)$$

Where ϵ_0 is the permittivity of free space; m_e is the mass of electron; e is the charge of the electron; c is speed of light; and λ is the wavelength of the laser source. For example, for the laser at 1 μm wavelength, this point is achieved for the carrier density of 10^{21} cm^{-3} . Thus, this defocusing effect of the plasma counter acts the positive refractive index change produced by the Kerr effect, resulting in a defocusing of the beam. The interplay between these two nonlinear effects will lead to the propagation of the beam at a very small size over several Rayleigh distances and the process is called Filamentation [8], [21], [22].

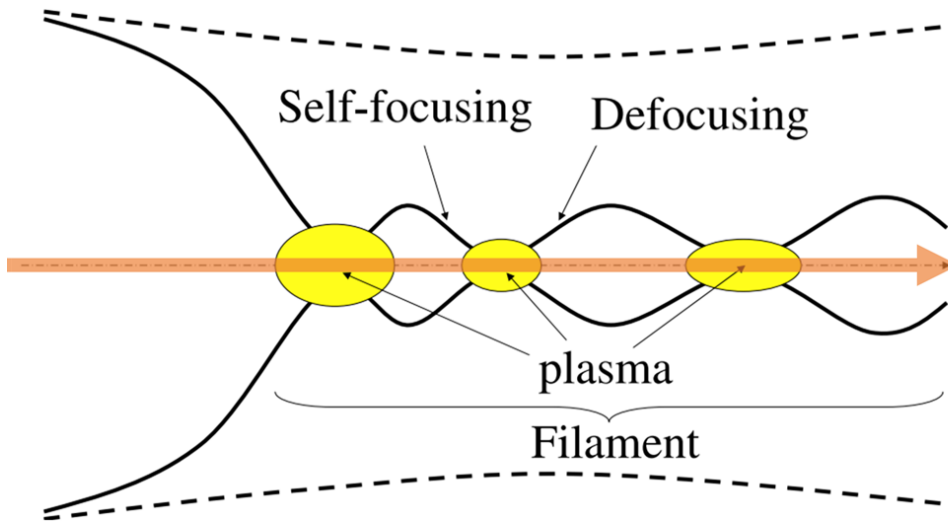


Figure 2-2 : Schematic representation of Filamentation processes by the intense core of the beam. The solid lines show the diameter of the intense core while the dashed line indicates the root mean square radius of the full beam for linear propagation. The arrowed line in the middle shows the direction of illumination. Modified from [23].

As it is depicted in Figure 2-2, the combination of the optical Kerr effect, multiphoton absorption, MPA, and ionization result in the origin of the formation of the first cycle of the filaments preserving an average small diameter over a long distance. This beam at this cycle is further attenuated by mainly losses due to plasma absorption and multiphoton ionization. As the pulse further propagates, it is nonlinearly refocused and becomes sufficiently intense with a peak power above P_{cr} which should undergo a collapse. However, MPA attenuates the core of the beam and a plasma is generated once more near the collapse location, which defocuses the beam core once again and gets attenuated because of nonlinear losses as described above.

The repetition of this scenario sustains a long range, self-guided propagation in the form of a filament [23].

2.1.2 Nonlinear Photon Absorption and Propagation

The phenomenon of carrier excitation by direct absorption of photons is generally called photoionization. In the simplest case, the laser linearly deposits energy into a material by creating an electron-hole plasma through single-photon absorption. However, the absorption cross section is very small at IR wavelength for wide bandgap dielectrics. Consequently, the only way such materials can absorb a sufficient amount of photons from an IR laser is through nonlinear processes which occur at very high intensities commonly described as strong electric field ionization (SEFI).

This can be explained by a simple consideration of a free electron of charge, e^- , interacting with linearly polarized light $E \exp(-i\omega t)$, where the position x of e^- under this harmonic motion can be given as:

$$x = -\frac{eE \exp(-i\omega t)}{m_e \omega^2} \quad (2.6)$$

Where e is the charge of an electron; m_e is the mass of an electron; $\omega = c / \lambda$ is the frequency of the laser source. Given the cycle-averaged intensity as $I = c\varepsilon E^2/2$ where c is the speed of light, ε is the permittivity of the dielectric material and E is the electric field amplitude.

Therefore, the cycled-averaged kinetic energy, Ponderomotive energy, U_p , the electron experiences due to laser exposure can be given as [24]:

$$U_p = \frac{1}{2} m_e \omega^2 \langle x^2 \rangle = \frac{e^2}{8\pi^2 m_e \epsilon_0 c^3} I \lambda^2 \quad (2.7)$$

$$U_p [\text{eV}] = 9.34 \times 10^{-20} \times (\lambda [\text{nm}])^2 \times I \left[\frac{\text{W}}{\text{cm}^2} \right] \quad (2.8)$$

Where $\lambda [\text{nm}]$ is the wavelength of the source in nm; ϵ_0 is the free space/vacuum permittivity. The nonlinear ionization process via SEFI occurs when the absorbed Ponderomotive energy is greater than the ionization potential or the bandgap energy of the system, E_g , $U_p > E_g$. For example, as shown in Figure 2-3, the ionization energy of most elements falls between 5 – 20 eV which corresponds to the intensity of 5 - 20 x 10¹³ W/cm² approximately for a source at 1030 nm [25].

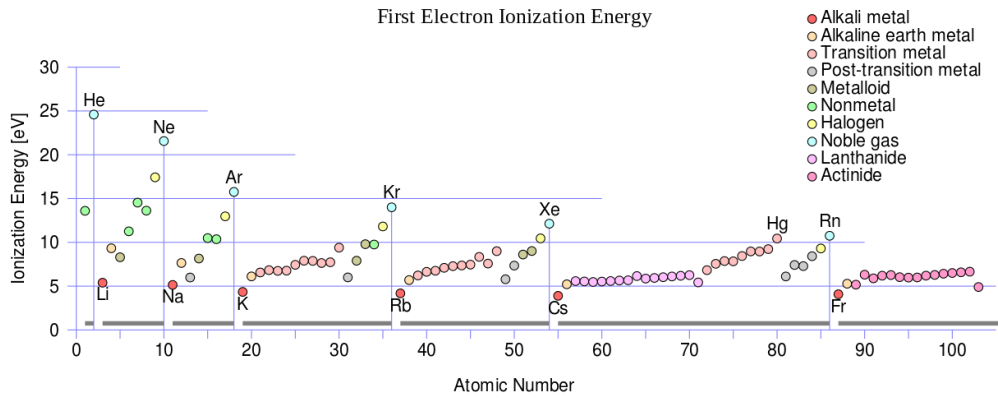


Figure 2-3 : Periodic trends for ionization energy (IE) vs. atomic number {copied from https://en.wikipedia.org/wiki/Ionization_energy}

Experimentally, it has been proven that, for the nonlinear multiphoton absorption inside a dielectric material of ultrafast laser radiation to occur, the peak intensity of the IR laser beam should be at least in the regime of 10¹² to 10¹³ W/cm². At these intensity values, simultaneous absorption of multiple photons is involved to excite a valence band electron. This type of photoionization by direct absorption of multiple photons is called multiphoton absorption. The rate of multiphoton absorption is expressed as:

$$\left\{ \frac{dN}{dt} \right\}_{MPA} = \sigma_m I^m \quad (2.9)$$

Where N is the density of electrons in the conduction band; I is the laser intensity and σ_m is the absorption cross-section related to m -photons process [7].

The number of photons, m , should be the minimum integer that satisfies the relation, $m\hbar\omega > E_g$, where $\hbar\omega$ is the single-photon energy; E_g is the bandgap energy of the dielectric material. Since the multiphoton absorption process is related to the peak intensity of the ultrafast laser beam, it is confined to the focal volume of the laser beam. It provides the initial seed electrons that are heated up by inverse bremsstrahlung forming a high-density electron gas in the conduction band through avalanche ionization processes [26].

Similarly, if the electric field strength becomes comparable with the atomic Coulomb potential, the electron can tunnel through the potential barrier. In this case, the tunneling time is given by the mean free time of an electron passing through a barrier of width, $l_{tunneling} = E_g/eE(t, \phi)$, where E_g is the ionization potential, e is the electron charge, and $E(t, \phi)$ is the optical field. Due to this inverse relationship between a barrier width and the applied optical field strength, for very high electric fields of the laser pulse, the Coulomb well is suppressed enough that the electron can tunnel through the short barrier and become excited to the conduction band. This type of photoionization is called tunneling ionization [27].

At high intensities of electromagnetic fields, the multiphoton and tunneling ionization processes compete. This behavior of an atom is commonly analyzed based on the Keldysh parameter which is given as:

$$\gamma = \frac{\omega}{e} \sqrt{\frac{m_e c n \epsilon_0 E_g}{I}} \quad (2.10)$$

Where ω is the laser frequency; I is the laser intensity at the focus; E_g is the ionization potential or bandgap energy of the material; m_e is the effective electron mass, e is the fundamental electron charge, c is the speed of light, n is the linear refractive index and ϵ_0 is the permittivity of free space [28].

The Keldysh parameter can be introduced to define the transition between the regimes of photoionization. For high frequency and moderate intensity of the laser, $\gamma > 1.5$, multiphoton ionization dominates. Contrarily, for very high intensity ($> 10^{14} \text{ W/cm}^2$) and lower frequencies, $\gamma < 1.5$, the laser radiation significantly modifies the Coulomb potential, i.e. tunneling ionization dominates the overall initial process of photoionization.

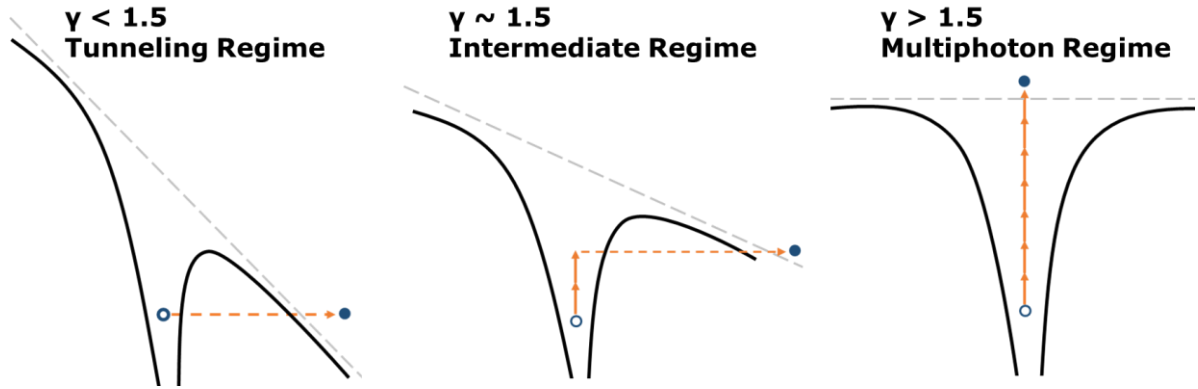


Figure 2-4 : Schematic diagram of the photoionization of an electron in an atomic Coulomb potential for different values of the Keldysh parameter. The grey broken line indicates the potential barrier. (Inspired by [22], [25]).

Figure 2-4 represents the schematic of the three regimes of photoionization described above. In the intermediate regime, i.e. $\gamma \sim 1.5$, the overall process of photoionization is a mix between multiphoton absorption and tunneling ionization. For instance, for our case with a laser source at 800 nm, for the given laser beam focusing conditions and material properties, the waveguide fabrication in both CaF_2 and Nd:YAG samples results $\gamma < 1.5$, i.e. 1.13 and 0.39 for CaF_2 and Nd:YAG respectively, in which the nonlinear ionization is interplay of both multiphoton ionization and tunneling ionization dominated by tunneling ionization specially for the Nd:YAG case [8].

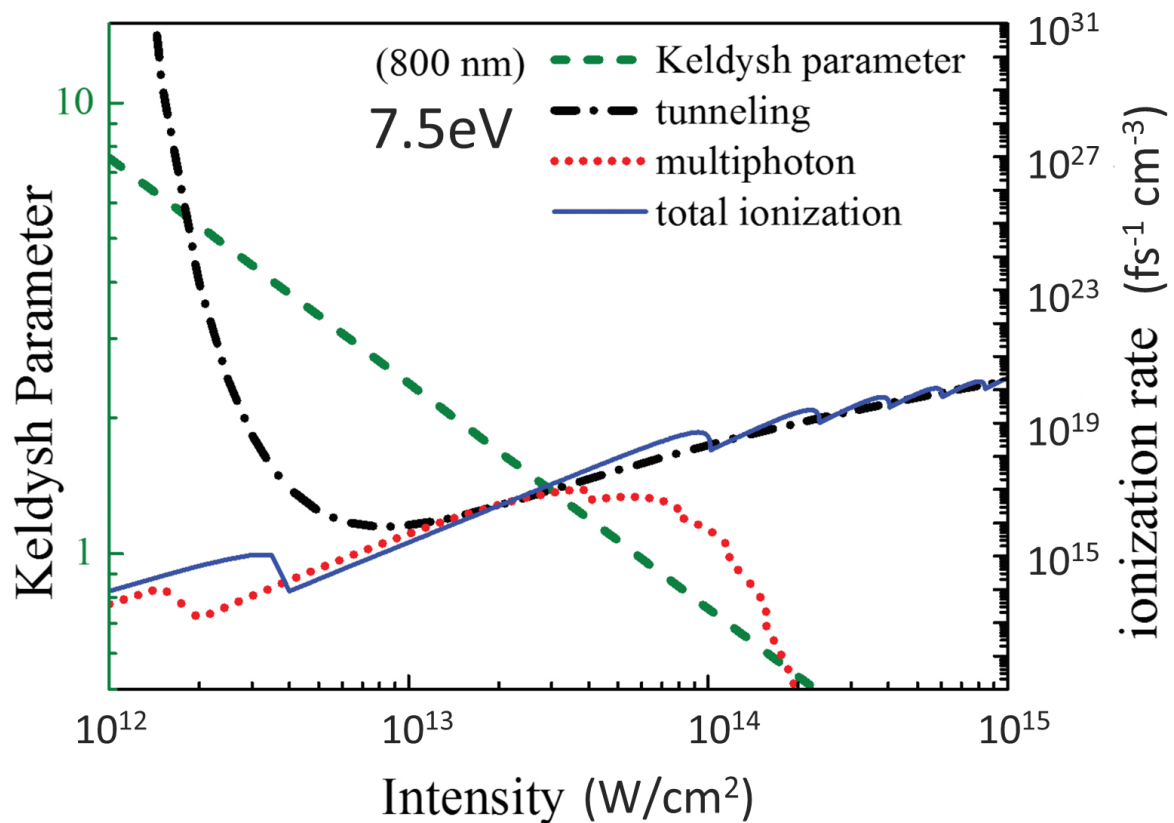


Figure 2-5 : The photoionization rate and the Keldysh parameter as a function of laser intensity for 800 nm light in fused silica (7.5 eV band-gap). The black dotted line describes tunneling only (equation (40) in [28]); the dotted red line shows multiphoton ionization only (equation (41) in [28]); and the solid blue line is for the full expression from Keldysh (equation (37) in [28]) {modified from [22] and [27]}.

In general, the Keldysh parameter provides a common framework for different photoionization processes which would have rather been described with totally different conceptual depictions and analytical formulations [22]. As it can be shown in the

Figure 2-5 above, the solid (blue) line represents the photoionization rate based on the full expression from Keldysh (equation (37) in [28]), the dotted (red) line represents the multiphoton ionization rate, the dashed and dotted (black) line represents the tunneling ionization rate and the dashed line represents the Keldysh parameter. Note that the multiphoton and tunneling rates overlap around a Keldysh parameter of 1.5.

The rate based on tunneling only (equation (40) in [28]) agrees with the complete formula up to a Keldysh parameter of just over 1.5, then overestimates the rate. Similarly, the rate based on multiphoton ionization only (equation (41) in [28]) agrees with the full formula for Keldysh parameters down to just below 1.5, then underestimates the rate.

In parallel to the direct nonlinear absorption of photons by valence electrons, for pulse durations longer than 30-50 fs [15], electrons already in the conduction band can also absorb photons, by phonon-mediated linear absorption processes, to get excited from the conduction minimum. These consequently can lead to inelastic electron-electron collisions. For the case in which after the sequential absorption of m photons by inverse Bremsstrahlung [29], where m is the smallest number satisfying the condition for multiphoton ionization, the colliding electron's energy from the minimum of the conduction band is more than the bandgap energy of the material.

As a result, this type of collision of an electron with another electron from the valence band would result two electrons near the minimum of the conduction band. This process of ionization by free-carrier absorption followed by impact ionization is called Avalanche ionization.

Figure 2-6 generalizes the above explained ionization processes. To initialize the process of avalanche ionization, 'seed' electrons need to be in the conduction band. These electrons can be provided either by thermally excited carriers, by easily ionized defect states, or in the case of ultrafast laser writing by carriers directly from photoionization [14], [22]. While the laser beam is present, the electron density, N , in the conduction band grows with the rate due to the avalanche process:

$$\left\{ \frac{dN}{dt} \right\}_{avalanche} = \beta NI \quad (2.11)$$

Where β is the avalanche ionization coefficient; I is the laser intensity.

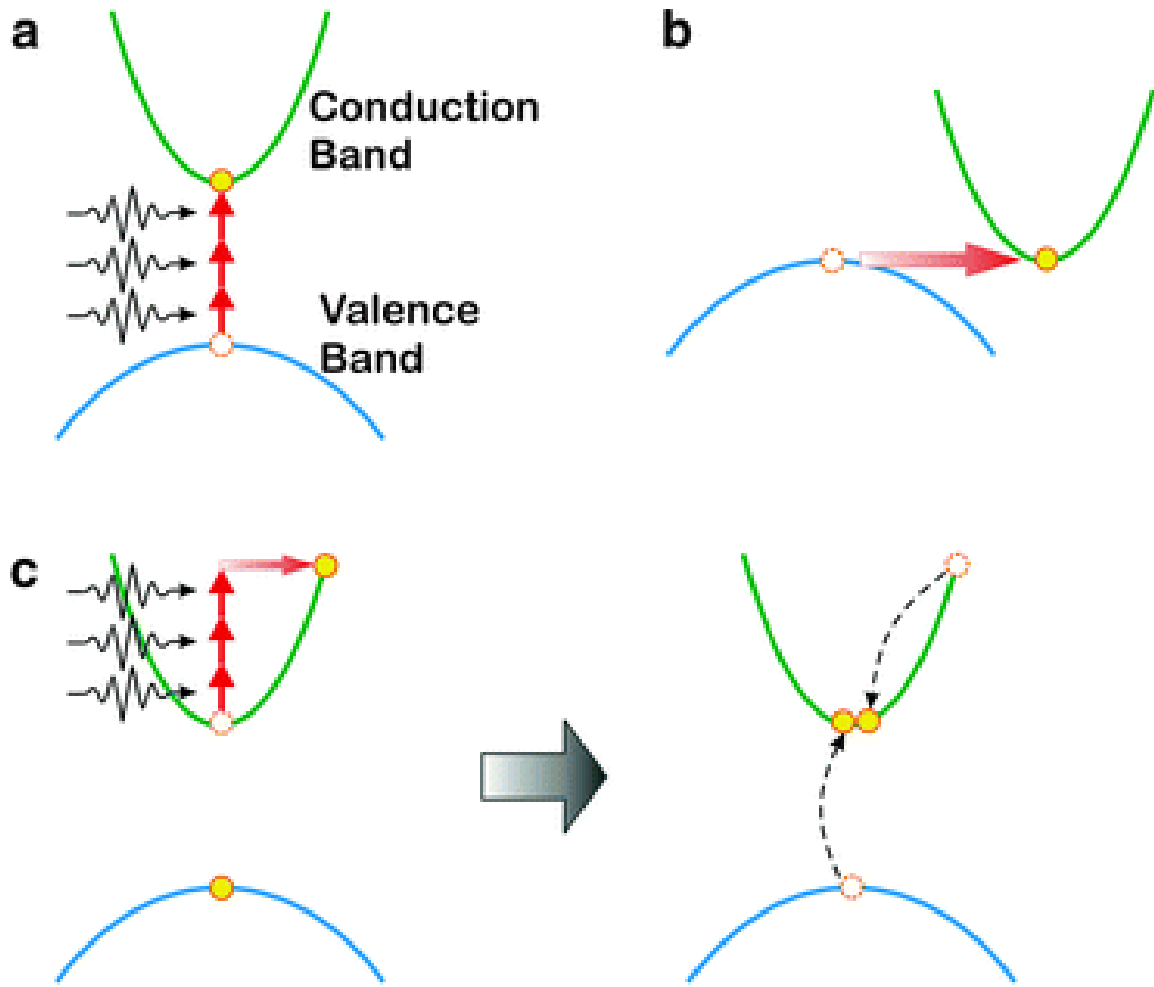


Figure 2-6 : Nonlinear ionization process dominating ultrafast laser writing. (a) and (b) show direct photoionization processes with multiphoton and tunneling ionization processes, respectively. (c) shows the avalanche ionization process [8].

Assuming the electron density of the plasma should reach a critical value to produce damage to the surrounding dielectric material, the dependence of the modification threshold on electron density can be fitted with the rate equations modeled as [30]:

$$\frac{dN}{dt} = \sigma_m I^m + \beta N I \quad (2.12)$$

Where the right side of the equation is the sum of both photoionization and avalanche ionization processes described in Equations (2.9) and (2.11), respectively for the multiphoton ionization dominating the photoionization process, i.e. $\gamma \gg 1.5$. This example of rate equation results in

an interpolation scheme describing the transition between two regimes that photoionization is strongly dominating at the center of the pulse to produce valence band electrons and it is less important when the peak passes while these electrons initiate the avalanche ionization which is more prominent with vanishing photoionization process at the edges of the pulse.

Consequently, once the avalanche ionization is in play, the electron density in the conduction band grows rapidly inside the plasma, with its natural resonant oscillation approaching the frequency of the laser [31] by which point it becomes strongly absorbing. N_c is the value of the critical plasma density as described in Equation (2.4).

It is commonly assumed that a critical density plasma must be formed to produce material damage. M. Sentis et al. developed a model that confirms this phenomenon for sub picosecond pulse duration above 50 fs. In this model, the temporal propagation of a pulse is described by a spatiotemporal dependence of the linear and nonlinear absorption by the medium as the electron plasma density evolves from sub-critical to over-critical [32]–[34]. This is explained in [30], as for intensities way above the threshold, the material is fully ionized with a thin layer of plasma on the order of a wavelength, in which the incident laser light no longer collisionally ionizes further electrons, but rather increases the average energy per electron forming dense, extremely hot plasmas [22]. This can be shown by using the Drude model which describes the absorption of the laser beam using the dielectric function, $\tilde{\epsilon}$, expressed as [14]:

$$\tilde{\epsilon} = 1 - \omega_p^2 \left[\frac{\tau^2}{1 + \omega^2 \tau^2} + i \frac{\tau}{\omega(1 + \omega^2 \tau^2)} \right] \quad (2.13)$$

Where τ is the scattering time depending on the conduction band electron energy, commonly a fraction of femtoseconds; ω is the angular frequency of the laser source while ω_p is the plasma angular frequency given as:

$$\omega_p = \sqrt{\frac{e^2 N_c}{\epsilon_0 m_e}} \quad (2.14)$$

Where ϵ_0 is the permittivity of free space; m_e is the mass of the electron; e is the charge of the electron; c is the speed of light and N_c is the critical density of electrons for the given source. For optical modification to occur, it is assumed that the electron density must reach the critical density, i.e. at $\omega_p \approx \omega$ [14][22].

In general, for very short pulses, tens of fs , in dielectric photoionization processes can overwhelm the overall process of the ionization as compared to avalanche ionization [35] while for longer pulses and for materials with greater band gap energies such as fused silica and sapphire, the avalanche ionization dominates the whole process [22].

2.1.3 Thermalization and Heat Dissipation

For sub picosecond pulses, the processes of energy absorption and ionization are more thoroughly understood than the plasma energy dissipation process [36]. Generally in light-matter interaction of homogenous dielectric materials, electron-electron and electron-phonon coupling are the main plasma relaxation mechanisms [37], while thermal diffusion and shockwave generation are the primary mechanisms of energy dissipation [36].

The first step of energy absorption is the relaxation of the electrons by carrier-carrier scattering, or electron-electron coupling, which results by thermalization of electrons. This process is highly dependent on the carrier density [15]. For lower excitation densities, the electrons basically interact with the equilibrium part of the electron distribution while for higher excitation densities, multiple collisions between non-equilibrium electrons dominate the process leading to rapid thermalization [37]. This thermalization process occurs within hundreds of femtoseconds and the lattice structure is still largely undisturbed. The second stage

of the thermalization process is related with the relaxation mechanism of the energy transfer of the electrons to the lattice in dielectric bulk materials. Temporally, this energy transfer process happens at the end of the laser pulse by efficient electron-lattice scattering. This process is called electron-phonon coupling and it is characterized by a temperature exchange process between electrons and phonons. This stage of the thermalization mechanism typically occurs on the time scale of 1-100 ps, depending on electron-phonon coupling strength of the material [15].

For a given pulse in the femtosecond regime, the electrons in the conduction band are heated much faster than they are cooled by phonon emission, and the pulse ends before the electrons thermally excite any ions [22]. It is only after the laser pulse is gone that thermal energy from “hot” electrons is deposited in shock-like form to the lattice [9]. This results in a shockwave or pressure within a couple of nanoseconds [22]. This is followed by diffusion of the thermal energy out of the focal volume (voxel) over a microsecond scale [9], [15].

It is this relative rate of energy deposition (shockwave generation) and thermal diffusion inside the focal volume of the lattice that primarily determine the damage threshold of the dielectric material during micromachining while the relative dominant process between the two probably depends on pulse fluence and repetition rate [9], [36]. For sufficiently high irradiance, the above thermal processes give rise to a temperature increase of the lattice inside the focal volume to several hundred or even thousands of degrees [15] leading to phase transitions, fusion and explosion in the latter part of the thermodynamic process.

While the aforementioned processes are well understood and largely material independent processes, the thermal and structural processes that follow leading to permanent modifications are material dependent and are still the subject of intense research. These processes result in physical, chemical and structural changes like densification [38], stress [39], and color center formation [40] particular to the material at micro volumes [26], [36].

For example, the refractive index modification induced within bulk materials is strongly dependent on the exact material composition and also the direct laser writing (DLW) parameters, especially on the repetition rate of the pulses [26].

The repetition rate or frequency of the laser is the main driving force behind the thermal effects within the focal volume in which the thermal diffusion relaxation time can be determined by the thermal diffusion coefficient, D_{th} , as [15]:

$$D_{th} = \kappa / \rho_0 C_p \quad (2.15)$$

Where κ is the thermal conductivity; ρ_0 is the density of the medium; and C_p is the specific heat capacity at constant pressure.

The heat will dissipate from the focusing volume within the diffusion time, τ_D as [41]:

$$\tau_D \approx 4\omega_0^2 / D_{th} \quad (2.16)$$

Where ω_0 is the beam waist for a Gaussian beam. For instance, in our experiments which will be discussed in Chapter 3, for CaF_2 crystals with a diffraction limited beam focused by a microscope objective of $\text{NA} = 0.42$ at a wavelength of $0.8 \mu\text{m}$, the thermal diffusivity and diffusion time are $3.58 \times 10^{-6} \text{ m}^2/\text{s}$ and $1.46 \mu\text{s}$, respectively. Therefore, a laser with a repetition rate below $1/\tau_D = 1/1.46 \mu\text{s} \approx 685 \text{ kHz}$, results in repetitive pulse-by-pulse modification where each pulse interacts with “cold” material. This regime is called athermal regime of writing.

As it is shown in Figure 2-7, the athermal regime of writing uses low repetition rate pulse trains, usually in the kilohertz regime, with high pulse energies up to a few micro joules. In addition, low NA objectives are used which gives longer working distances. In this case, the modified

volume reflects the shape of the intensity distribution, or the shape of the filament as it was shown with a sketch in Figure 2-2. Additionally, to create sufficiently smooth spatial overlap between consecutive pulses, the sample translation speed is limited to tens of micrometers per second making it susceptible for non-transient writing environment conditions [42].

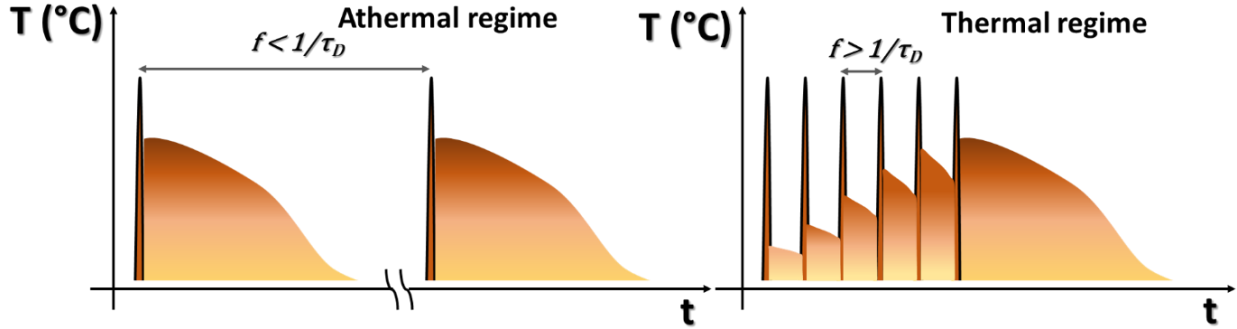


Figure 2-7 : Schematic diagram of two modification regimes in DLW. Athermal and thermal regimes of writing with low and high repetition rate of the pulses, respectively (inspired by [10], [26]).

In contrast, in the case of the thermal writing regime, for series of fs pulses at repetition rates higher than $1/\tau_D$, the gradually increased temperature of the sample is induced by successive pulses with repetition rates of hundreds of kilohertz to several megahertz with lower pulse energy. Therefore, high-NA objectives are used to achieve the modification threshold, for this regime limiting the longitudinal translation. Owing to the isotropic heat diffusion, as the sample is translated, the modifications formed are generally circular in this case and much larger than the size of the focal volume [26], [42], [43].

2.1.4 Parameters Affecting the Femtosecond Laser–Matter Interaction

In addition to the repetition rate of the laser source, micro-modifications inside crystals also depend on other irradiations parameters as well as physical material properties such as bandgap, dispersion, ionization rates and so on. To mention just a few:

- **Focusing conditions, i.e. numerical aperture of the microscope objective (NA):** can determine the energy needed to reach a threshold (E_{th}). With the threshold intensity and the critical power for self-focusing as free parameters, for diffraction-limited focusing with weak self-focusing, E_{th} can be expressed as [44][45]:

$$E_{th} = \frac{I_{th}\tau\lambda^2}{\pi(NA)^2 + I_{th}\lambda^2/P_{cr}} \quad (2.17)$$

Where I_{th} is the intensity for the modification threshold; λ is the wavelength of the source; τ is the pulse duration. Schaffer et al. demonstrated such a relationship experimentally on a number of materials, for details the reader may refer to Figure 7 of [22]. Given the range of NA's used, for the higher NA's, the threshold of modification usually starts below reaching the critical power, P_{cr} , thus self-focusing is negligible for this range while lower NA's significantly decrease the threshold energy for modification, E_{th} . On the other hand, large numerical apertures lead to a fast divergence of the beam after the focus leading to unstable filamentary propagation over a long length. Numerical apertures of value between 0.3 and 0.8 are most commonly used for microscope objectives for waveguide fabrication inside crystals [46].

- **Wavelength:** the threshold of modification, the resultant structures and the properties are strongly wavelength-dependent. Jia et al. have studied the wavelength dependence of laser-induced damage in CaF_2 and silica. Results showed a direct relationship with the threshold of optical breakdown, $E_{th} \sim \lambda$, for sources with visible spectra while the threshold stays constant for common laser sources in the near IR regime, i.e. $800 \text{ nm} < \lambda < 2000 \text{ nm}$. Further reading can be found in reference [46].
- **Pulse duration:** the dependence of the threshold of modification has been investigated over a wide range of different pulse durations τ (sub-50 fs to ns). Short-pulse damage exhibits a deterministic nature as opposed to the statistical behavior for long-pulse damage. Absorption occurs on a time scale that is short compared to the time scale for energy

transfer to the lattice, decoupling the absorption and lattice heating processes which is on the order of 10 ps [22][8]. Consequently, there was no dramatic increase of the modification threshold as the pulse duration was increased from 150 fs to 10 ps [30]. For pulses longer than a few tens of picoseconds, the generally accepted picture of bulk damage to defect-free dielectrics involves the heating of conduction-band electrons by the incident radiation. This model predicts the so called $\sqrt{\tau}$ scaling rule, which is a $\tau^{1/2}$ dependence of the threshold fluence upon pulse duration τ [30]. While for very short sub-100 fs pulses, the photoionization process dominates the avalanche ionization [47].

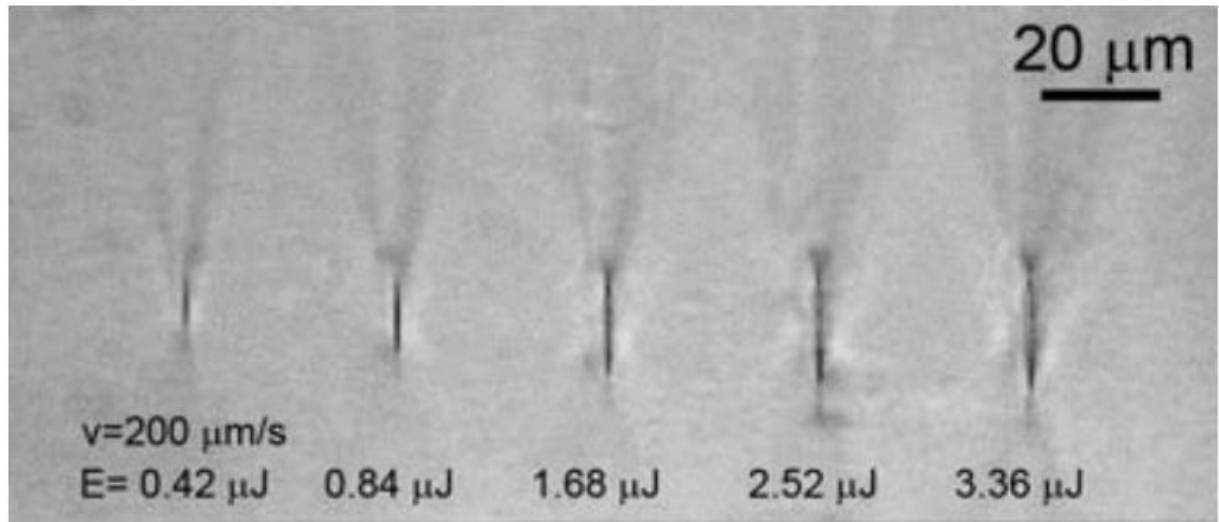


Figure 2-8 : Transmission microscope bright-field (BF) images of the damage tracks produced in a Nd:YAG sample by 120-fs pulses at a writing speed of 200 $\mu\text{m/s}$. The beam was focused from the top. (modified from [16]).

- **Pulse energy and energy intensity:** for a constant pulse duration, as the pulse energy increases beyond the threshold, the damage track elongates along the pulse propagation direction as shown in Figure 2-8.

This can be explained by the fact that increasing the beam energy enhances the spatial range of interaction between the focusing and defocusing effects due to refractive index variation and plasma, respectively, as it was explained in section 2.1.1.

2.2 Types of Modifications in Crystals

In general, following the irradiation of femtosecond pulses inside crystals, the induced morphological modifications along the tracks can be divided into two categories: smooth and severe damage regimes, or more commonly type I and type II modifications, respectively. The type I and II classification has recently been adopted for both crystals and glasses based on reference [48]. However, in the case of crystals, the type II classification scheme can be expanded to include type III waveguide configurations which are basically depressed cladding waveguide structures as it will be explained in section 5.1.

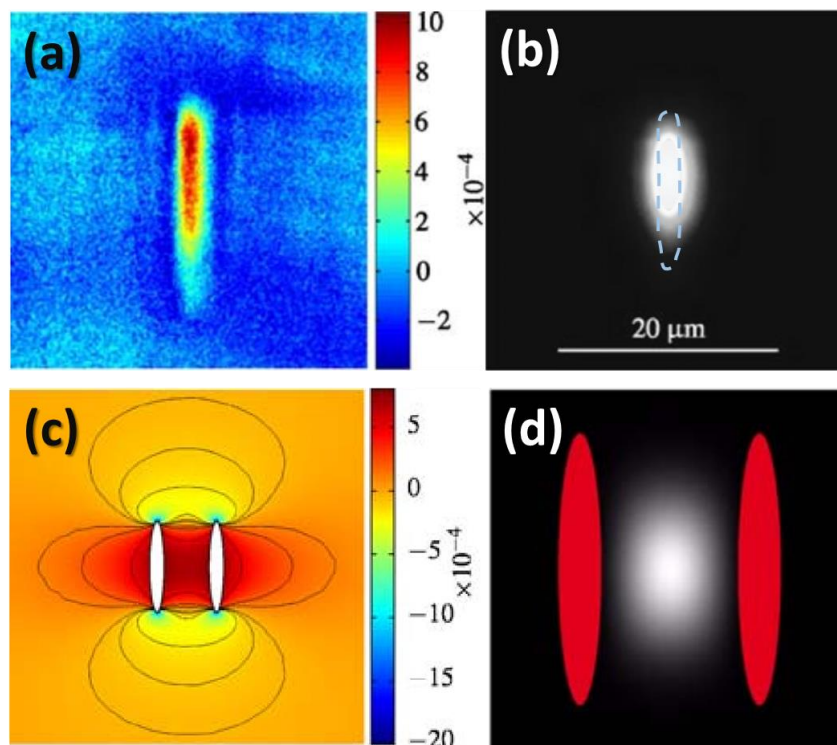


Figure 2-9 : Refractive index distribution of waveguides written inside LiNbO3 with type I and type II modification regimes in (a) and (c). The respective beam profiles that are guided along the modified zones are shown in (b) and (d), respectively. The broken line in (b) shows the modified track in (a) and the red ellipses in (d) depict the double damage tracks shown in (c). (modified from [49])

In the type I modification scheme, the changes are generally weak and guiding of light in this modification regimes occurs along the modified track, $\Delta n > 0$, only for one single polarization as shown in Figure 2-9 (a) and (b). Type I modifications have been observed only in a handful

of crystalline materials, for example Nd:YCOB [50], ZnSe [51] or mainly LiNbO₃ [52]–[57]. They have advantages like lower scattering losses and a potential of guiding longer wavelengths due to the possibility of scaling the modal cross-section by the multiscale technique. However, the refractive index changes can be thermally deteriorated or completely reversed in this case because the refractive index increase is induced by densification of the material which is difficult to achieve in crystalline materials as the lattice structure inside crystals can hardly be modified without inducing disorder and damage which generally lowers the index profile along the damage focal volume. In addition to their illusive nature, a thermal deteriorating property of type I poses a major drawback in their applications [49], [50].

Type II modifications are mainly generations of severe damage track along the propagation direction. These severe damages usually will lead to amorphization of the material and thus resulting in a lower refractive index, i.e. formation of voids, cracks and occurrence of microexplosions will lead up to volume increase in the focal volume. Simultaneously, in the vicinity of the damage tracks, as the inscribed tracks apply high pressure to the surrounding material and thus generate stress a stress field is created leading to a refractive index increase. Based on the fact that all dielectric materials have modification thresholds for optical damages and theoretically a lower refractive index cladding, or tracks, can be inscribed, these types of modifications are the most widely implemented for micromachining of crystals. Guiding can be achieved in this case by the strain which typically forms around the vicinity of the damage tracks as shown in Figure 2-9 (c) and (d). Due to this simplicity, these types of modification schemes are easily achieved in crystals and are most commonly applied for DLW fabricated waveguides. It is possible to achieve a higher contrast of refractive index in these types of modifications due to the fact that the inscriptions can be done in the window between the modification threshold and just below void formation, which is the result of micro explosions for extremely high fluence. In the case of crystals, this window is usually interchanged for the range of fluence between the threshold of modification and the threshold of crack formation, which is the result of high anisotropy of stress induced around the femtosecond laser modified volume. Even though, the modified tracks formed in this regime generally depend on the response of the material, crystals or ceramics, and the particular irradiation parameters of the laser source, the following observations are common [58]:

- i) Irreversible lattice damage at the core of the tracks probably due to accumulation of self-focused plasma volume giving rise to a continuous line of submicron-sized amorphous damage-voxels.
- ii) Compressed crystalline material with a high density of thermally removable defects and lattice imperfections in the vicinity of the filament's core.
- iii) Compressed crystalline material between filaments and in the surroundings of them, which is thermally stable.
- iv) Slight dilatation of crystalline material at the initial and final apexes of the tracks, which is also thermally stable.

Waveguides and compact lasers written in these schemes, type II, have been demonstrated in a wide variety of crystals, to mention just a few are garnet [58]–[62], lithium niobate [53], [56], borates [63], [64], sapphire [65]–[67], tungstate [68], [69], phosphate [70], vanadate [71]–[73], fluoride [74], [75] and so on. A more detailed list can also be found in [16].

2.3 Properties of Crystals

The term “crystal” derives from the Greek word “Krystallos” which means “ice”. In fact, the name is figurative and it is obvious that ice in the form of snowflakes or glaciers is crystalline. However, the word crystal includes a broad category of other forms of solid state matter, for example rock crystals.

Consequently, in the standard form the term “crystal” can be defined as solid-state bodies which are homogenous, anisotropic, and are composed of constituents that are strictly three-dimensional periodically ordered [76]. Thus, technically, crystals can be described as a lattice with a basis added to each lattice site as shown in Figure 2-10.

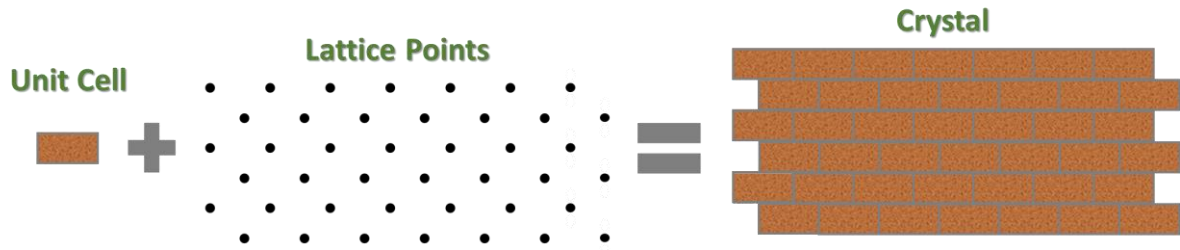
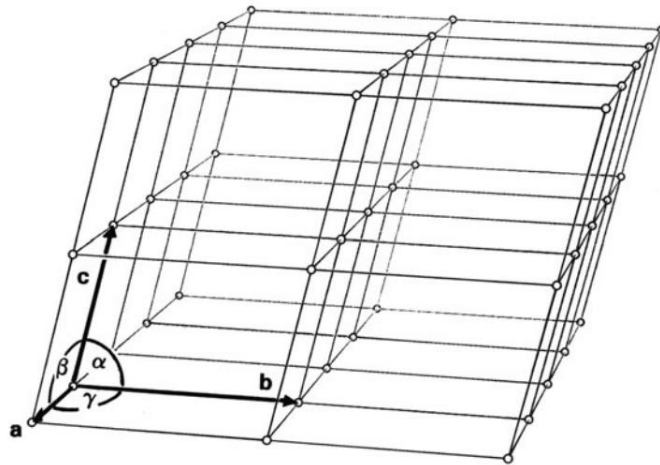


Figure 2-10 : Simplified model of a crystal.

In three dimensions, the basis, or commonly the unit cell, fills the geometrical space completely and is the smallest repeating volume of the lattice. This space filling characteristics of the unit cell infers that a given unit cell should be a parallelepiped. Therefore, lattice structures can be described as mere mathematical translations of three vectors \mathbf{a} , \mathbf{b} , \mathbf{c} of the unit cell, or more commonly as three lattice constants a , b , c (the lengths of the vectors) and by the three angles α , β , γ which separate these vectors from one another as shown in Figure 2-11. Unit cells are constituted by atoms, molecules or ions and their composition defines the composition of the entire crystal by extrapolation.

Figure 2-11 : Portion of a lattice. a , b and c are lengths of the cell edges and α , β and γ are cell angles between them.



In order to describe crystal structures clearly and unambiguously, various rules have been adopted concerning the choice and naming of the unit cell axes. In general, a "right-handed" system is chosen. This means that if the positive direction of a is directed forward and that of b to the left, then c must point upwards. Based on the translation between a , b , and c , also known as primitive translation vectors, and the angles α , β and γ , we can classify lattices in to

7 crystal systems based on restrictions of cell edges and angles as shown in a Table 2-1 below [77].

Table 2-1 : The seven crystal systems and the restrictions on their cell dimensions.

Restriction in	cell edges	cell angles
triclinic	none	none
monoclinic	none	$\alpha = \gamma = 90^\circ$
orthorhombic	none	$\alpha = \beta = \gamma = 90^\circ$
tetragonal	$a=b$	$\alpha = \beta = \gamma = 90^\circ$
hexagonal	$a=b$	$\alpha = \beta = 90^\circ, \gamma = 120^\circ$
trigonal	$a=b=c$	$\alpha = \beta = 90^\circ, \gamma = 120^\circ$
cubic	$a=b=c$	$\alpha = \beta = \gamma = 90^\circ$

Although the unit cell is a representation of the crystal in its smallest possible basis vectors, the best representation for crystals is the one that also includes symmetry elements, such as mirror planes, axes of rotation and centers of inversion. The choice of the unit cell for the description of a crystal structure will be that in which the highest possible symmetry is exhibited. This idea leads to the 14 Bravais lattices.

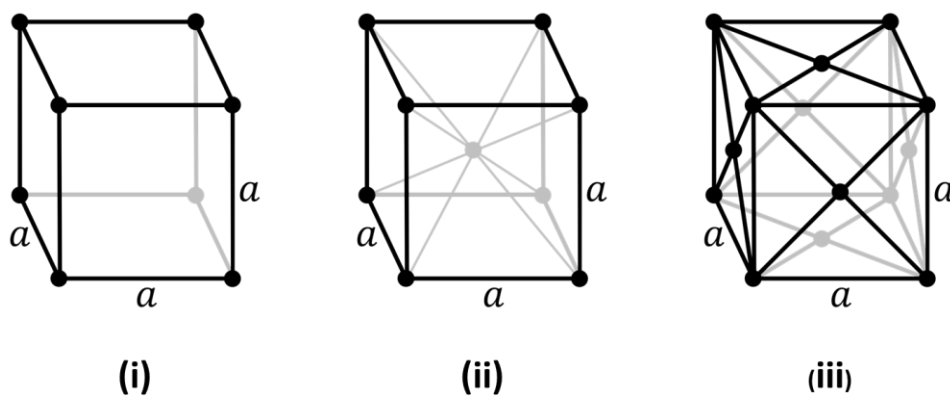


Figure 2-12 : Representation of Bravais Lattices of cubic crystal system. (i) The simple/primitive cubic (sc), (ii) the body centered cubic (bcc) (iii) the face centered cubic (fcc) lattices.

For example, as shown in Figure 2-12, there are three Bravais lattices with a cubic symmetry. One distinguishes the simple/primitive cubic (sc), the body centered cubic (bcc) and the face centered cubic (fcc) lattice with one lattice point on each corner of the cube, one lattice point

in the center of the unit cell in addition to the eight corner points and lattice points on the faces of the cube in addition to the corner lattice points, respectively.

Due to the strict arrangement of atoms, many physical properties of crystalline materials are directional dependent, hence anisotropic. However, depending on the type and quantity of properties such as the elasticity and thermal diffusion, a crystal might act as isotropic or anisotropic. To deal with these complex situations with single crystal properties, multidimensional arrays of numerical values or tensors are used. A simple example of tensor is stress, which is like pressure and is obtained by considering each of the six face areas in which the forces are acting on a cube, $\sigma_{ij} = F_i/A_j$, as shown in Figure 2-13 (a) below. Generally, stress can be expressed by second rank, σ_{ij} , as:

$$\sigma_{ij} = \begin{bmatrix} \sigma_{11} & \sigma_{12} & \sigma_{13} \\ \sigma_{21} & \sigma_{22} & \sigma_{23} \\ \sigma_{31} & \sigma_{32} & \sigma_{33} \end{bmatrix} \quad (2.18)$$

Any arbitrary stress can be decomposed in to 9 components, labeled as σ_{ij} ; where $i, j = 1, 2, 3$. Stress, strain, thermal conductivity, magnetic susceptibility and electric permittivity are all second rank tensors [78].

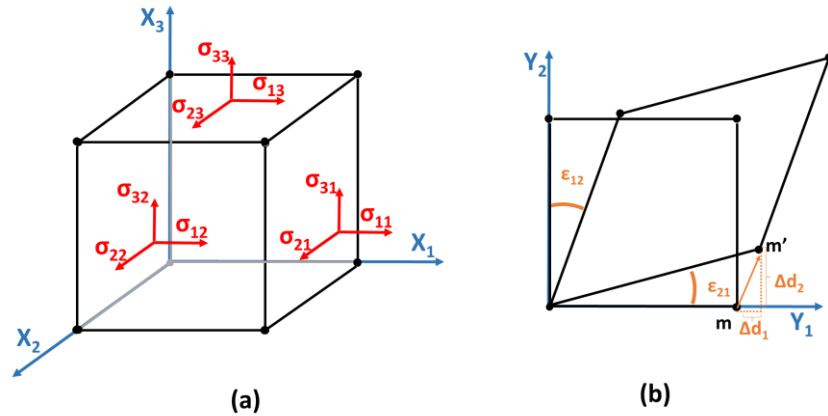


Figure 2-13 : (a) General three-dimensional representation of second rank tensor, e.g. stress. (b) Two-dimensional representation of strain with a square that is deformed to a parallelepiped.

Similarly, strain is defined as the relative change in position of points within a unit cell that has undergone deformation as depicted in Figure 2-13 (b). Inside crystals, strain, ε , can also be expressed with a second rank tensor matrix as in Equation (2.18). The intrinsic property of any crystalline material in relation to reversing deformations is called elasticity. By considering the fact that both stress and strain are symmetric tensors, the elastic properties relate stress and strain as:

$$\varepsilon_i = S_{ij}\sigma_j \dots \dots [i, j = 1, 2, 3, 4, 5, 6] \quad (2.19)$$

Where S is the elastic compliance. The number of elastic constants, i.e. S_{ij} , needed to completely describe the elasticity of the crystal depends on the crystal symmetry. For example, thanks to the diagonal symmetry, for cubic crystals of all symmetry classes only three elastic constants are needed: c_{11} , c_{12} and c_{44} [79].

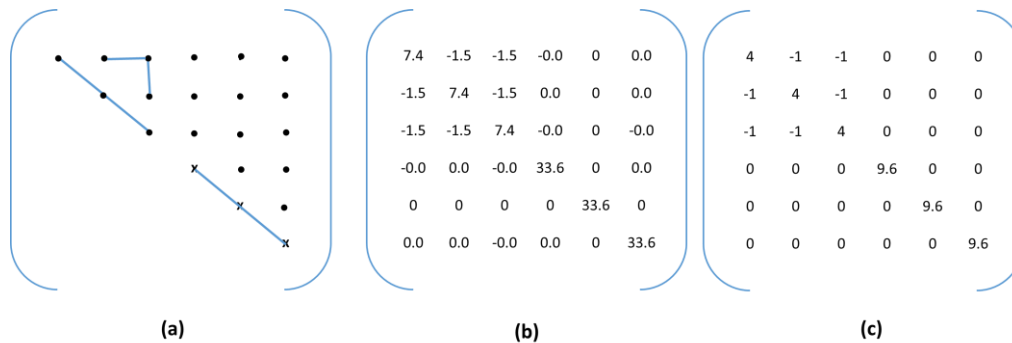


Figure 2-14 : (a) Tensor representation of the form of the elastic compliance tensor for cubic crystallographic systems. Standalone dots represent zeros; dot and a line represent equal components; X represents 2 fold ($S_{11}-S_{12}$) approximately while the interconnecting line indicates that they are equal (inspired by [79]). (b) and (c) show elasticity, 10^{-12}Pa^{-1} , of CaF_2 and YAG respectively (data from [80]).

Figure 2-14 shows a fourth rank tensor representation of cubic crystals which is highly simplified due to symmetry. As it can be shown in Figure 2-14 (b) and (c) that the CaF_2 shows less stiffness as compared to YAG. Further comparisons in terms of spectroscopic and thermodynamic properties between the two will be presented in the next section.

2.4 Crystals of Interest: Nd:YAG and CaF₂

Crystals can be divided into 2 groups based on how the velocity of light of a particular wavelength propagates in the material. Crystals whose refractive index does not depend on the direction that the light travels are called isotropic materials. While crystals whose refractive index does depend on the direction that the light travels, polarization, are called anisotropic materials. These types of materials will have a range of refractive indices between two extreme values for each wavelength.

The tetragonal and hexagonal crystal systems are uniaxial and are characterized by 2 extreme refractive indices for each wavelength. While the triclinic, monoclinic, and orthorhombic crystal systems are biaxial and are characterized by 3 refractive indices, one of which is intermediate between the other two.

As it was described above, isotropic crystalline materials exhibit a uniform refractive index in any arbitrary direction. Thus, owing to this direction independent uniform property, optical specificities and restrictions of low-symmetry crystal optics are neglected for cubic crystals which enables a more simplified systematic approach to study modifications due to femtosecond DLW inside crystals along the damaged tracks. In this thesis work, the focus is on more and better understanding and an approach for qualitative and quantitative characterizations in both waveguiding and luminescence properties of modified cubic crystals, namely Yttrium Aluminum Garnet (YAG) and Calcium Fluoride (CaF₂).

Calcium fluoride (CaF₂) is a dielectric crystal which crystallizes in a cubic fluorite structure, space group Fmm3 [81]. The cation positions correspond to the closest packing and each unit cell has four Ca atoms and eight F atoms as shown in Figure 2-15. With its high transparency in a broad wavelength range, a low refractive index, and a low phonon energy, CaF₂ is used as commercial optics material from the infrared to the ultraviolet region, such as for windows [82].

Figure 2-15 : Unit cell of CaF_2 . The black balls represent the Ca atoms, and the green balls represent the F atoms [83].



One of the most important challenges when designing high power laser systems is the selection of the gain medium. Although single crystals are generally challenging to grow, they are implemented more often than non-crystalline hosts, when scaling up diode-pumped laser systems to high power. This is because of the fact that crystalline materials have a lower pump threshold, better Q-switching stability, and better thermal conductivity [84].

Ytterbium-doped YAG materials are, so far, the most important and developed ones due to their low Stokes-shift (very often incorrectly called “quantum defect” in the laser community), long fluorescence lifetime and the match of the absorption wavelength with commercially available high-power pump diodes, which are the main budget driving factors behind high power solid state systems.

Similarly, CaF_2 was identified among the first host crystals for active laser media [85],[86] during the 1970s. However, due to the need of charge compensation of the Nd^{3+} -ions required to keep the electric neutrality within the fluorite crystal and the difficulty of its growth other host materials like YAG, or oxide and fluorite glasses were preferred over the years. Recent developments made on ytterbium-doped alkaline-earth fluorides have shown that it is possible to have a better scalability of the crystal growth as well as a very high thermal conductivity, a high laser-induced damage threshold, a longer emission lifetime, a lower nonlinear refractive index and a large emission wavelength tuning range. Due to these reasons, Yb-doped CaF_2 has once again proved to be a competitive material for high-energy and high-power applications,

further readings can be found in [13], [82], [87]–[91]. Table 2-2 presents a comparison of the spectroscopic and thermodynamic properties of YAG and CaF₂ crystals.

As shown in the Table 2-2 below, it is obvious that the absorption cross sections are about the same for Yb-doped YAG and CaF₂. However, the emission cross section of YAG exceeds that of CaF₂ by more than a factor of 10, in favor of YAG. Therefore, better pumping efficiency is achieved in the case of Yb:YAG. On the other hand, the emission lifetime of Yb:CaF₂ is twice longer which make it favorable for a use as gain medium of pulsed laser amplifiers [90].

Table 2-2 : Comparison of properties of Yb-doped YAG and CaF₂ (copied and modified from [13])

Laser Host	YAG	CaF ₂
<i>Spectroscopic and Laser Parameters</i>		
Absorption peak wavelength [nm]	942	979.8
Peak absorption cross section [10^{-21} cm ²]	8	5.4
Laser wavelength, λ_l , [nm]	1029	1049
Emission cross section at λ_l [10^{-21} cm ²]	20	1.7
Lifetime [ms]	0.95	2.4
Demonstrated tuning range [nm]	1020 - 1083	1000 - 1072
Refractive index at λ_l	1.815	1.429
Nonlinear refractive index [10^{-20} m ² /W]	6.2	1.3
Saturation Fluence, F_{sat} (J/cm ²)	9.6	80
<i>Thermo-optical and mechanical parameters</i>		
Hardness [mohs]	8 – 8.5	4
Thermal expansion coefficient [10^{-6} K ⁻¹]	6.7	19
Young Modulus E [GPa]	280	76
Thermal conductivity [W m ⁻¹ K ⁻¹]	10.7	9.7

Yb:CaF₂ has also demonstrated a wide tuning range and generation of ultrashort laser pulses (about 100 fs) which is considerably shorter than that of Yb:YAG. Moreover, the nonlinear refractive index is around four times smaller than in the case of YAG, [92], and also the refractive index is lower, which makes them suitable as intermediate systems in laser cavities, i.e. as cavity spacer [93].

For undoped crystals, the thermal conductivity of both crystals is significantly high and almost the same between the two, which is crucial for high power laser applications [89]. However, the Yb-ion concentration in the case of CaF₂ corresponds to twice that of YAG, for example 2.5 % Yb in CaF₂ is equal in density to 5 % in the case of YAG. This has a consequence on the thermal conductivity as the dopant ions introduce lattice defects which result in diminishing thermal conductivity with respect to the undoped matrix [94]. Thus, the thermal conductivity decreases less in the case of Yb:CaF₂ than for Yb:YAG [13].

2.5 State-of-the-art of Direct Laser Writing inside Crystals

Femtosecond laser micromachined crystalline waveguides can be implemented in many different technological issues of photonics. Some of the components demonstrated for integrated optics inside crystals are:

- **Electro-optic modulators:** have been fabricated with a Mach–Zehnder interferometer (MZI) configuration in LiNbO₃ crystals [95]–[98].
- **Three-dimensional waveguide splitters:** pave a way to produce direct-pump compact integrated laser devices on chip scales for beam splitting in dielectric laser crystals for various photonic applications. With a photonic-lattice-like cladding approach, Nd:YAG splitters capable of 1 to 2 and 1 to 4 beam splitting, for pumps at 808 nm and 1064 nm wavelength with slope efficiencies of 34% and 22% were realized [99].

- **Frequency converters:** can be realized in nonlinear crystals. As compared to bulk, waveguides enhance the efficiencies of second-harmonic or higher-order generation. Readers are encouraged to refer to Table 1 of [16] which summarizes literatures for SHG in fs-laser micromachined crystal waveguides.
- **Waveguide lasers:** possess lower lasing thresholds, comparable efficiencies and compact geometries as compare to bulk solid state lasers. Both type II and type III waveguide configurations have been realized and intensively studied. Readers might find a complete list of reviews for waveguide lasers inside crystals in Table 2 of [16].

In relation to our crystals of interest, a number of works have reported on ytterbium and neodymium doped YAG crystals. Slope efficiencies above 70% [100], also known as a parasitic process achieved by simply polishing the end facets, and continuous wave output powers of more than 5 W were reported by T. Calmano et al. [101]–[106]. The same group demonstrated a passively Q-switched waveguide laser with repetition rate of 300 kHz at 300 mW [107]. While this group has been more dedicated on type II waveguide configurations, the group of A. Okhrimchuk (Moscow, Russia) et al., focused more on depressed cladding, type III, waveguides inside YAG crystals [60], [108], [109]. They have demonstrated a microchip type III waveguide laser operating in Q-switched mode [109] and a 11-GHz waveguide laser mode-locked with a single layer of graphene [110]. Beside these two groups, a number of studies and characterization of waveguides inside doped YAG samples have been demonstrated, readers are encouraged to refer to [59], [108], [111]–[114].

While there are a number of studies about waveguides inside YAG, the study of femtosecond laser written waveguides inside CaF_2 has been so far ignored and only a few works have been performed [75]. Recently, R. Graf et al. categorizes the type of modifications inside CaF_2 as pearl-chain type [115] which makes it difficult to achieve waveguiding [116]. The only significant recent work was the fabrication of Yb,Na:CaF_2 depressed cladding waveguides produced by the DLW technology [117], in which dual-wavelength laser emissions, at 1013.9 nm and 1027.9 nm, with an optical-to-optical conversion efficiency as high as 45.3% and a pulse energy of 0.13 μJ was demonstrated. Just recently, Babu et al. reported double track

cladding inside Nd^{3+} , Y^{3+} co-doped CaF_2 crystals with refractive index, birefringence, transmission loss and micro-luminescence studies as a function of the double track separation [118].

In the upcoming chapters, the work of this thesis on double track waveguides achieved both inside Yb-doped YAG and undoped CaF_2 crystals will be presented. To the best of our knowledge we have demonstrated the first double track waveguides inside CaF_2 samples [119] with good guiding properties. Moreover, a detailed description for new characterization approaches of those waveguides is given, which opens a new venue in the field of direct laser writing in crystals and in other dielectric materials.

3 Experiment in Femtosecond Laser Structuring

3.1 Experimental Set-up

In its fundamental form, a femtosecond laser writing setup consists of a high-power radiation source, a beam delivery system and a programmable 3-axis stage. Figure 3-1 shows the basic components of the direct laser writing setup from pulse beam generation to delivery of the pulse at the focal volume inside the dielectric crystal sample.

3.1.1 High Power Source

The femtosecond laser beam, which is utilized for most of the work, was delivered by RegA 9000 laser system, from Coherent Inc. the laser system chain is constituted by a femtosecond oscillator, a regenerative amplifier and a stretcher/compressor.

Femtosecond Oscillator

The Chameleon Vision S, customized, is pumped at 532 nm by a Verdi solid state laser, to produce an 80-MHz pulse train centered at 800 nm with pulse energies on the order of 40 nJ. The mode-locking occurs via Kerr-lens mode-locking applying a material exhibiting the nonlinear Kerr effect reducing the beam size when mode-locked together with a slit that introduces losses to larger, continuous wave beams.

The mode-locking is initiated by a reflective starter assembly that can modulate the cavity length and phase locks the longitudinal modes of the laser. The final pulse width is established due to an interplay of pulse broadening due to self-phase modulation and negative dispersion induced from a prism pair inside the cavity to achieve soliton mode-locked pulses with a duration of 75 fs.

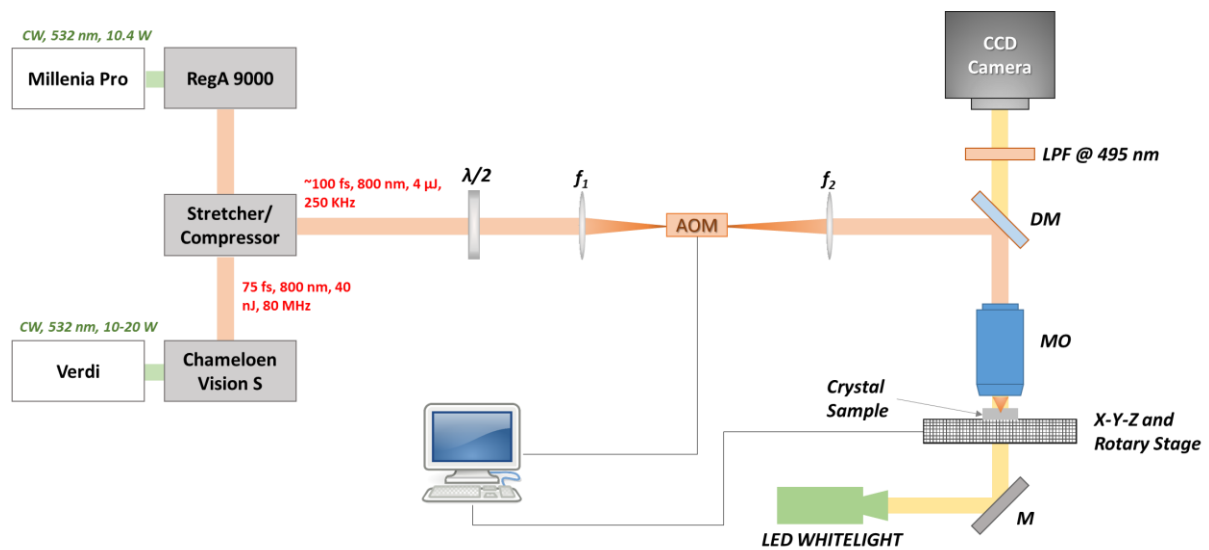


Figure 3-1 : The summary sketch of the 3D direct laser writing setup. $\lambda/2$ – half-wave plate; f_1 – 1000 mm convex lens; f_2 – 500 mm convex lens; AOM – Acousto Optic Modulator; DM – dichroic mirror; LPF – long pass filter; MO – microscope objective; M – mirror. The AOM and 3-axis stage are synchronized and computer controlled. An LED white light source and a CCD camera enable in-situ imaging of the sample during fabrication.

Regenerative Amplifier

Although the Chameleon Vision S is capable of generating stable 40 nJ pulses, both the pulse energy and repetition rate are not yet sufficient for femtosecond fabrication. The RegA 9000 Laser is configured as regenerative amplifier to select incoming pulses of the oscillator, at the repetition rate of 250 kHz and amplify them to approximately 4 μ J/pulse. The RegA 9000 is a Titanium:sapphire amplifier and is pumped using the all solid-state laser from Spectra-Physics model Millenia Pro with 10 W of continuous wave (CW) output power at 532 nm. The regenerative amplifier uses acousto-optic components to inject/eject pulses, using a cavity

dumper. The acousto-optic components are driven by an radio frequency (RF) signal clock arising from the photodiode signal placed at the oscillator and the configurable internal clocking mechanism generated by the system controller.

Stretcher/Compressor

The RegA laser system employs chirped-pulse amplification (CPA) method. Therefore, a stretcher/compressor module of the RegA laser system chain is placed between the Chameloen Vision S and RegA 9000 stretching the pulse coming from the seeder to around 40 ps and recompressing the amplified stretched pulse from the amplifier back to around 100 fs. The core of the stretcher/compressor module is a holographic diffraction grating.

3.1.2 Beam and Pulse Control

Beam Shaping and Polarization

The polarization of the linearly light ejected from the compressor module is rotated using the half-wave plate to give maximum optimized efficient output at the acousto-optic modulator (AOM). A telescope arrangement of f_1 and f_2 lenses is used to give an optimum beam diameter at the AOM core, 2 mm x 2mm, and at the microscope objective diaphragm, 6 mm to 10 mm, in the meantime, the microscope objective tightly focuses the beam inside the sample. It is worth to note that the beam shaping arrangement described above results in a polarization parallel to the designated y-axis at the 3D-stage.

Pulse Shaping and Picking

The pulse energy was modulated by a computer controlled arbitrary waveform generator, Agilent 33250A, which drives the fixed frequency source that generates the RF signal for the

AOM with a first order frequency shift of 110 MHz. Consequently, this provides the user with complete flexible control of energy and exposure time of the pulse train on to the sample down to single pulse picking.

3.1.3 3D Trajectory

The three dimensional trajectory of the writing tracks is achieved by placing the sample on a slide which is attached to micro-controlled Newport Corporation X-Y-Z stages, XMS50, with a spatial resolution of 0.04 μm along the predetermined path.

3.1.4 Power and Trajectory Control

An XPS Universal Motion controller from Newport Corporation is used to offer a configuration wizard for the XMS50 three-dimensional stages while the Agilent 33250A provides a configuration tool for RF supply to the AOM. The laboratory grown IGOR program with the Graphic User Interface (GUI) is used to control both the power, by setting the RF voltage of the AOM, and 3D trajectory using the XPS server that manages the assigned line-arc trajectory motion groups of the three-dimensional stage.

3.2 Protocol for Laser Structuring

In addition to the aforementioned components, a detailed procedure for the fabrication is explained below:

- The RegA chain, with RegA 9000 seeded with the Chameleon Vision S, is turned on and the system normal start up is controlled by the oscilloscope output connected to the RegA system control.

- In order to enable an automated control and lock of the stages, the XPS server should be turned on.
- Similarly, the power supply to the AOM and the Agilent should be turned on.
- Using the GUI, both the XPS server and the Agilent are initialized to build up the communication.
- After warming up the laser for a sufficient duration, the output power from the laser can be measured for reference, by placing the powermeter, to measure the first order diffraction, just after the AOM at the maximum driving RF voltage, which is 4.95 volts in this case. Figure 3-2 shows the nonlinear relationship between the AOM RF voltage and the corresponding fraction of maximum power of first order diffraction.

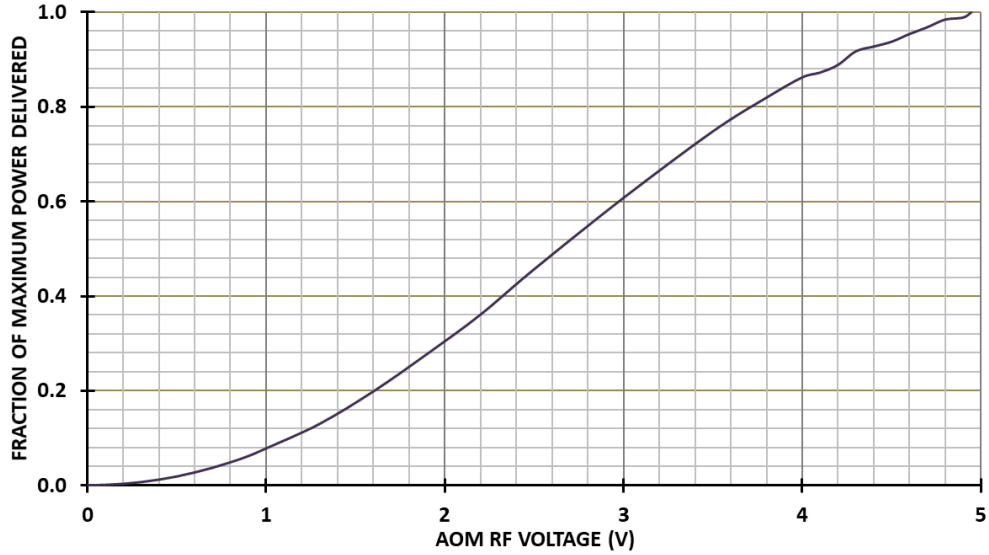


Figure 3-2 : Relationship between AOM RF Voltage and the fraction of peak power delivered.

The pulse energy, E_p , can be given as:

$$E_p = \frac{P_{max} \eta_{AOM \rightarrow P}}{f} \quad (3.1)$$

Where P_{max} is the maximum first-order diffraction; $\eta_{AOM \rightarrow P}$ is the fraction of the P_{max} diffracted at the AOM which is given as a nonlinear function of the AOM RF voltage as shown in Figure 3-2; and f is the repetition rate of the source.

- The beam is then centered on the center of the consecutive pinholes along the path of the beam until the entrance of the microscope objective.
- By setting the power at a relatively safe percentage the beam can be focused on to the surface of the sample, i.e. below the threshold for surface ablation, and the back reflection is monitored on the screen connected to the CCD camera. The symmetry of the beam along the longitudinal direction is performed by horizontal and vertical adjustment of the mirror that is just before the entrance of the objective. When the beam is no more tilted the focusing and defocusing on the surface using the longitudinal z-axis of the stage becomes symmetrical or untilted.
- After the optical path is aligned, the preferred objective is selected and the low power beam can be used to achieve back reflection, at the focal plane of the objective, from the surface of the sample on to the CCD camera.
- Once the beam focus is located on the surface of the sample, all the manual trajectories of the XPS server are locked to automatic and the sample will be longitudinally moved upwards to $150\text{ }\mu\text{m}$ mechanically, to achieve a focal volume around the depth of $150\text{ }\mu\text{m} \times n$, where n is refractive index of the sample.

4 Fabrication of Waveguides

The femtosecond laser inscription setup and protocol of the previous chapter is applied on two differently cut CaF_2 samples to inscribe double track waveguides, which will be discussed in Sections 4.1 and 4.2. Although the main task was to identify the writing parameters, the crystal samples which were cut along the defined principal axes exhibited anomalies, namely smooth modification and non-reciprocal writing, which were reported only in a handful cases so far. This will be detailed in Section 4.3.

4.1 Modification Threshold and Crack Formation

The GUI based software developed using IGOR allows flexible control of the modulated power of the pulses by the RF function generator and arc-line trajectories using the XPS server. Once the beam is focused inside the sample, we can identify the damage threshold using a matrix of number of pulses and the AOM RF voltage. In transversal writing of tracks, the number of pulses crossing each point can be related with the speed of writing as a product of time to intercept a point and repetition rate of the laser. The speed of writing (v) can be given as:

$$v = \frac{2\omega_0 f}{N} \quad (4.1)$$

Where $\omega_0 = 0.6 \lambda/NA$ is the diffraction limited beam waist; λ is the wavelength of the laser source; NA is the numerical aperture of the objective; f is the repetition rate of the laser source; and N is the number of pulses crossing each point.

In order to identify the threshold of modification and crack formation, we start by inscribing a point matrix with coarse AOM voltage and number of pulses then we tune around the threshold and crack formation as shown in Figure 4-1 below.

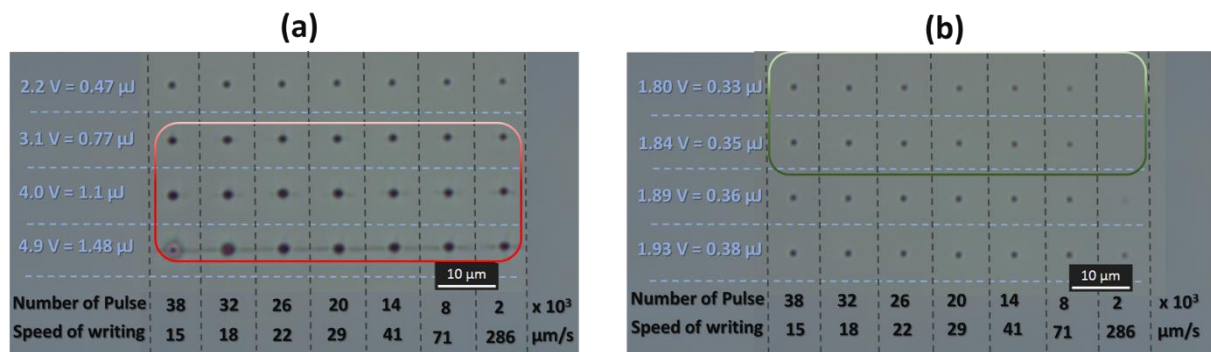


Figure 4-1 : Optical micrograph of femtosecond inscription of matrix of number of pulses/speed of writing (μm/s) and RF voltage (v)/energy of writing(μJ) for undoped CaF₂ sample. (a) shows coarse modifications; (b) shows fine tuning around the threshold of modification. The red rectangle shows crack formation while the green rectangle shows the threshold of modification.

As it is shown in the figure above, the pulse energy plays a more prominent role for the threshold of modification and crack formation. This can be evidenced from the fact that with the repetition rate of the laser source used, the writing process is in an athermal regime which was explained in Section 2.1.3 with a CaF₂ sample used in our case as an example. Figure 4-1 (a) shows that an energy of 0.77 μJ and above results in crack formation, enclosed by the red rectangle, while 0.47 μJ is still above the threshold of modification.

In its second part, the threshold of modification, which is the point where modifications start to be observed, is identified. The writing pulse energy is decreased below 0.47 μJ and the threshold point was observed around a pulse energy of 0.36 μJ . Then, by fine tuning around 0.36 μJ as indicated in Figure 4-1 (b) results the threshold of modification of 0.33 μJ , enclosed with a green rectangle. Similarly, to find the threshold of crack formation, the pulse energy was fine-tuned around 0.77 μJ to find the crack formation threshold of 0.61 μJ .

4.2 Waveguide Inscription

In parallel to the threshold of modification and crack formation, waveguide tracks were studied, or short lines, i.e. fabrication inside two groups of single-crystal samples of undoped CaF_2 . The first sample had faces parallel to some main planes, i.e. polished faces parallel to $[11\bar{2}]$, $[\bar{1}10]$ and $[111]$ planes (Sample A) as shown in Figure 4-2 (a). While the second sample had faces randomly cut and parallel to $[04\bar{3}]$, $[1\bar{3}\bar{4}]$ and $[611]$ planes (Sample B) as shown in Figure 4-2 (b). The x and y axes of CaF_2 are assigned as the short and longer sides in which the x axis of the crystal is perpendicular to the plane $[\bar{1}10]$ and $[1\bar{3}\bar{4}]$ while the y-axis of the crystal is perpendicular to the plane $[111]$ and $[611]$ in Sample A and Sample B, respectively.

A number of short tracks, of 150 μm in length, were inscribed 150 μm below the surface with the scan speed varying between 10 $\mu\text{m/s}$ to 1000 $\mu\text{m/s}$ and with various pulse energies ranging between 0.36 μJ to 0.72 μJ , which correspond to numbers of pulses per spot (N) between 570 to 57000 and fluences (F) between 8.7 J/cm^2 to 17.5 J/cm^2 , respectively. We were surprised to notice smooth modification in the case of Sample A for an approximate scanning speed between 200 $\mu\text{m/s}$ to 300 $\mu\text{m/s}$ for certain polarizations with respect to the crystal axes, energy and direction of writing. In addition, this was not observed in the case of the Sample B in which low loss waveguides were inscribed as it was discussed in the section 4.2 and Chapter 5.

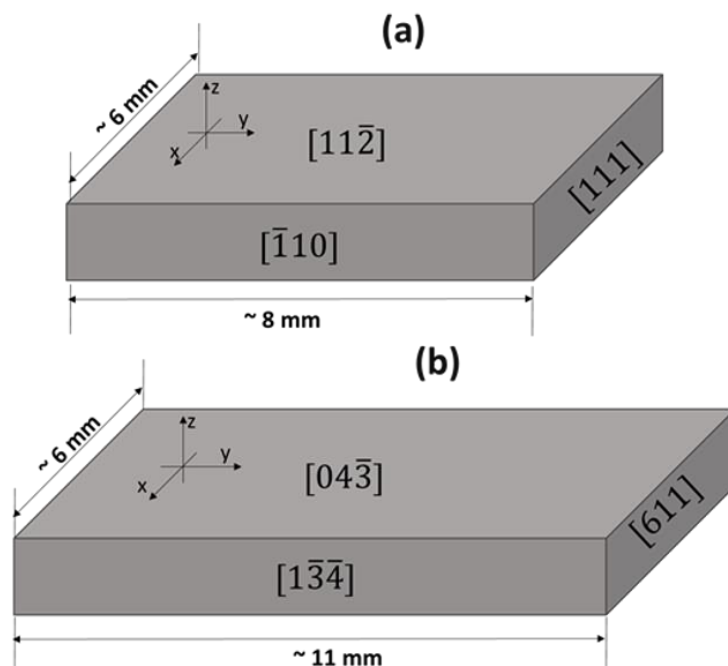


Figure 4-2 : Sketch of two undoped CaF_2 samples used for waveguide track fabrication. (a) shows the sample Group A with polished faces parallel to $[11\bar{2}]$, $[\bar{1}10]$ and $[111]$. Similarly, (b) shows the sample Group B with polished faces parallel to $[04\bar{3}]$, $[1\bar{3}\bar{4}]$ and $[611]$.

Thus, once the threshold of modification and crack formation are identified for a sample B, we can inscribe waveguides between these two extremes to study and understand the characteristics of the waveguides due to the effect of different parameters like writing energy, distance between tracks, writing speed, numerical aperture of the objective and so on. For example, for the undoped CaF_2 sample B depicted in Figure 4-2 (b), pulses were focused using a Mitutoyo Plan Apo objective 20x, 0.42 NA, and a group of lines with various speed of writing and energy were inscribed and the result shows that for speeds exceeding $50 \mu\text{m/s}$ there is a strong indication of pearl-chain type of modification which makes it impossible to have low loss waveguiding [115], [116]. Thus, to avoid such high-loss scatterers in the waveguide structure and to have a maximum overlap between consecutive pulses, we chose a speed of $v = 10 \mu\text{m/s}$ in which the distance between two consecutive pulses will be $v/f = 0.04 \text{ nm}$ where f is the repetition rate of the laser source and the number of pulses overlapping within the beam diameter will be $N = 2\omega_0/h = 2.29 \mu\text{m}/0.04 \text{ nm} = 57,142$. With such a small beam shift, the beam translation along the modified track can be assumed to be continuous.

Consequently, as shown in Table 4-1, five 20- μm double track waveguides (WG-1, WG-2, WG-3, WG-4 and WG-5) were inscribed with five different energies per pulse from 0.41 μJ to 0.56 μJ approximately which covers the range between 25 % above the damage threshold (0.33 μJ) and slightly below the crack formation energy of 0.61 μJ .

As it is shown in Table 4-1 below, other descriptions are included to precise the following parameters of writing:

- **Speed of writing (v):** which is related to the energy delivered (E_D) at each point as a product of the single pulse energy and the number of pulses traversing a given point. This can be formulated as:

$$E_D = 2\omega_0 E_p f / v \quad (4.2)$$

Where E_p is the energy per pulse ; ω_0 is the diffraction limited beam waist; f is the repetition rate of the source; v is the speed of writing.

- **Focal volume of the beam:** It is described with the total energy delivered traversing the focal surface, fluence (F), or an energy density at the confocal volume (E_v) in which the shape of the filament is formed, in the athermal writing regime, resembles the beam shape as it was described in Section 2.1.2. This can be given in J/cm^2 and J/cm^3 , respectively, as:

$$F = \frac{E_p}{\pi\omega_0^2} \quad (4.3)$$

$$E_v = \frac{E_p}{2\pi\omega_0^2 Z_R} \quad (4.4)$$

Where E_p is the energy per pulse; ω_0 is the diffraction limited beam waist; Z_R is the Rayleigh length.

- **Pulse shape and pulse duration:** Assuming a temporal and spatial Gaussian profile for the pulse, these parameters can be implicated as irradiance at the focal point ($I[z=0]$) which can be given in TW/cm^2 as:

$$I[z = 0] = \frac{E_p \times 10^5}{\sqrt{\frac{\pi}{2}} \times \tau \times \frac{\pi \omega_0^2}{2}} \quad (4.5)$$

Where E_p is the energy per pulse (μJ); ω_0 is the diffraction limited beam waist (μm); τ is the temporal width of the pulse (fs).

Table 4-1 : DLW waveguide inscription parameters of CaF_2 waveguides. Crack th. – threshold of crack formation; Mod. th. – Modification Threshold; E_p (μJ) – Energy per pulse; E_D (mJ) – Total Energy Delivered at focal point; F (J/cm^2) – fluence; E_v (J/cm^3) – Total Energy Deposition per unit volume and I (TW/cm^2) – Irradiance.

Waveguide	Crack th.	WG-1	WG-2	WG-3	WG-4	WG-5	Mod. th.
E_p (μJ)	0.61	0.56	0.52	0.48	0.44	0.41	0.33
E_D (mJ)	35	32	30	27	25	23	19
F (J/cm^2)	14.87	13.65	12.67	11.70	10.72	9.99	8.04
E_v (J/cm^3)	10131	9300	8636	7972	7307	6809	5480
I (TW/cm^2)	139.5	128.1	119.0	109.8	100.7	93.8	75.5

Table 4-1 shows all the main writing parameters of each double track, which are separated by $200 \mu\text{m}$ with a single track at $0.52 \mu\text{J}$ of pulse energy (E_p) in the middle to be used as reference for characterization experiments.

Once the waveguides are inscribed, due to the combined effects of the conical shape of the focused beam and writing process which takes place at a certain depth, the DLW process didn't access the final few micrometers before the end facets as it is depicted in Figure 4-3 below.

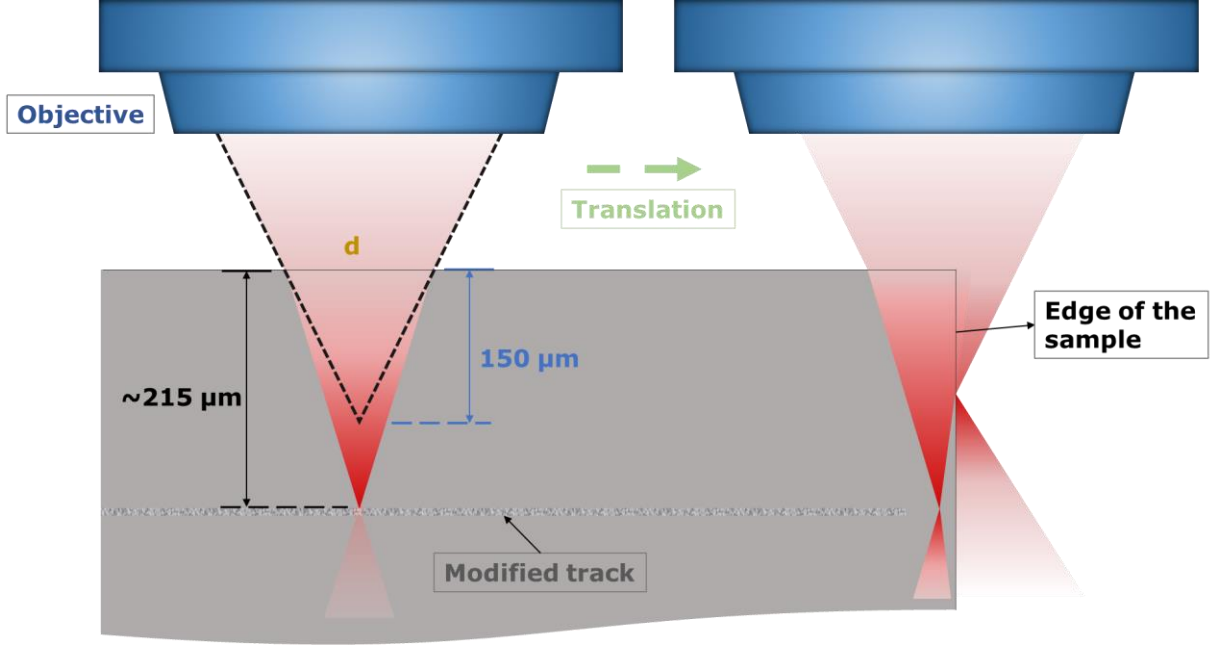


Figure 4-3 : Schematic diagram of a conical shaped beam focused at 150 μm mechanical depth below the sample. LEFT: Beam focused inside the sample; RIGHT: beam focused at the edge of the sample. d is the beam diameter at the surface of the sample.

As it is shown in Figure 4-3 above, the beam is focused using an objective at the mechanical depth of 150 μm which is equivalent to $150 \mu\text{m} * n \approx 215 \mu\text{m}$ where $n = 1.4305$ is the refractive index of the given CaF_2 sample. As the beam is translated to the right edge of the sample, a part of the beam is reflected by the edge. For example, for the diffraction limited beam in this case, the conical diameter, d , can be given as:

$$d = d_0 \sqrt{1 + (z/z_R)^2} \quad (4.6)$$

Where d_0 is the diffraction limited beam diameter at the focus; z is the mechanical depth; and z_R is the Rayleigh length. For example, for the objective with $\text{NA} = 0.42$ and a CaF_2 sample with the given mechanical depth of writing at 150 μm below the surface, d is calculated as 47

μm . Thus, in this particular case, the DLW process will not access the final few micrometers before the edge of the sample, and this zone should be removed with polishing.

Therefore, the sample's end facets are polished to optical quality and resulted in 11.06-mm long double track waveguides as it is shown in Figure 4-4.

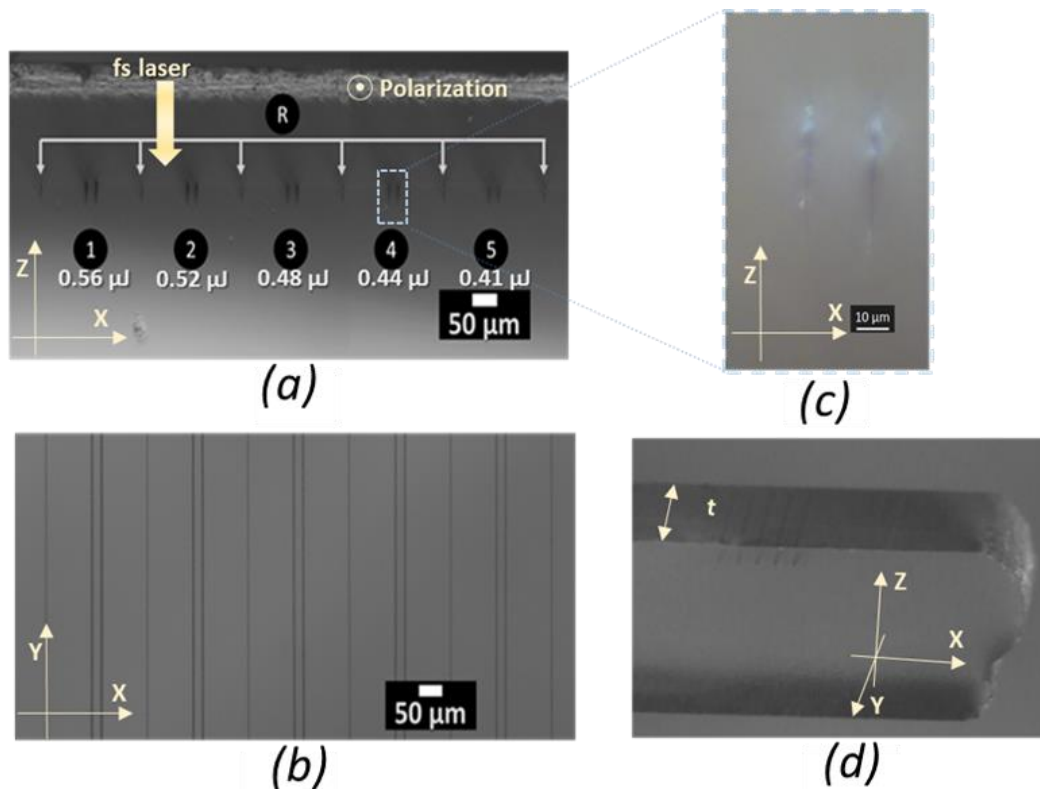


Figure 4-4 : Microscope images of all the five tracks written inside undoped CaF₂ crystal. (a) and (b) are side (xz) and top (xy) bright field (BF) images in transmission of written tracks with different energies, respectively. (R) - reference single track written to locate the double tracks. (c) shows dark field (DF) image in reflection of a dual track waveguide written with 0.44 μJ . (d) shows the 20X BF image of a transversally sliced part of the sample with thickness, t , of 1.37 mm.

Figure 4-4 shows the BF microscope images of five double track waveguides and six reference tracks written inside arbitrarily cut undoped CaF₂. The modification threshold identification showed a sharp transition from no modification to pearl-chain type of modification, while the sample with a defined cut along the cleavage and fundamental crystallographic axes showed a smooth modification window, which will be discussed in the upcoming section.

4.3 Smooth Modifications and Non-reciprocity of DLW inside CaF₂

Once we noticed the smooth modification inside the Sample A, Figure 4-2 (a), further tracks were inscribed to systematically study the relationship between the polarization of the writing beam, the writing direction, the pulse energy, the translation speed and the crystallographic axes. This is illustrated in Figure 4-5 below, the first two cases, Case 1 and 2, show that the polarization is kept parallel to the scanning direction while in the next two cases, Case 3 and 4 the polarization is kept perpendicular to the scanning direction.

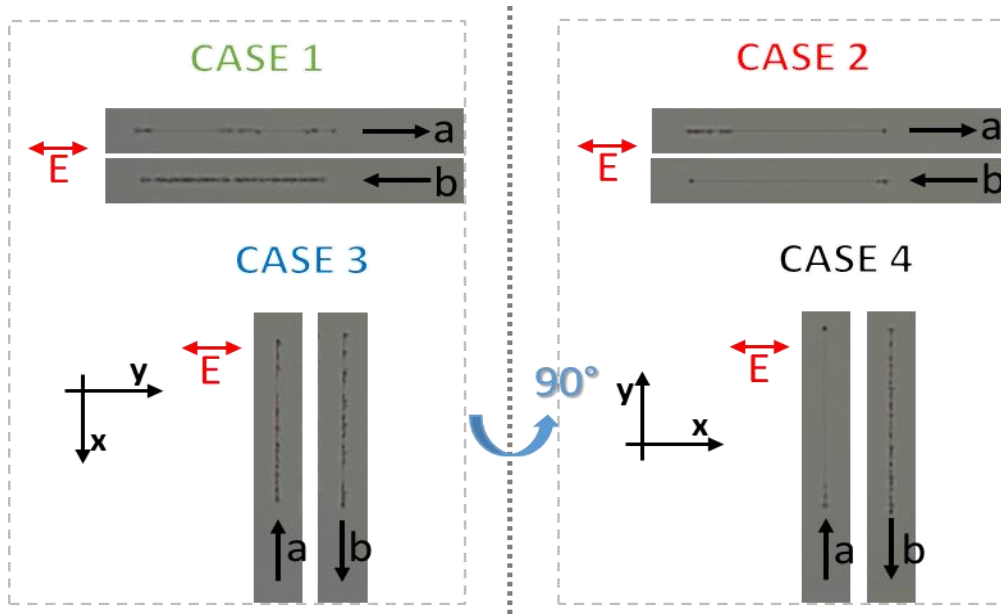


Figure 4-5 : Example of the inscribed tracks with a number of pulses of 2280 per spot and a fluence of 12 J/cm^2 . The polarization is along the y- and x-axis of Sample A in (Case 1, 3) and (Case 2,4), respectively. Furthermore, a and b indicate the scanning directions.

In addition to the polarization direction, the laser scanning direction was kept along the x- and y- axis in Case 2,3 and Case 1,4, respectively. Notice that the sample is rotated by 90° counterclockwise between the cases 1,3 with respect to cases 2,4. Once the tracks were inscribed, we used the image processing tool from Igor Pro software, from WaveMetrics, Inc.,

to calculate the fraction (percentage) of the track lines with smooth modification as shown in Figure 4-6.

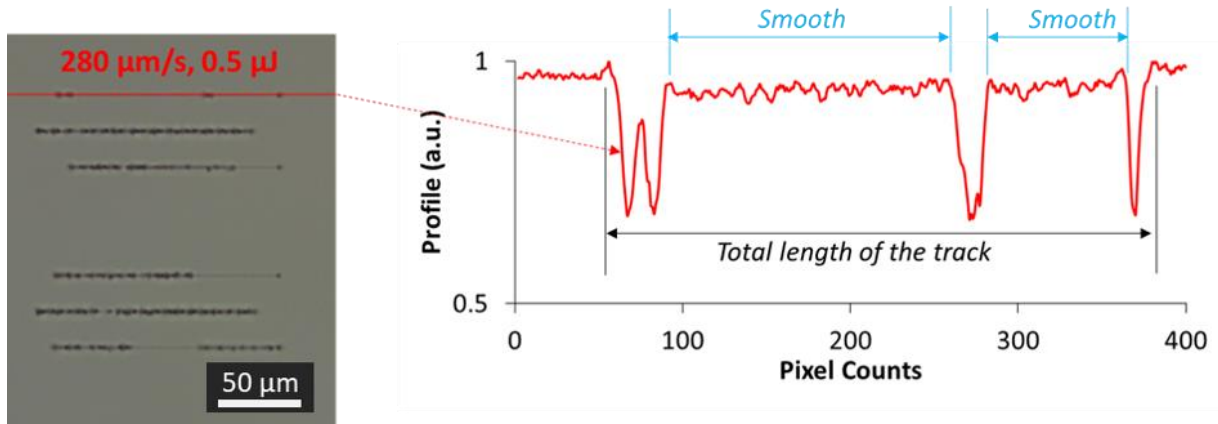


Figure 4-6 : The fraction of smooth modification for the track inscribed with $N \approx 2000$, and $F = 12 \text{ J/cm}^2$.

The percentage of smooth modification on each line is identified and we observed that despite the smooth modifications, the writings were also non-reciprocal with respect to the writing directions in most of the cases. All tracks with non-zero smooth track fractions are presented in the scatter plots of Figure 4-7 in below.

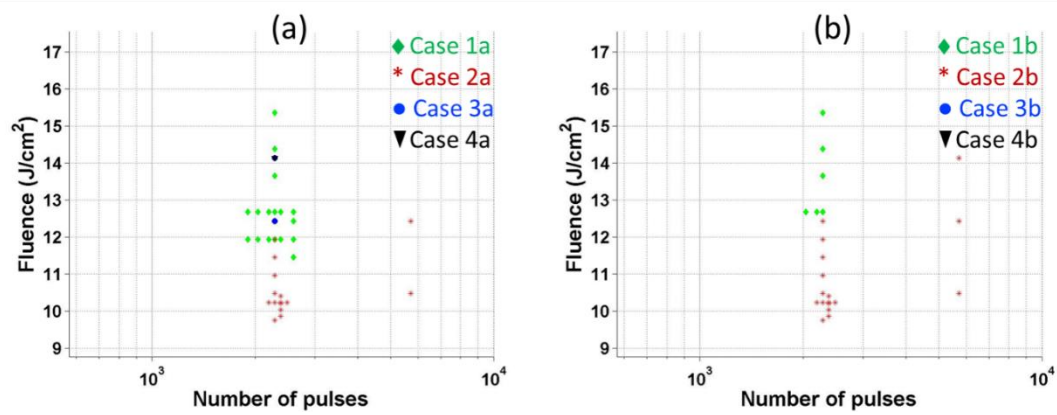


Figure 4-7 : All smoothly modified tracks with non-zero fractions as a function of number of pulses and fluence. (a) and (b) show the two directions of scanning in each axis.

In order to identify the smooth modification window and non-reciprocity of the material modification in relation to the laser scanning direction, we used linear interpolation and resampling to plot the contour between the writing energy, fluence, scanning speed, and number of pulses per spot.

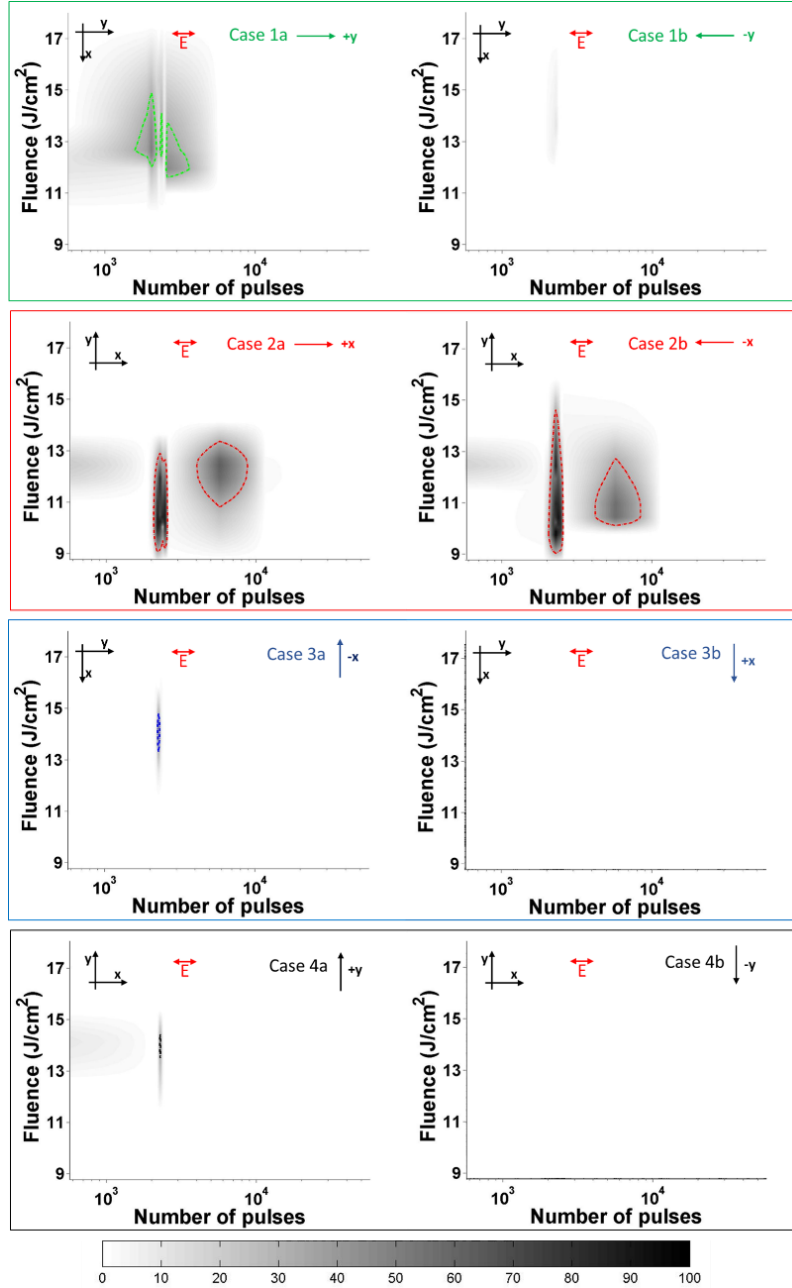


Figure 4-8 : Plot of all the smooth modifications inside CaF₂ and the contour, at 30% of the smooth modification ratio, shows windows for the writing parameters with respect to the direction of scanning, crystallographic axes, number of pulses per spot and fluence. The gray scale indicates the percentage of the track that is smoothly modified.

As it is shown Figure 4-8 once the percentage of smooth modification parts of the inscribed tracks with both non-zero, as it was shown in Figure 4-7, and zero values are identified, linear interpolation and resampling was performed on the data to identify and plot the windows of writing parameters for smooth modification. In these plots, it is obvious that the window of smooth modification is affected by the direction of scanning, or non-reciprocity, which will be discussed in the next section.

4.3.1 Smooth Modification

Despite a few crystals mentioned in Section 2.2, smooth or type I modification in crystals are not common due to the fact that a photoinduced increase of the refractive index through structural densification of the crystal is essentially complex and impractical. However, when overcoming this difficulty, type I modifications in crystals can result in very low transmission loss waveguides. For example, J. Bérubé et al. recently reported single mode operation at a wavelength of 2850 nm and propagation loss of < 0.37 dB/cm inside a depressed cladding waveguide of sapphire [120]. The low loss is mainly attributed to the fact that the authors were able to inscribe homogeneous and highly symmetrical tracks in a depressed cladding configuration instead of stress induced between several damage track waveguides that are susceptible to high scattering losses.

Similarly, within this thesis, we report for the first time, to the best of our knowledge such type I modifications inside cubic CaF_2 crystals. However, we found that this is the case only for one specially cut sample, Sample A in Figure 4-2 and only when specific quantitative and qualitative conditions of writing parameters are fulfilled as shown in Figure 4-8.

Given a 30 % smooth modification limit, i.e. 30 % of the tracks are smooth, we found a wide window of smooth modification for the cases 1a and 2 and in the case 3a and 4a, we observed a very narrow window while in cases 1b, 3b and 4b, there are little to none smooth modifications. In general, the smooth modifications occur for a number of pulses per spot

within the range of 2000 to 3000 which corresponds to a scanning speed of about 200 $\mu\text{m/s}$ to 300 $\mu\text{m/s}$. This range is narrow and is shown to be very critical. In addition, for the cases where smooth modification happened, the range of fluence values are between 12 J/cm^2 to 15 J/cm^2 except for the case 2, in which there is a wider window for such modification, that is in the fluence range between 9 J/cm^2 to 13 J/cm^2 .

Furthermore, we observed wider side windows for smooth modification in case 2a, i.e. for a writing polarization parallel to the +x-crystallographic axis for numbers of pulses from 4000 to 9000, speed between 60 $\mu\text{m/s}$ to 130 $\mu\text{m/s}$ while in the case 1a, i.e. for a writing polarization parallel to the +y-crystallographic axis, the side windows are closer and around the speed of 280 $\mu\text{m/s}$ ($N \approx 2000$) and 200 $\mu\text{m/s}$ ($N \approx 3000$).

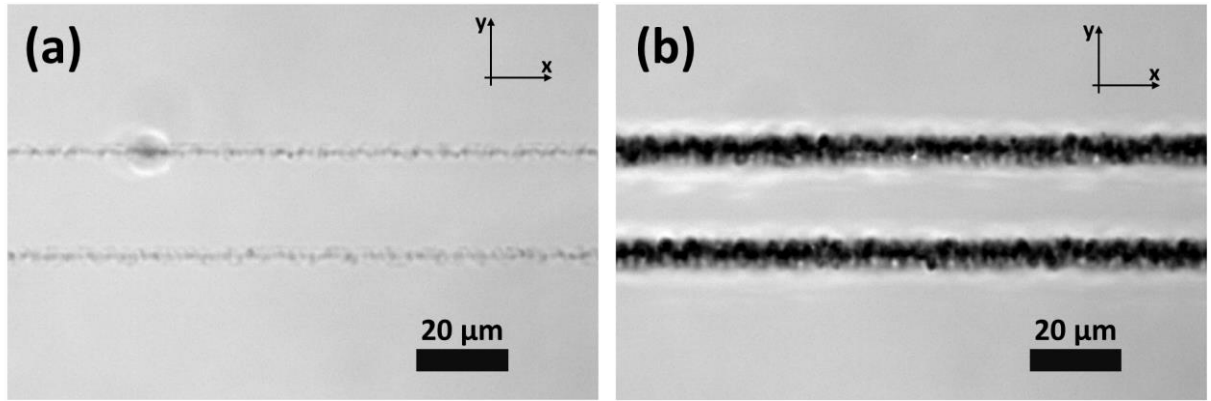


Figure 4-9 : Bright field microscopic image of double tracks. (a) shows section of a smoothly modified track inscribed with case 2 at 240 $\mu\text{m/s}$ ($N \approx 2400$) and energy of 0.47 μJ ($F = 11.4 \text{ J/cm}^2$); (b) shows part of modified track inscribed with case 2 at 10 $\mu\text{m/s}$ ($N \approx 57000$) and energy of 0.67 μJ ($F = 16.4 \text{ J/cm}^2$) with no smooth modification.

In addition, the writing cases where the polarization is perpendicular to the writing direction, cases 3 and 4, show little to no smooth modification. As the only difference between the cases 2 and 3 and also cases 1 and 4 is the change of the polarization direction with respect to the writing direction, we can conclude that the polarization plays the most significant role for the occurrence of smooth modification.

The refractive index change and waveguiding capability of the tracks with smooth modification are studied. The bright field (BF) microscope images of Figure 4-9 show a comparison of two

types of tracks. The tracks in (a) are inscribed inside the window of case 2, as in Figure 4-8, smooth modification with speed of $240 \mu\text{m/s}$ ($N \approx 2400$) and energy of $0.47 \mu\text{J}$ ($F = 11.4 \text{ J/cm}^2$) while in (b), the tracks are still inscribed according to case 2 but outside the smooth modification window with $10 \mu\text{m/s}$ ($N \approx 57000$) and energy of $0.67 \mu\text{J}$ ($F = 16.4 \text{ J/cm}^2$) with no smooth modification. As it can be observed, in the case of smooth modification, the modified zone is much thinner and it is within the confocal diameter $\sim 2 \mu\text{m}$ while in the other case there is a crack formation. Both modifications show pearl-chain type of modification.

Moreover, Figure 4-10 shows the top view of a two-dimensional refractive index change map of double tracks in the regime of strong smooth modification. The refractive index change is calculated based on the Optical Path Difference, OPD, measurement using the phase-contrast microscopy method, which will be discussed in Chapter 6, Section 6.2. Thus, the refractive index change is obtained by dividing the OPD measurement by the confocal parameter of writing, i.e. $2Z_R = 10.3 \mu\text{m}$, with a reasonable assumption that the smooth modification is localized within the confocal volume and which is also confirmed by the confocal microscope images of the side view of the tracks.

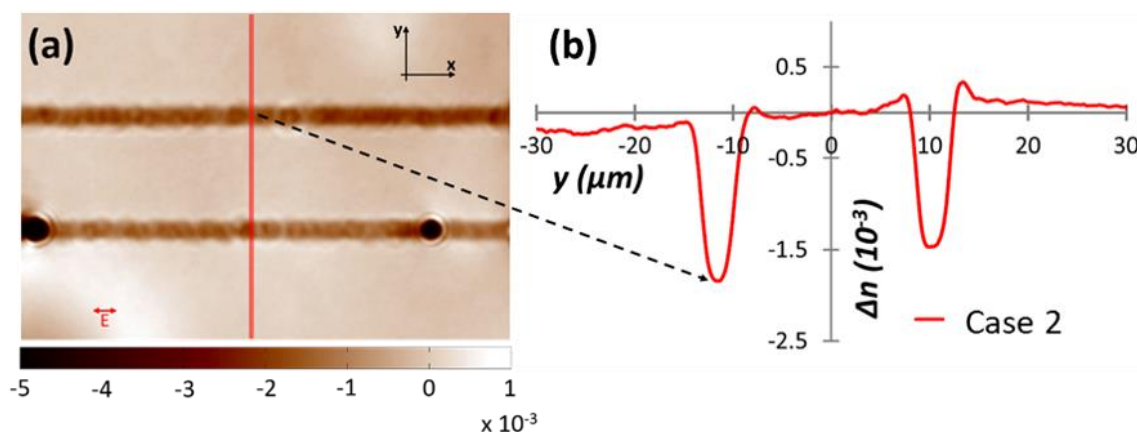


Figure 4-10 : Double track written at speed of $240 \mu\text{m/s}$ ($N \approx 2400$) and energy of $0.47 \mu\text{J}$ ($F = 11.4 \text{ J/cm}^2$) with case 2. (a) shows the two-dimensional refractive index change map of the portion of the double track as viewed from the top; (b) shows the line profile of the refractive index change map.

It can be observed that the refractive index change is negative along the tracks with the magnitude of 10^{-3} . Moreover, the refractive index change is localized along and in a very close vicinity of the track leading to no stress based waveguiding. Besides, the dark spots indicate non-smooth modification, which indicates that the window is so narrow for smooth modification and they exhibit high index modification which shows the possibility of stress based guiding.

In general, for this particular cut of the CaF₂ crystal and defined crystal axis, case 2 shows a wide and strong smooth modification window in both directions of scanning and we highly suggest it can be used to inscribe type I modification based depressed cladding waveguides with low loss.

4.3.2 Non-reciprocity

Until recently, it was well recognized that reversing the writing direction should not have the effect on material processing and associated modifications. However, subsequent studies inside silica by Kazansky et al. [21] in 2007 showed that there is a remarkable phenomenon in direct laser writing is usually known as non-reciprocity and it is manifested as a change in material modification by reversing the direction of writing. In addition, the study by other groups also confirmed such a phenomenon [121],[122]. This is usually termed as a quill effect as the effect resembles to a quill pen and is interpreted in terms of anisotropic trapping of the electron plasma by a tilted front of the ultrashort laser pulse as F. He et al. [121] suggest, indicating that further studies are needed on both spatial and temporal tilt effects .

In addition to the above studies inside fused silica, non-reciprocal photosensitivity was demonstrated inside a LiNbO₃ crystal under uniform and symmetrical laser radiation with an interpretation based on the effect of light pressure and associated heat flow [123]. As far as the source of anisotropy is considered, this was a new non-reciprocal, nonlinear optical

phenomenon with the source of the anisotropy being the non-centrosymmetric nature of LiNbO_3 crystals.

The mechanism was explained by asymmetry in average heat current along the writing direction which is related to the material asymmetry described by the heat current with a sixth rank tensor. Consequently, the change in temperature between the opposite sides of the beam is governed by the directional heat current which results in a difference in the temperature increase due to the anisotropic heating in one direction and isotropic heating in another as shown Figure 4-11 [123].

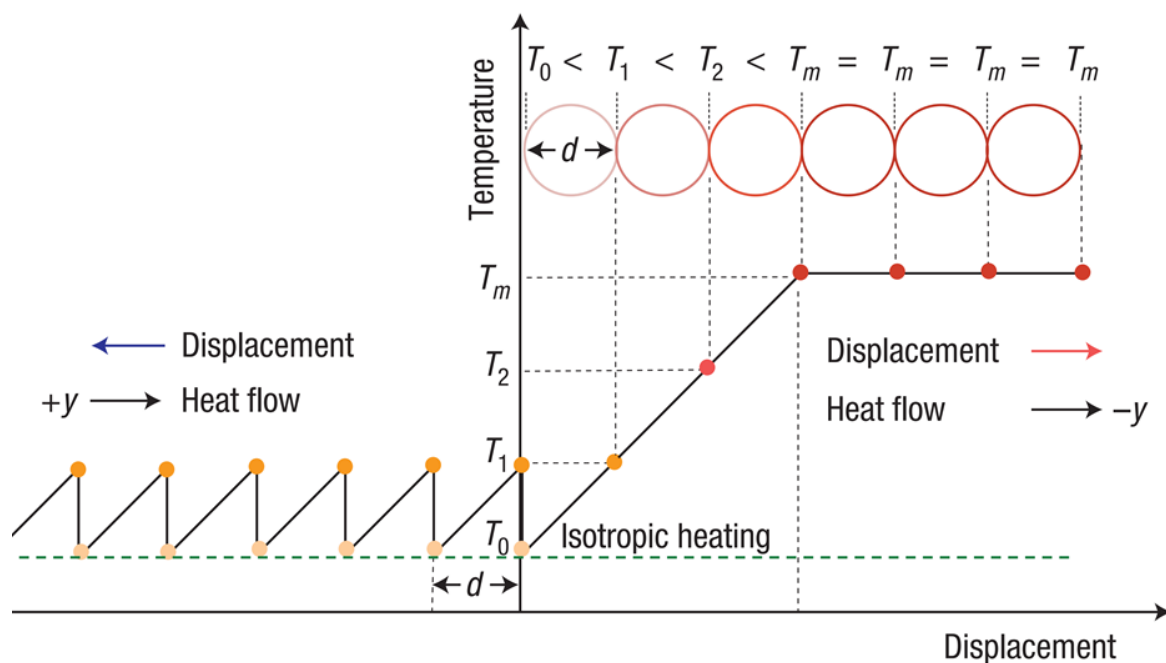
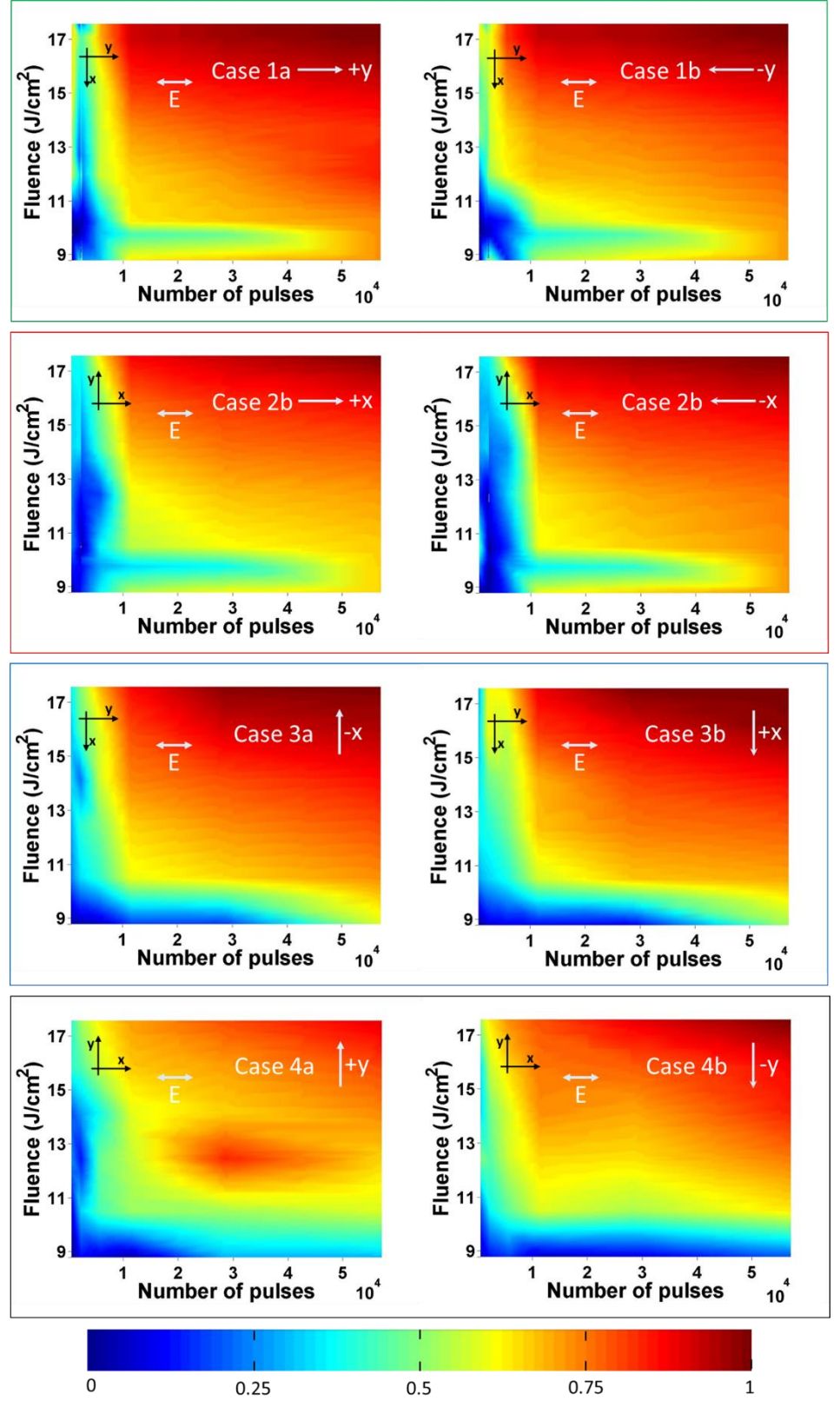


Figure 4-11 : Illustration of the differential heating of a crystal as a result of the bulk photothermal effect (copied from [123]).

As it is shown in Figure 4-11 above, heat flows (black arrow) in the -y direction of the crystal. The temperature of the crystal increases until saturation when the beam is displaced in the direction of heat flow (red arrow) and oscillates near the level defined by isotropic heating (green dashed line) when the displacement is opposite to the heat flow (blue arrow). The large circles illustrate the laser beam, and increasingly darker color corresponds to increasing temperature of the sample at the beam position.

Figure 4-12 : Non-reciprocity of writing based on the pixel counts of the written tracks. In the color scale, 0 and 1 show no or smooth modification and the maximum modification in each case, respectively.



Similarly, as it can be observed in Figure 4-8, it is clear that the smooth modification windows are not symmetrical for reversed directions of scanning, i.e. for a- and b-directions. In addition,

as it is shown in the cases 1 & 4 compared to cases 2 & 3, non-reciprocity in the smooth modification regime is particularly stronger for the writing direction along the y-axis of the crystal. This is further considered and studied for the regimes of modification other than smooth modification as can be shown in Figure 4-12 above.

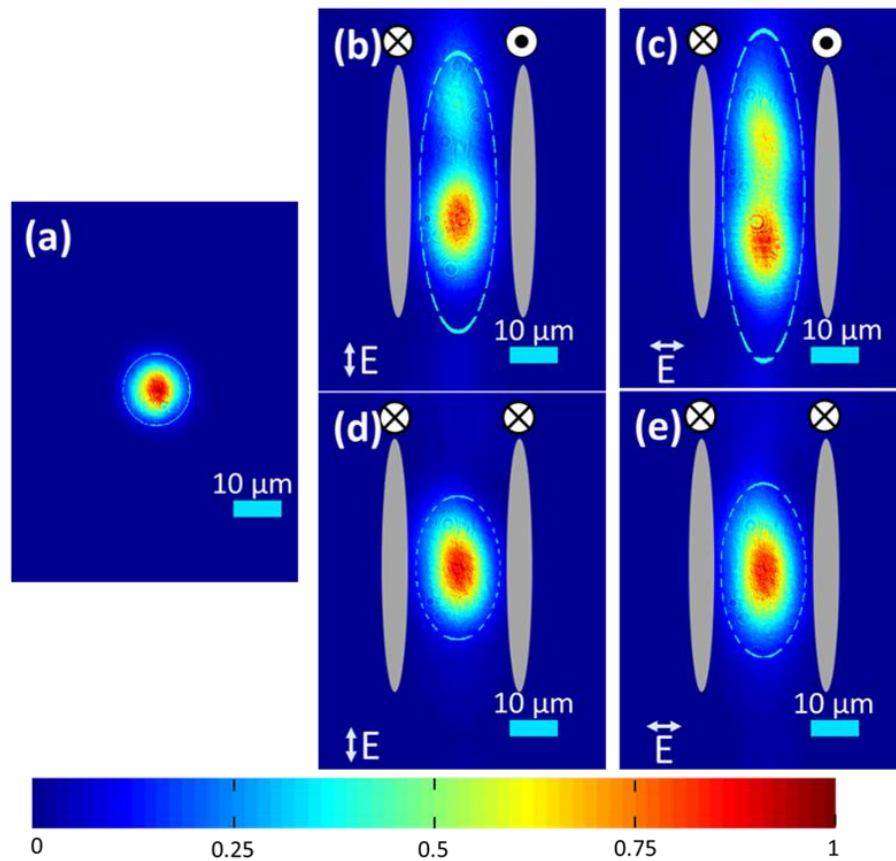


Figure 4-13 : Near field profile images of light guided inside double track waveguides inside CaF_2 crystal with writing directions shown above the sketch of the tracks with circle and x and circle and dot for the inward and outward directions of writing, respectively. (a) HeNe source at 633 nm; (b) and (c) are tracks written by opposite directions of writing with polarizations parallel and perpendicular to the elongation of the tracks, respectively; (d) and (e) are tracks written by same directions of writing with polarizations parallel and perpendicular to the elongation of the tracks, respectively.

Different writing regimes as shown in Figure 4-12 above are plotted by considering the pixel counts of the short tracks for the range of thresholds as described in Figure 4-6 and normalization based to the maximum pixel count of each case. This is followed by simple linear interpolation to cover all the ranges in each writing regime. The blue color shows the regions

where there are no modifications or smooth modification while the dark red regions show the regime of writing with the possibility of crack formation. Cases 3 & 4 show a continuous threshold around regions below 10 J/cm² and writing speed above 50 $\mu\text{m/s}$, $N \approx 10000$, which makes sense as we have observed little to none smooth modification. On the other hand, cases 1 & 2 show a discontinuity in the region between $N \approx 2000$ to 3000 in which the smooth modifications occur.

In addition to the discontinuities in the regions which are related to the occurrence of smooth modifications, plots of the a- and b- directions of writing for cases 1 & 4 are less symmetrical as compared to cases 2 & 3. Therefore, the non-reciprocity is particularly stronger along the y-crystallographic axis of the sample.

Furthermore, an additional study on the effect of non-reciprocity of the waveguiding characteristics is performed. Figure 4-13 shows double track waveguides written along the x-crystallographic axis with 24 μm between them at a fluence of 16.8 J/cm². The polarization is kept parallel to the writing direction as in case 2. As it can be observed, the waveguiding characteristic significantly changes for different directions of writing with respect to the crystallographic axis. The waveguiding setup used for this case is discussed in detail in the following chapter, Section 5.3.1

With all the aforementioned proofs, we can be certain that non-reciprocity exists in CaF₂ crystals. However, the CaF₂ crystal, with space group $Fm\bar{3}m$, is centrosymmetric. Thus, the non-reciprocity of the material modifications cannot easily be attributed to the asymmetry of heat current due to a non-centrosymmetric nature of the crystal which is reflected on the anisotropy of temperature gradients as in the case for LiNbO₃. However, at very high temperatures, CaF₂ crystals show a crystal-orientation dependency of thermal effects such as birefringence [91], depolarization and astigmatism [124][125]. Given the fact that such anisotropy inside CaF₂ is reported for the first time, to the best of our knowledge, we recommend a careful development of a more sophisticated setup and “real time” laser matter interaction study at very high temperatures.

4.4 Conclusion

In conclusion, although the main motivation behind the task described in this chapter was to inscribe double track CaF_2 waveguides with various writing parameters, we have observed non-reciprocal and smooth modification for the samples cut along the principal crystallographic axes. The method for both experimental and analytical approach for identifying the window for modifications inside these samples has been discussed. Strong smooth modifications were observed when the writing direction is parallel to the polarization direction in general, and wider windows are obtained along the x-crystallographic axis in particular. In comparison, strong non-reciprocal writing was observed along the y-crystallographic axis.

5 Guiding Characteristics of the Waveguides

In the previous chapter, the inscription of low speed double track CaF_2 at different pulse energies has been presented. In this chapter, the theory and experimental demonstration will be described to study the waveguiding mechanism and transmission loss of the guided modes inside femtosecond laser induced double track waveguides of CaF_2 . The first part of the chapter covers an overview about waveguiding followed by different geometries of waveguides inside crystalline materials in Sections 5.1 and 5.2, respectively. In Section 5.3, the theory and setup for characterizing waveguide modes is discussed and the near-field mode profiles of the double track CaF_2 waveguides is presented. Furthermore, Section 5.4 discusses a simple transmission loss measurement setup with theoretical modeling, the power measurement of the guided modes and a comparison of the results with previous measurements of other groups is presented. Finally, Section 5.5 presents the polarization dependence of the waveguides.

5.1 Introduction to Waveguiding

Free space beam propagation of light takes different forms of waves which can be described as solutions of the Helmholtz equation. Due to practical reasons and its ease of study, a special solution class of beams taking the form of Gaussian waves are commonly considered in which the given beam parabolically expands from the minimum beam waist point, usually designated as z_0 , as it propagates [126]. Thus, optical beams diffract and broaden from a point source to the destination point. Then, in order to transmit light between two points in free space, it is necessary to make use of common and conventional optical components like mirrors, lenses, prisms [127].

Due to the fact that photons have many degrees of freedom and exhibit different properties as compared to electrons, there is an ever expanding industrial use of optical signals as a means of secure communication and material processing in fabrication of miniaturized optical and optoelectronic devices and functionalities. This becomes a driving force behind the technology towards confining and directing light to complex geometrical locations by using dielectric materials as pipes, also known as guided-wave optics. By implementing spatially inhomogeneous refractive indices, waveguiding technology provides a new venue of complexity and flexibility into long-distance low-loss light transmission [127]. Light can be confined and guided using optical waveguides which are commonly formed by a medium of higher refractive index surrounded by another medium with lower refractive index, resulting in self-consistency and confinement of the optical beam along the propagation direction by multiple total internal reflections.

The most widely used application of waveguides can in general be classified as optical fiber waveguides for communication and waveguides for integrated optics which mimic systems on-a-chip in electronic systems. Due to its extremely attractive features, during its invention and while advancement of the technology, optical fibers are the most widely applied waveguides to date [128]. However, due to the complex nature of drawing a preform, it is challenging to miniaturize complex optical circuits with fibers.

For applications related to integrated optics technologies, due to well established and mature approaches of system on-a-chip technology, the trend was to adapt these 2D manufacturing approaches. To mention just a few of these methods: epitaxy or with polishing methods for planar waveguides or lithographic methods in combination with epitaxy or ion exchange for channel waveguides and so on. However, due to vast properties like wavelength, polarization, spatial mode and orbital angular momentum of photons which reflect the three-dimensional character of light, many features cannot be fully exploited with planar circuits. Waveguides fabricated using laser-induced breakdown inside dielectric materials have proven to be interesting solutions and the main drivers behind growing interest in 3D photonic solutions [42], [129], [130].

5.2 Geometries of Waveguides in crystals

Thanks to the capability of DLW for volume processing inside transparent materials, we can induce different groups of refractive index geometries inside dielectric materials [131]. Given the 3D flexibility and complexity of inscription, the processed photonic crystals can be categorized into many classes. Therefore, it is necessary to come up with a more simplified methodology to group and study the different geometries of waveguides inside crystals. One of these common methodologies is based on localized material modifications in relation to the optical damage threshold, the point where any modification is observed, of the substrate. For low intensity near or below the damage threshold, a smooth modification of refractive index, usually related to positive change inside the laser modified tracks, is induced. This is commonly referred to as Type I modifications. In crystals, these types of modifications are usually thermally unstable and are realized with only a handful of materials such as Lithium Niobate.

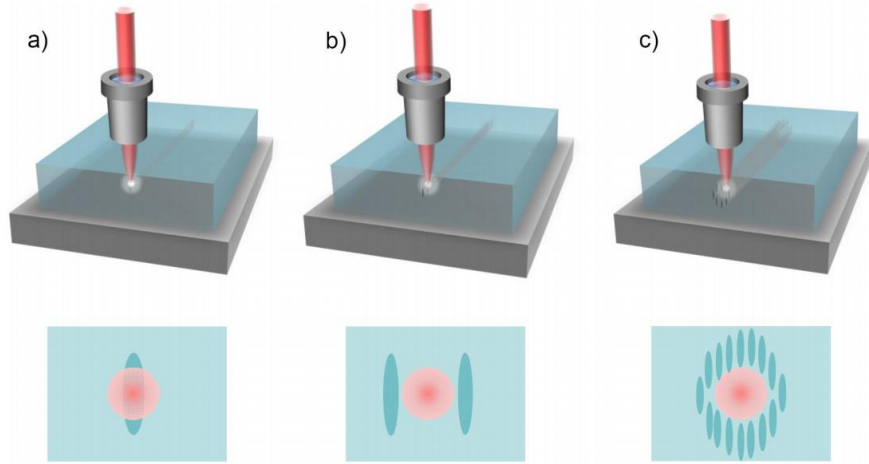


Figure 5-1 : Schematic plots of the fabrication of the three categories of guiding inside crystal materials by femtosecond laser irradiation and the spatial locations of the waveguide modes: a) waveguides based on Type I modification in single-line geometry, b) waveguides based on Type II modification in dual-line geometry, and c) waveguides based on Type II modification in depressed cladding Type III geometry. [132]

The second and third types of waveguide geometries, Figure 5-1 b&c, in crystals are related to high intensity irradiation, where localized severe damage of the crystal lattice occurs along the tracks with micro-explosions and empty void mechanisms. These damage regimes are usually

related with a degradation of bulk features and negative refractive index change inside the tracks.

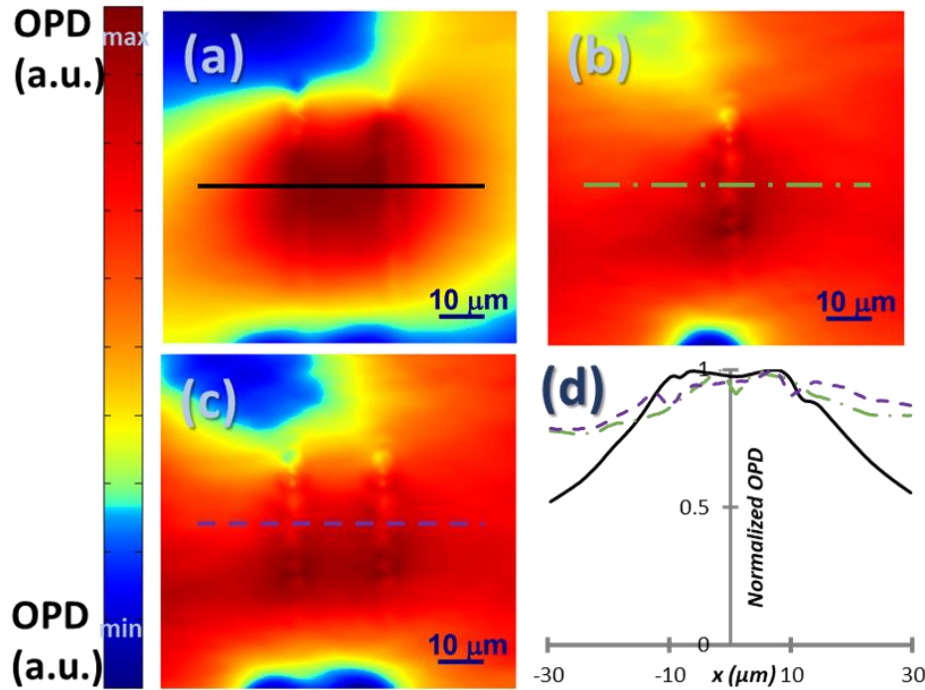


Figure 5-2 : (a) OPD measurement of double track waveguide, (b) OPD measurement of single track, (c) simple arithmetic addition of two single track OPD measurements and (d) line profiles of the OPD spatial maps of double track (Solid black line), single track (broken green line and a point) and generated double track (broken violet line).

In Type II waveguides, the negative refractive index along the tracks induces a stress-field in the vicinity of the tracks and produces a guiding core. We use double tracks with distances between them of typically 20 μm to 30 μm. Thus, the overall guiding structure will be the cumulative effect of the two tracks. Double track waveguides inside cubic crystals have already been inscribed and studied intensively with YAG. By far, inside CaF₂, double track waveguides have not been reported and hereby we will characterize the five double track waveguides inscribed with different energy and with 20 μm between them. While in Type III waveguides a number of single tracks encircle the core geometry. The guiding is more similar to a fiber clad-core configuration. Both Type II and Type III have excellent thermal stability. Type II waveguides are restricted to small sized cores, usually between 20 μm and 30 μm, they are widely applicable for single-mode, or low-order modes, while Type III modifications are more

convenient for highly efficient coupling and flexible 3D structures. Because of the refractive index change mechanism, both modification regimes can easily be achieved in crystals.

Figure 5-2 shows that the overall spatial map of OPD, or logically refractive index change, and, therefore, the guiding action is the linear cumulative effect of the single tracks

Refraction of light at a dielectric interface is governed by Snell's Law, which can be described as:

$$n_1 \sin \theta_1 = n_2 \sin \theta_2 \quad (5.1)$$

For the light propagating from medium 1 to medium 2. Where n_1 is the refractive ind, which is different from a simple addition of two single tracks.

5.3 Modes in Waveguides

ex of medium 1 and medium 2, respectively. As shown in Figure 5-3, when light strikes a medium 1 with lower refractive index at an angle θ_1 , it bends away from the normal to an angle of θ_2 . As the striking angle increases, the refracted angle will make 90° to the normal, i.e. it will be parallel to the interface. This angle is named the critical angle and is given by:

$$\theta_{cr} = \sin^{-1}(n_2/n_1) \quad (5.2)$$

Light with incident angles, θ , greater than the critical angle, $\theta > \theta_{cr}$ will be totally reflected. Total internal reflection, as shown in Figure 5-3, is a necessary condition for the beam to be confined and guided inside waveguides. Thus evidently, the waveguide is formed by a medium which is embedded by another medium of lower refractive index. The medium of higher refractive index, also known as the core, acts as a “trap” by confining light in the waveguide by multiple total internal reflections. In this way, light can be self-consistent and transported from one location to another location [127], [129].

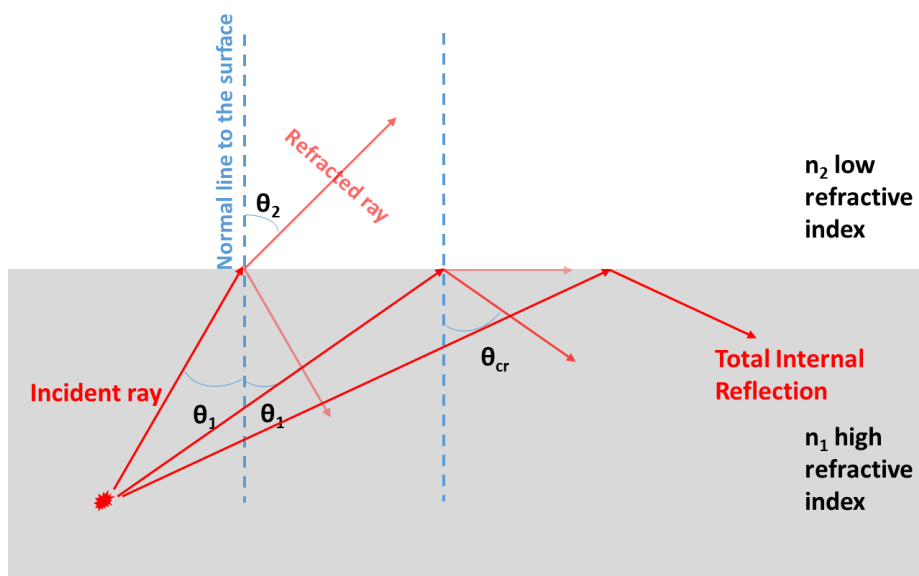


Figure 5-3 : Refraction and reflection of light at a dielectric interface. The proportion between reflected and refracted beam power can be calculated using Fresnel equations.

For example, considering a simple case of planar dielectric waveguide, in order to be self-consistent for the beam, it should reproduce itself between two reflections, i.e. the phase difference between two consecutive reflections should be an integer multiple of 2π . This can be described as:

$$\frac{2\pi n}{\lambda} 2d \sin \theta - 2\theta_r = 2\pi q \quad q = 0,1,2,\dots \quad (5.3)$$

Where d is the thickness of the core material; n is the refractive index of the core; λ is the free space wavelength of the propagating light; θ_r is the phase shift at the dielectric interface introduced at each reflection.

Given the condition for total internal reflection, we have only two plane waves allowed for each incident angle. Fields that satisfy these conditions are called eigenmodes or simply modes of the waveguide. Light can be transmitted through the waveguide by one or multiple modes depending on the source of excitation. However, the maximum number of the waveguide modes allowed can be described as Eigen solution. For common waveguides, the number of modes depends on the polarization and the wavelength of the source, the dimensions and

geometry of the core and the relative values of refractive indices of core and cladding. For example, Equation (5.4) shows the formulation of the number of TE modes, m , of planar dielectric waveguides; the symbol \doteq denotes the approximation done by increasing to the nearest integer.

$$m \doteq 2 \frac{d}{\lambda} \sqrt{(n_{core}^2 - n_{cladding}^2)} \quad (5.4)$$

Since light propagates in a waveguide in the form of modes, the cumulative field distribution will be the superposition of all existing modes. However, the relative amplitude of each mode highly depends on the mode matching with the profile of the source used to excite the waveguide.

5.3.1 Setup

In order to excite a given mode, the transverse distribution and polarization of the incident light should match that of the desired mode. Incident light can be coupled to a waveguide by directly focusing it into one of the end facets where the waveguide is exposed. However, due to the small dimension of waveguides, focusing and alignment are usually difficult. As a result, in order to have higher coupling efficiencies, the guiding setups should be developed in such a way that they are easier to manipulate and mechanically flexible down to micrometer levels.

Figure 5-4 shows the waveguide setup used for imaging the near field profiles and measuring the output powers for the purpose of observing the excited modes and also measuring the transmission losses of the waveguides. The source is a linearly polarized HeNe laser with circular Gaussian mode and measured M-squared (M^2) value of 1.07. The first half-wave plate, $\lambda/2_1$, in combination with a polarization beam splitter, PBS, adaptably controls the injected power with p-polarized light just after the PBS. The residual s-polarized light is blocked at beam blocker, BB1. While the second half-wave plate, $\lambda/2_2$, is used to control the polarization of the injected beam into the waveguides. Because of the observed weakly guiding of light by the waveguides, a low numerical aperture (NA) 5x objective, OBJ 1, with NA = 0.13 is used

to get an optimum beam waist and better NA matching between the injected and guided modes. The three-dimensional translation stage with linear x , y and z translations in combination with the rotary translations (θ , ϕ) are used to cover all points at a micrometer level. These fundamental Cartesian plane translations and rotary translations can be theoretically summarized in to polar angle, θ , azimuth angle, ϕ and radial distance, r in spherical coordinates.

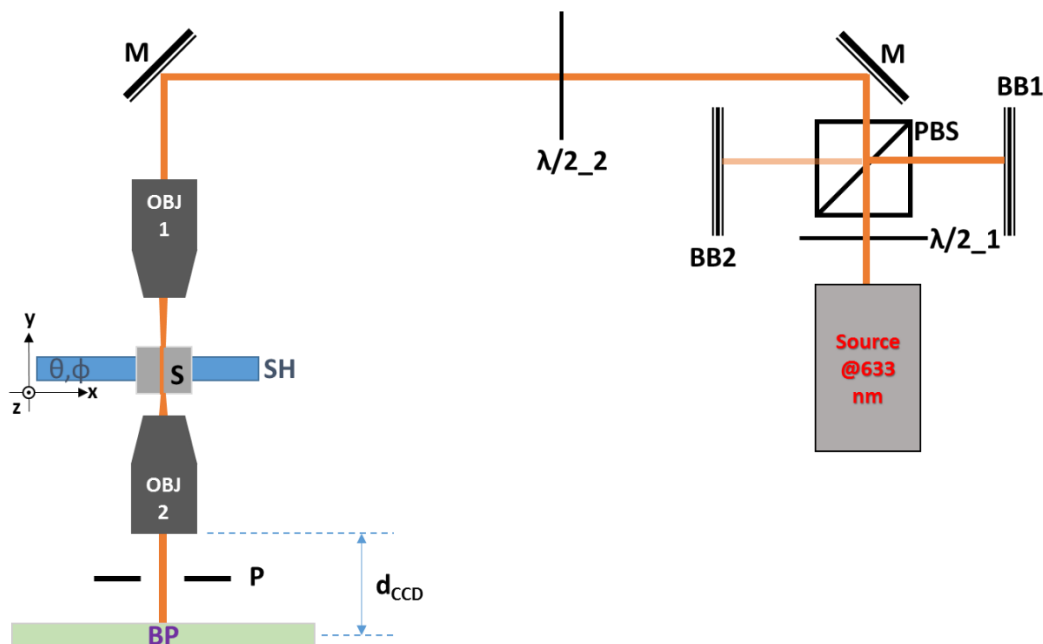


Figure 5-4 : Waveguiding setup. The source @ 633 nm is a HeNe Laser; $\lambda/2_1$ and $\lambda/2_2$ are half-wave plates; BB1 and BB2 are beam blockers/screens; PBS is a polarization beam splitter; M is a mirror at 45°; OBJ 1 is an Olympus Neo SPlan 5x injecting/focusing objective with NA = 0.13; S is the sample; SH is the sample holder with x - y - z 3D linear translations in addition to rotary translations with polar angle θ and azimuthal angle ϕ ; OBJ 2 is an Olympus UPlanFLN 20x imaging with NA = 0.5; P is a pinhole; BP is a Thorlabs BC106N-VIS Charge-Coupled Device (CCD) Beam Profiler.

Given the above explanation of the setup, in order to have optimized injection, we have two criteria. Firstly, we need to make sure that the beam is focused at the surface of the input facet of the waveguide sample, S, i.e. at the top side of the rectangular sample in the figure. This can be achieved by 3D translating of the sample until focused back reflection of the beam at the BB2, beam blocker/screen, is found. Secondly, we need to make sure that the beam strikes the surface parallel to the surface normal. Assuming the polished surfaces are perfectly perpendicular to the waveguides, this insures that coupling of the injected beam into the waveguide is not affected by conical tilt of the beam, which can result in injection induced NA mismatch. This is achieved by repeatedly optimizing the rotary translation adjustment keys and

then micro translations in the y -axis to observe whether the beam is symmetrically focused and defocused on BB2.

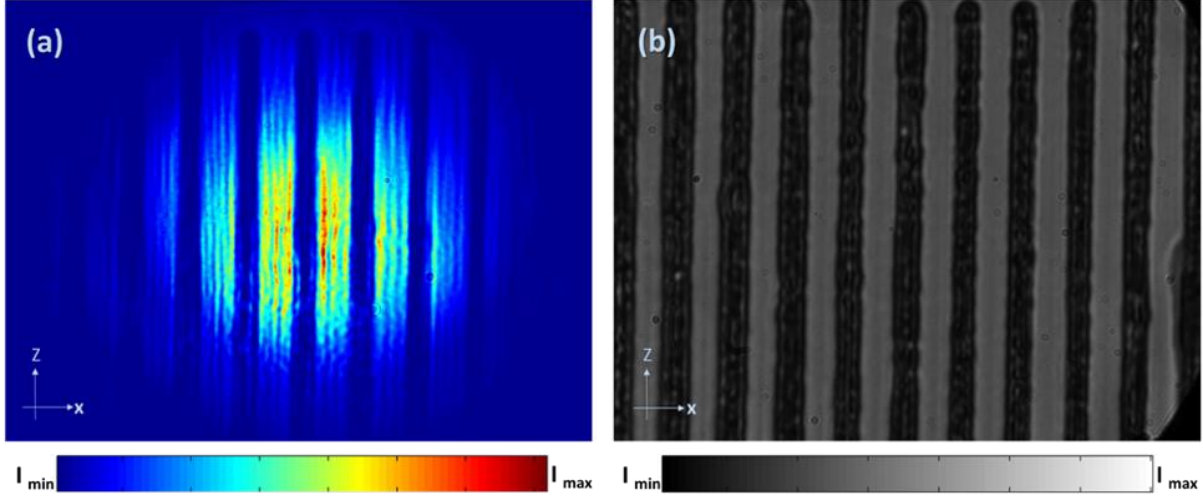


Figure 5-5 : Intensity images/ profiles of a micro-scale ruler on the CCD camera position. (a) shows the HeNe laser at 633 nm as a source while (b) shows illumination with white light. I_{min} and I_{max} are the normalized intensity values at the maximum and minimum radiation intensity; the dark marks are the marks of the micro-scale ruler with $10\ \mu\text{m}$ between them.

Once the optimized injection condition is achieved, we scan the input facet of the sample, i.e. xz -plane translation to find waveguides for both parallel (p) and perpendicular (s) polarizations of the incoming beam with respect to the setup table. When the guided modes, or waveguides, are located, the near-field profile of the ejecting facet of the sample is sharply imaged on the CCD. Theoretically, we will have maximum power yield from the waveguides, when the centroid of the excited mode, or fundamental mode, and the coupled beam perfectly coincide, thus by using micro translations in the xz -plane, we continue to optimize until maximum power is obtained at the CCD camera/ powermeter sensors. Once the power is optimized for a given waveguide, under the condition that the written waveguides are parallel to each other, we overlap the center of the pinhole, P, and the centroid of the profile to make sure that we have the same coupling conditions for all the remaining waveguides.

Since the CCD beam profiler is placed at a certain distance, d_{CCD} , after imaging with a 20x objective, with $\text{NA} = 0.5$, we need to calculate the magnification of the images being formed at this particular position. This is done by imaging a micro-ruler slide, positioned at the sample position, with scales of $10\ \mu\text{m}$ as shown in Figure 5-5 above.

Once the intensity patterns of the scales of the micro ruler are sharply focused on the CCD profiler, the data is exported as intensity values of each pixel over the whole area of 1024 pixels (in z) by 1360 pixels (in x). Since we know that each pixel has a size of $6.45 \mu\text{m} \times 6.45 \mu\text{m}$, we can calculate the magnification of the imaging part of the guiding setup as long as we know the average distance between the scales in pixels.

Considering the case of the HeNe laser, to calculate the average distance between the scales of the micro rulers, we first calculate the vertical binning (sum) of the intensity values since the scales are along the horizontal axis. We can observe in Figure 5-6 (a) that this results in intensity data points with numerous localized peaks.

Thus, we smooth the data points using 2nd degree polynomial local regression with weighted linear least square ('loess') technique by MATLAB. This will give us localized single maxima points. However, to avoid errors due to background intensity and smoothing of the data for lower intensity values, only values above 35 % are considered.

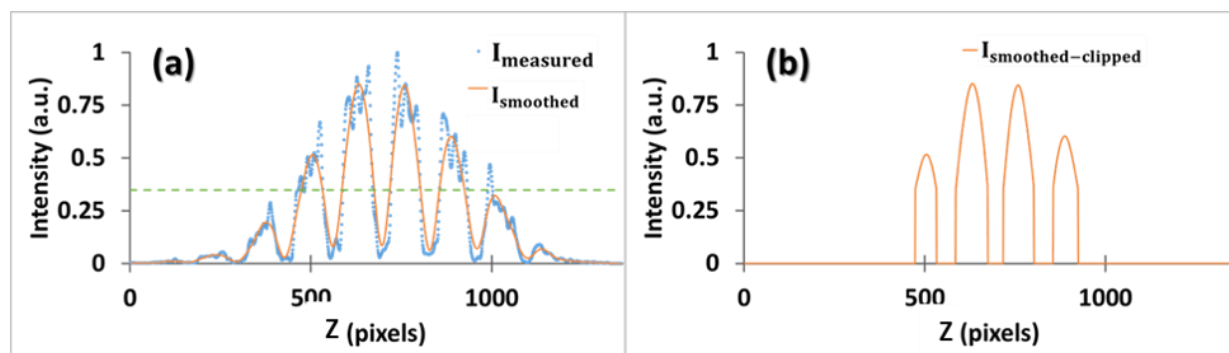


Figure 5-6 : Normalized intensity of measured and smoothed data points for determination of pixel distances between the scales of the micro ruler. (a) blue markers show measured data intensity vertically binned, continuous red lines represent the smoothed data and green discrete line at 35 % of maximum; (b) smoothed data trimmed at 35 % to avoid errors due to background and smoothing.

This results in 128 ± 1 pixels between each scale of $10 \mu\text{m}$. Therefore, considering the pixel size, the magnification of the imaging system is determined to be 82.56.

5.3.2 Mode Field Diameter Measurements

Figure 5-7 shows the measured power density distributions, PDDs, of five CaF₂ waveguides written with different pulse energies. As described in Section 4.2 of the previous chapter, these waveguides are designated as WG-1, WG-2, WG-3, WG-4, and WG-5 in descending order of the writing energy while the distance between the double tracks is kept constant at 20 μm . In addition, the HeNe laser source at 633 nm wavelength is simply designated as HeNe.

To calculate the mode field diameter (MFD) for the given circular Gaussian beam injected, the excited mode can intuitively be assumed as an elliptical Gaussian beam based on the PDD observed from the experiment. This assumption is further proved in the coming sections later in this chapter.

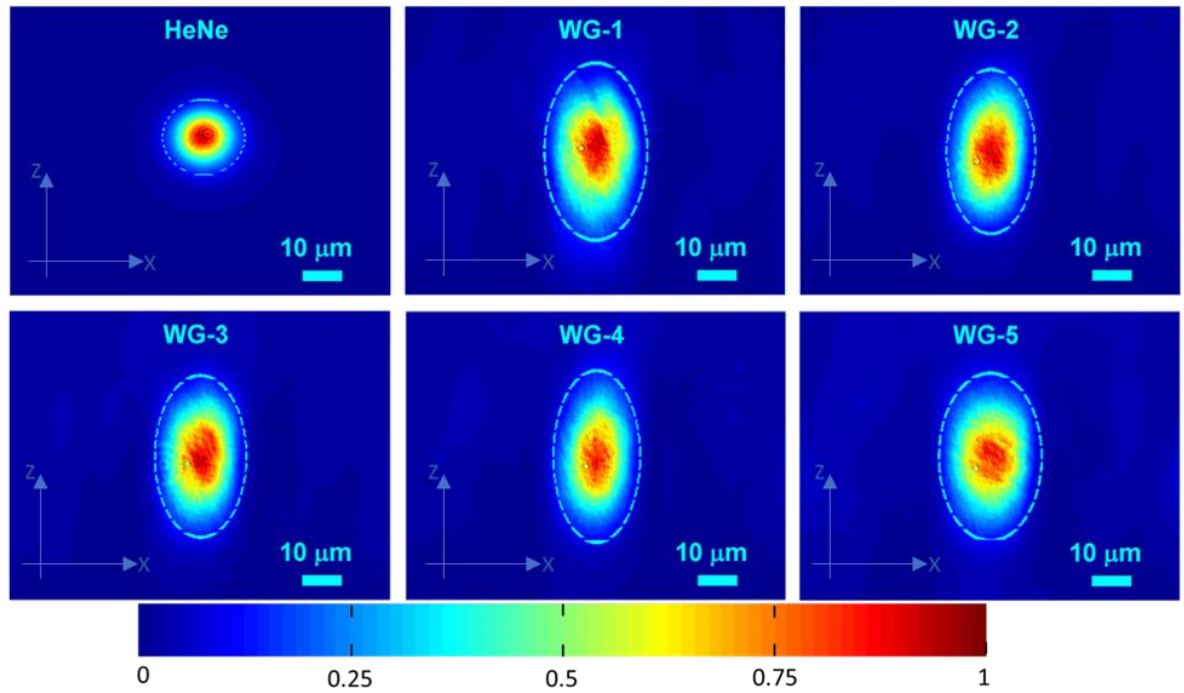


Figure 5-7 : PDDs of the injected HeNe laser source and the guided modes of five waveguides. Light blue broken lines show the boundary at $1/e^2$ of the maximum amplitude.

Given the assumed Gaussian distribution, the most accurate way of applying MFD calculation is by considering the boundary at the more generalized criterion in which the intensity drops to $1/e^2$ of the maximum intensity, this encircles about 95% of the power. This is also known as $D4\sigma$ method, as defined in ISO Standard 11146-1 in which the Gaussian beam MFD is in this case 4σ , i.e. $2\omega_i = 4\sigma$. In our case, instead of applying the discrete form of the above criterion, we used the non-linear least-square solver in MATLAB, *lsqcurvefit*, to fit the measured PDD according to the representation in Equation (5.5).

$$P(r, \theta) = \frac{2P_{tot}}{\pi\omega_x\omega_z} e^{-2r^2(\cos^2\theta/\omega_x^2 + \sin^2\theta/\omega_z^2)} \quad (5.5)$$

Where P is the power at coordinates r, θ ; P_{tot} is the total power of the Gaussian mode; ω_x, ω_z are the beam waists of the guided mode in the horizontal and vertical axes in the xz -plane; and r, θ are polar coordinates.

Figure 5-7 shows the 2D PDD of all the five waveguides and the source at the injection facet. As it can be observed from the images, the obtained profiles are highly elliptical for the injected circular source. The modes are simply constricted by the tracks. On the other hand, if we increase the distance between the tracks, we will change the overall 2D refractive index change distribution which doesn't necessarily result in gaussian fundamental modes. The fitting is indicated in the images by broken lines which are the $D4\sigma$ diameters.

Table 5-1 : Near-Field MFD of double-track waveguides inside CaF_2 and the HeNe source.

MFD	HeNe	WG-1	WG-2	WG-3	WG-4	WG-5
$X (\mu\text{m})$	14.78	18.16 ± 0.21	16.12 ± 0.27	16.42 ± 0.16	15.21 ± 0.37	18.31 ± 0.61
$Z (\mu\text{m})$	14.86	35.75 ± 1.95	32.50 ± 0.74	31.70 ± 0.14	34.37 ± 1.00	32.77 ± 0.76
Ellipticity	0.99	0.51	0.50	0.52	0.44	0.56

Table 5-1 shows the calculated horizontal, x – axis, and vertical, z -axis, 4σ – NF MFD of the source and the waveguides based on the above described modeling. As it can be observed from

the table, the ellipticity of the guided modes is below 0.6 for an almost perfectly circular beam injected at the entrance facet.

5.4 Transmission Losses

There are only a few techniques that can be applied for measuring propagation losses of waveguides. They are either techniques which require:

- **Z cut :** is also known as cut-back method where the transmitted power through waveguides of varying lengths is measured and absorption losses are calculated [133]. However, given the short length of the sample, it is difficult to apply this technique in our case.
- **Using a Fabry-Perot Cavity:** implements a Fabry-Perot Cavity to form complex interferometric setups. By artificially induced changes of the cavity length the transmission exhibits Fabry-Perot fringes which are directly related to the reflectivity of the end mirrors and the propagation loss of the waveguides. This method is commonly applied in fibers and it is not practical to apply it on crystals [134].
- **Scattered power method:** is the method which scans peak intensity variations along the propagation direction using a high-resolution camera. However, the method has some drawbacks. For example, when the scattering centers are not homogeneously distributed making it impossible to derive the residual intensity, $I(z) = I(0)\exp(-\alpha z)$. In addition, the portion of light that is not coupled in to the waveguide is detected as part of the scattered light [135].

Thus, we engage a technique which implements simple power measurements with directly obtained or calculated transmission losses on the end facets, beam focusing optics, i.e. lenses and objective, and propagation losses including coupling loss.

5.4.1 Modeling Guided and Unguided Modes

Since the ellipticity of HeNe source is determined to be 0.995, it can be assumed as a nearly perfect circular Gaussian beam¹. This gives a beam MFD of 14.8 μm for the HeNe source at the injection facet. Thus, the free propagation of the HeNe source inside 1.11 cm of waveguide length an unguided beam MFD of 451.0 μm calculated at the end facet of the sample as shown with Equation (5.6).

$$2\omega_u = (2\omega_{u,0}) \sqrt{1 + \left[\frac{M^2 \lambda l_c}{\pi n \omega_{u,0}^2} \right]^2} \quad (5.6)$$

Where $\omega_{u,0}$ is the beam waist at the injection face; λ is the wavelength of the beam; n is the refractive index of the sample; l_c is the length of the waveguides.

Due to the complexity of determining and simulating how the phase matching occurs between the injected Gaussian beam at 633 nm and the waveguide modes, the coupled light is assumed as the sum of well-known guided and modelled unguided modes. The unguided mode is modelled by assuming that all of the “top hat”, lowest numerical aperture rays of light, of the injected Gaussian beam to be guided. While the unguided mode profile is predominantly on the edge of the waveguides and in the vicinity of the tracks as the refractive index change extends on the side lobes of the modified tracks.

This can be implemented by taking a normalized circular Gaussian profile of unguided propagation at the exit face of the crystal subtracted by the normalized profile of the guided mode as shown in Equation (5.7) below.

¹ ISO Standard 11146-1: Circular power density distribution is defined as power density distribution (PDD) having ellipticity greater than 0.87.

$$P_{measured, unguided} = \frac{2TP_u e^{-\alpha_a l_c}}{\pi(\omega_u^2 - \omega_x \omega_z)} \int_0^{2\pi} \int_0^\infty \left[e^{-2r^2/\omega_u^2} - e^{-2r^2 \left(\cos^2 \theta / \omega_x^2 + \sin^2 \theta / \omega_z^2 \right)} \right] r dr d\theta \quad (5.7)$$

Where T are the transmission losses due to the lens, Fresnel and imaging objective; P_u is the unguided mode power at the injection facet; α_a is the absorption coefficient of pristine CaF_2 ; l_c is the length of the waveguides; ω_u is the beam waist at the end facet of the unguided mode; ω_x , ω_z are the beam waists of the guided mode in horizontal and vertical axes; r , θ are polar coordinates.

Thus, by subtracting the normalized elliptical Gaussian mode of the guided from the bulk propagation of the evolved circular Gaussian mode at the exit face, we can obtain the model of the unguided mode as shown in Figure 5-8 below.

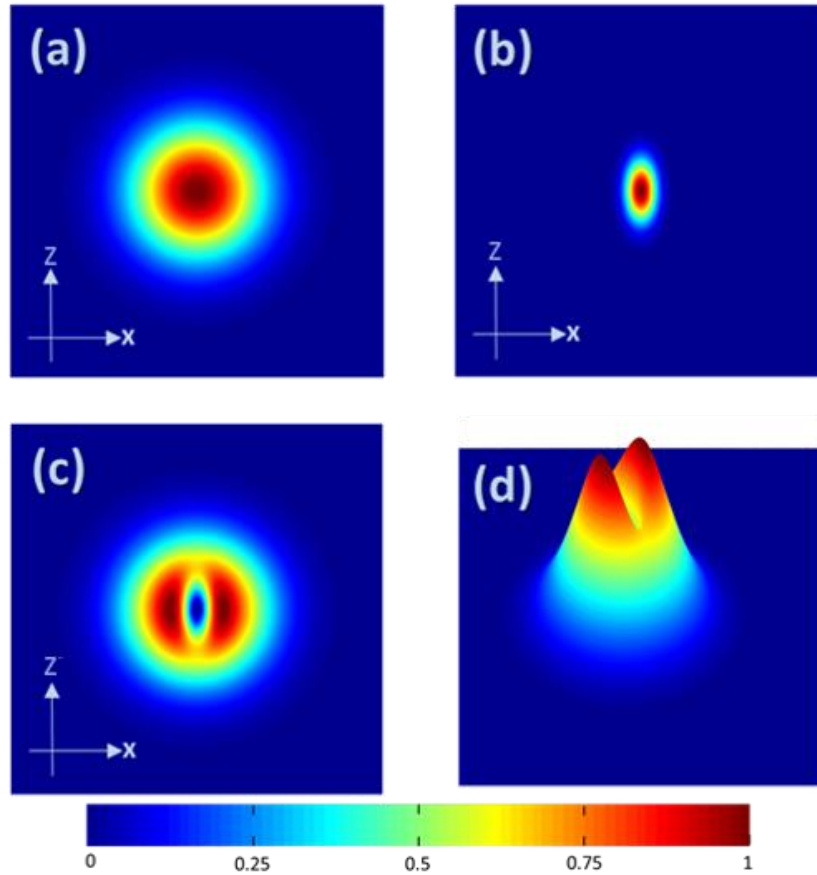


Figure 5-8 : Near Field, NF, MFD of modeled power density distributions. (a) Evolved unguided circular Gaussian mode in 2D, (b) Guided elliptical Gaussian mode in 2D, (c)

Modeled unguided mode at the exit facet of the sample in 2D and (d) the 3D view of the modeled unguided mode.

For example, Figure 5-8 shows the unguided circular mode model with a radius of $40\text{ }\mu\text{m}$ subtracted by the guided elliptical mode model of $\omega_x = 9\text{ }\mu\text{m}$ by $\omega_z = 18\text{ }\mu\text{m}$ which results the assumed model as shown in (c) and (d).

5.4.2 Setup

Modeling the unguided mode, we can modify the imaging part of the waveguide setup presented in Figure 5-4 in such a way that the total power / profile at power meter/ CCD camera position is measured with two different limits as shown in Figure 5-9. The first case, Figure 5-9 (a), shows the case where all of the unguided and guided beam is collected on the sensor, powermeter / camera. Whereas the second case, (b), shows that a portion of the unguided mode and the whole of the guided mode is collected. In this case, the pinhole size is in such a way that it totally encircles the guided mode, i.e. $2r_{pin} > \text{maximum of } (2\omega_x, 2\omega_z)$ while the edges of the pinhole are observed on the CCD camera, i.e. $2r_{pin} \lesssim 80\text{ }\mu\text{m}$.

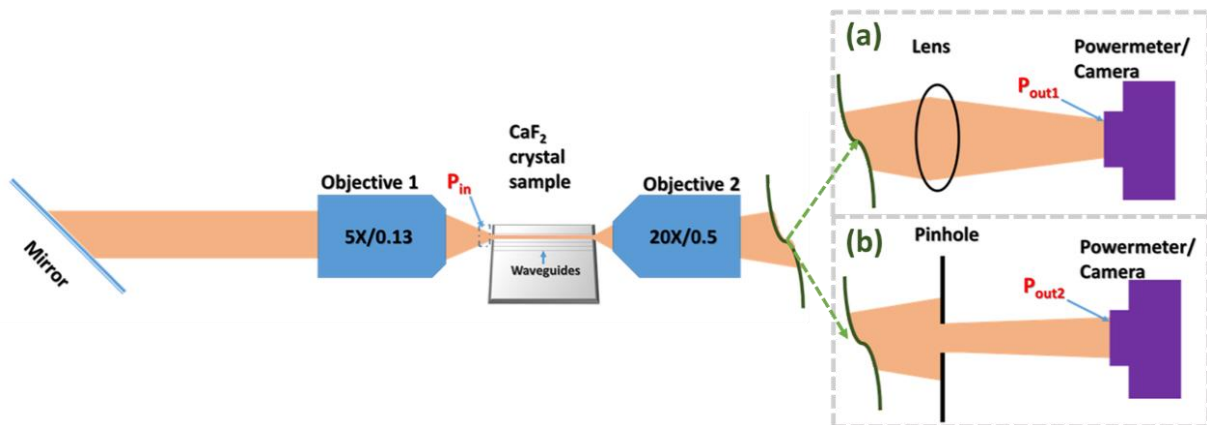


Figure 5-9 : Transmission loss setup. (a) P_{out1} is the power output measured as the sum of all the unguided mode and guided mode collected by focusing optics. (b) P_{out2} is the power output measured as the sum of a portion of the unguided mode and all of the guided.

Once the injection of the beam is optimized, the power measurement with and without pinhole for each waveguide of the sample should be performed. Thus, for each waveguide it was necessary to open and close the pinhole and this makes it necessary to accurately determine the pinhole radius for each case.

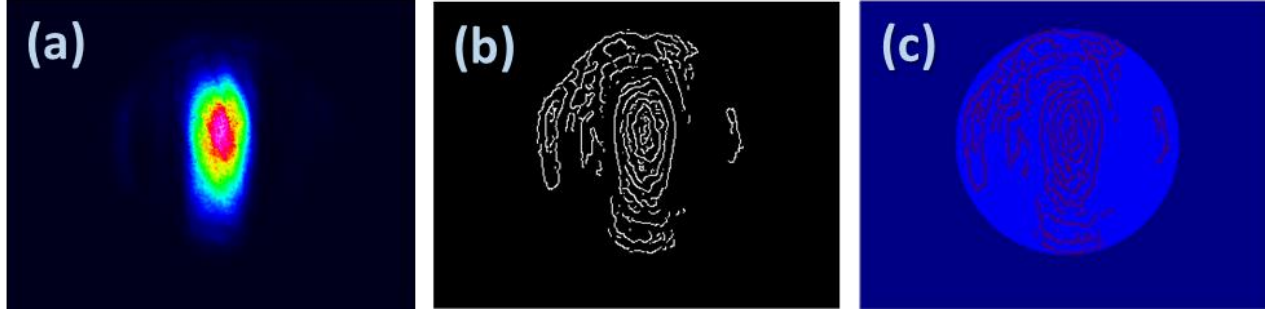


Figure 5-10 : (a) The profile of WG-1 with the pinhole edges encircling the guided mode. (b) Binary image of edges and (c) The numerically fitted circle, $2r_{pin} = 64.8 \mu m$, to completely encapsulate the edges.

For example, Figure 5-10 shows the profile of WG-1 imaged by using the setup as in Figure 5-9 (b). The profile on the left, Figure 5-10 (a), shows the guided mode encircled by the unguided mode until the edges of the pinhole. By employing a MATLAB inbuilt function which utilizes the Canny Method [136], by optimizing the tolerance level to find the edges only related with the pinhole and profile of guided and unguided modes encircled, we can find the binary image shown in Figure 5-10 (b). Once the edges are correctly determined, we can numerically fit a circle to completely encircle the edges, which should have an equivalent diameter of the pinhole, $2r_{pin}$.

5.4.3 Calculation and Result

As it is described in the previous section, for the given models of both guided and unguided modes, the power P_{in} , P_{out1} and P_{out2} can be described by the Equations **Error! Reference source not found.**, **Error! Reference source not found.** and **Error! Reference source not found.** below.

$$P_{in} = T_f (P_g + P_u) \quad (5.8)$$

$$P_{out1} = \left[\frac{2P_g}{\pi\omega_x\omega_z} e^{-\alpha_g l_c} \int_0^{2\pi} \int_0^\infty e^{-2r^2(\cos^2\theta/\omega_x^2 + \sin^2\theta/\omega_z^2)} r dr d\theta \right. \\ \left. + \frac{2P_u}{\pi(\omega_u^2 - \omega_x\omega_z)} e^{-\alpha_a l_c} \int_0^{2\pi} \int_0^\infty [e^{-2r^2/\omega_u^2} - e^{-2r^2(\cos^2\theta/\omega_x^2 + \sin^2\theta/\omega_z^2)}] r dr d\theta \right] T_f T_{obj2} T_{lens} \quad (5.9)$$

$$P_{out2} = \left[\frac{2P_g}{\pi\omega_x\omega_z} e^{-\alpha_g l_c} \int_0^{2\pi} \int_0^{r_{pin}} e^{-2r^2(\cos^2\theta/\omega_x^2 + \sin^2\theta/\omega_z^2)} r dr d\theta \right. \\ \left. + \frac{2P_u}{\pi(\omega_u^2 - \omega_x\omega_z)} e^{-\alpha_a l_c} \int_0^{2\pi} \int_0^{r_{pin}} [e^{-2r^2/\omega_u^2} - e^{-2r^2(\cos^2\theta/\omega_x^2 + \sin^2\theta/\omega_z^2)}] r dr d\theta \right] T_f T_{obj2} \quad (5.10)$$

Where P_{in} is the injected power just before the sample; P_g is the peak power of guided mode in mW; P_u is the peak power of the unguided mode in mW; T_f is the Fresnel transmission coefficient; T_{obj2} is the transmission coefficient of the objective 2 in Figure 5-9; T_{lens} is the transmission coefficient of the lens; α_g is the transmission loss of the waveguides in 1/cm; α_a is the transmission loss of the unmodified substrate which is 0.06 1/cm; l_c is the length of the waveguide in cm; ω_u is the beam waist at the end facet of the unguided mode; ω_x , ω_z are the beam waists of the guided mode in horizontal and vertical axes in μm ; r_{pin} is the pinhole radius in μm ; r , θ are polar coordinates.

Table 5-2 shows all the measured values of the transmission loss experiment. The power measurements, pinhole diameter and the transmission coefficient of the imaging optics of three separate experiments with the setup shown in Figure 5-9.

Table 5-2 : Transmission loss experiment measured values for three independent experiments. Where DLW E is the writing energy for each waveguide in μJ .

Waveguides		WG-1	WG-2	WG-3	WG-4	WG-5
DLW E (μJ)		0.56	0.52	0.48	0.44	0.41
Experiment 1	P_{out1} (mW)	3.48	3.32	3.46	3.36	3.53
	P_{out2} (mW)	1.81	1.73	1.55	1.14	1.14
	P_{in} (mW)	6				
	$2r_{pin}$ (μm)	64.75	47.94	58.52	67.24	64.13
Experiment 2	P_{out1} (mW)	3.47	3.34	3.52	3.23	3.59
	P_{out2} (mW)	1.98	1.8	1.64	1.33	1.19
	P_{in} (mW)	6.5				
	$2r_{pin}$ (μm)	56.03	74.71	60.39	75.95	71.60
Experiment 3	P_{out1} (mW)	3.42	3.25	3.4	3.29	3.55
	P_{out2} (mW)	1.89	1.75	1.66	1.31	1.275
	P_{in} (mW)	5.92				
	$2r_{pin}$ (μm)	53.54	69.11	68.48	77.82	65.99
T_{obj2}		0.92				
T_{lense}		0.94				

We can calculate T_f as 0.968 for the refractive index of CaF_2 of 1.43. Furthermore, T_{lens} and T_{obj2} are directly measured. Given the measured values in Table 5-2 and using the Equations **Error! Reference source not found.**, **Error! Reference source not found.** and **Error! Reference source not found.**, we can calculate P_g , P_u and α_g in which the transmission loss of the waveguides is given as:

$$\alpha_{loss}(dB/cm) = -\frac{10}{\ln 10} \alpha_g(1/cm) \quad (5.11)$$

As it was shown above, the unguided beam model only considers free bulk propagation subtracted by the confinement of the low numerical aperture. However, due to the comparable size of the negative refractive index change tracks, sub-micrometers, with the wavelength of the source, the diffraction effect of the tracks is significant in the vicinity, near-field, of the waveguides [137]. Therefore, we can conclude that the transmission loss calculations will result in an overestimation of the real losses of the waveguides which is also compared with other previously reported transmission loss measurements in crystals as presented in Figure 5-11 below.

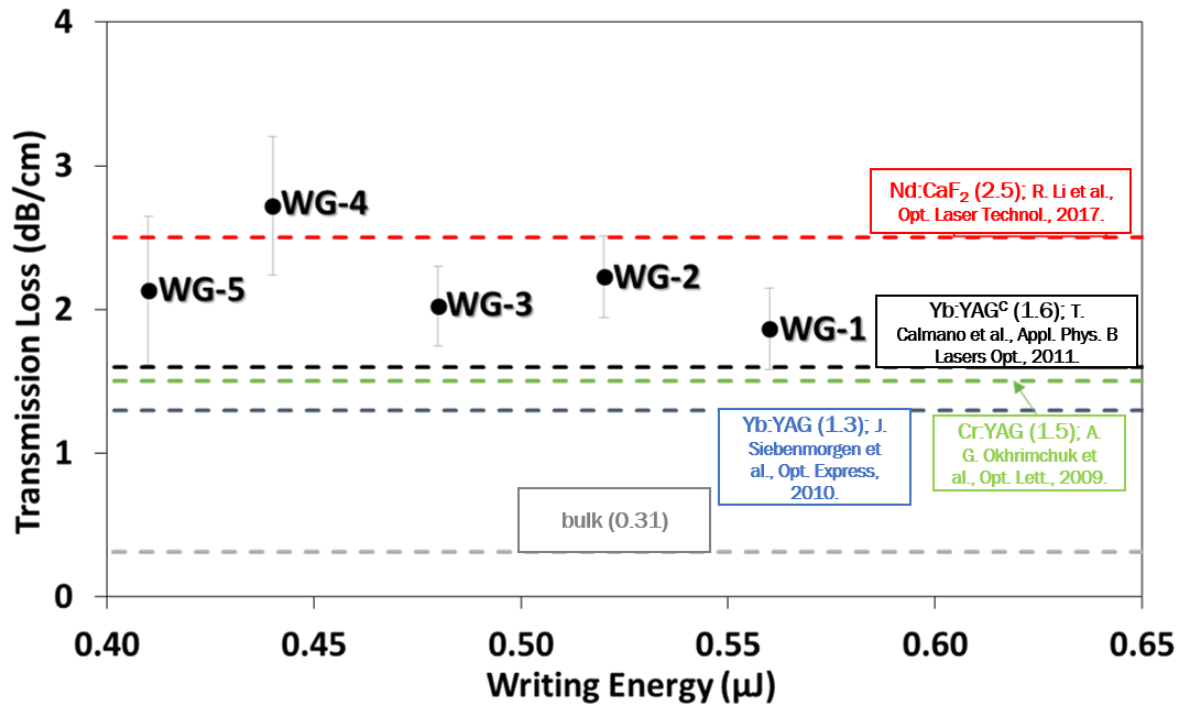


Figure 5-11 : Transmission loss (dB/cm) of the CaF₂ undoped crystal double-track waveguides in comparison with some previously reported transmission losses where red is a Nd:CaF₂ crystal [75]; black is a Yb:YAG ceramics [101]; green is a Cr:YAG crystal [109] and blue is a Yb:YAG crystal [106]. The gray line at 0.31 dB/cm is the transmission loss of the CaF₂ substrate.

The five waveguides of undoped CaF₂ exhibit a transmission loss between 1.9 dB/cm for WG-1 to 2.7 dB/cm for WG-4 while the bulk transmission loss is 0.31 dB/cm at 633 nm. This is close to some of the previously reported works on YAG crystals which were 1.3 dB/cm for Yb:YAG [106], 1.5 dB/cm for Cr:YAG [109] while 1.6 dB/cm was reported for Yb:YAG

ceramics [101]. In addition, recently waveguides written inside Nd:CaF₂ have been reported with a transmission loss of 2.5 dB/cm [75]. However, as it was mentioned above, our method is an overestimation of the real transmission losses, and better loss might result than for our “simple” model. The error bars in the measurements indicate the data from the three experimental runs.

5.5 Polarization Behavior of the Waveguides

Previous studies have shown that stress induced birefringence and selective guiding of only one polarization state has been reported in YAG crystals and ceramics [138], [106], [101], [104], [139], [140]. Similarly, we have observed that for all five waveguides, only the polarization parallel to the damage tracks was guided while exhibiting a Polarization Extinction Ratio, PER, between 15 – 20 dB, i.e. 1:32 to 1:100 parts as shown in Figure 5-12 (b).

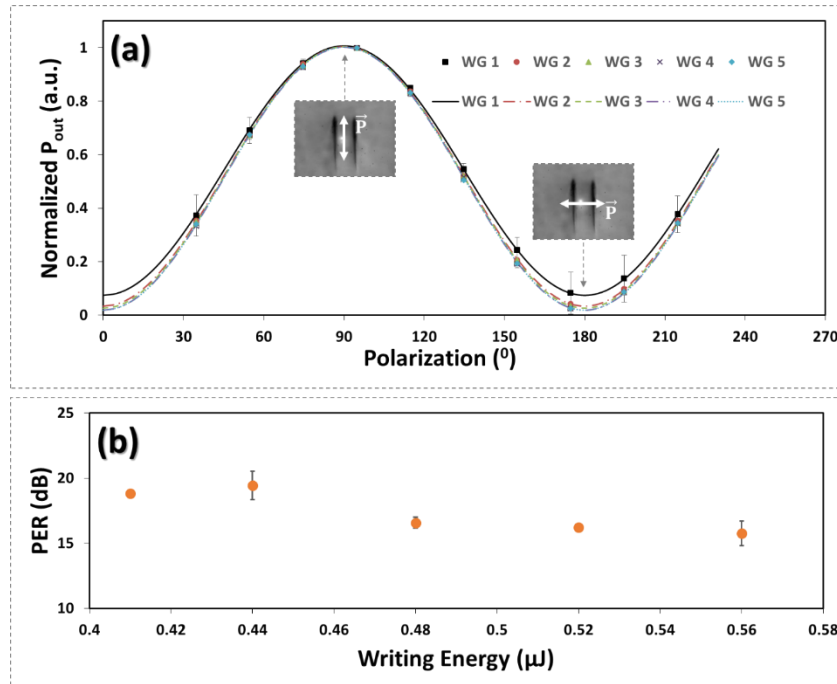


Figure 5-12 : Polarization dependent guiding of the five double track waveguides inscribed inside undoped CaF₂. (a) Normalized transmitted power based on the maximum value of transmitted power as a function of direction of light polarization. (b) Polarization Extinction Ratio (PER) of each waveguide.

A recent study by J. Qi et al. on polarization dependent guiding performances of LiNbO_3 crystals presented similar results. Propagating waves with the polarization parallel to the tracks is guided, i.e. TE mode for vertical double lines and TM mode for horizontal double lines are guided, while the polarization perpendicular to the double lines show high absorption, > 17 dB [141]. In addition, the simulation results in our case (vertical double lines) indicate strong absorption of the horizontal (s-) polarization. Given the fact that the birefringence is negligible for the conventional double track waveguides inside CaF_2 , the origin of this polarization dependent guiding is not yet completely understood.

5.6 Conclusion

In conclusion, the waveguiding properties of the fabricated structures were investigated at the wavelength of 633 nm by coupling the linearly polarized light of a HeNe laser source into the waveguides with an objective, $\text{NA} = 0.15$. The near-field guided mode profiles are elliptical, with an ellipticity less than 60 %. The maximum waveguide transmission losses were determined by considering an unguided mode model; which will result in more accurate if not over-estimation of the transmission loss measurement of the guided modes. The transmission loss of the five CaF_2 double track waveguides is between 1.9 dB/cm for WG-1 to 2.7 dB/cm for WG-4, which is close to previously reported transmission loss measurements inside YAG crystals. Furthermore, a study of the polarization dependence of the guiding of the waveguides showed that the waveguides act almost like perfect polarizers.

6 Refractive Index Change Measurement of Double Track CaF_2 Waveguides

As a continuation of characterizing the properties of the waveguides, this chapter presents direct refractive index measurements of the waveguides implementing the phase-contrast microscopy technique together with a Fresnel diffraction approach to determine the three-dimensional, 3D, refractive index change map along and in the vicinity of the modified tracks of the CaF_2 crystal. Section 6.1 briefly presents various techniques of refractive index change measurement and the comparative advantage of Quadriwave lateral shearing interferometry, QWLSI, which is a new application of phase-imaging microscopy for wavefront sensing. Sections 6.2 and 6.3 present the theory and the experimental setup for QWLSI, respectively. OPD measurements of the double track waveguides using QWLSI is demonstrated in Section 6.4. Section 6.5 presents a detailed discussion about the effect of Fresnel diffraction on the OPD measurements for the determination of the thickness of elements of the waveguides contributing to the phase difference measurement. Furthermore, the complete 3D refractive index profile is presented. Finally, Section 6.6 confirms this new approach for refractive index change measurements for double track waveguides inside crystals by comparing the mode field profiles of the simulation, by the Finite Difference Eigenmode (FDE) solver, and experimental results from the previous chapter.

6.1 Refractive Index Measurement Techniques

Various techniques and approaches for direct and indirect measurement of refractive index distributions have been developed and implemented. The convenience and measurement

accuracy of each technique depends on the type and geometry of the waveguides, the setup of the measurement, the theoretical analysis and estimation applied and so on.

For example, over the years various techniques have been considered to measure the refractive index change of three-dimensional waveguides with different geometries. Usually, three-dimensional distributions are two-dimensional ones longitudinally repeated in the lateral direction over the length of the waveguides. Thus, techniques that give an equivalent value for step index or two-dimensional longitudinal distributions are considered as good approximations to describe the overall refractive index change. To discuss just a few:

- **Mline technique:** can be applied by using a coupling prism in direct access and in close vicinity of the guiding interface [142], [143]. Although this technique is convenient for planar waveguide types, it will be difficult to implement it for embedded type waveguides that are being discussed here.
- **Near-field reflected/ transmitted method:** is based on reflected / transmitted intensity near the guiding facet in comparison with the substrate [57], [144]–[146]. This method requires polishing of the facet at an oblique angle and with a flatness as small as $\lambda/4$ and roughness smaller than 20 nm which is complex to achieve in our case.
- **NA measurement:** is done by a far-field measurement of the mode field at different distances from the end facet. The refractive index change can be approximated as $\Delta n \approx \sin^2 \vartheta_m / 2n$, where ϑ_m is the maximum incident angular deflection and n is the refractive index of the substrate [104], [113], [147], [148].
- **Electrooptic stress distribution:** is measured to indirectly access the unit cell volume changes. The change in volume is then related to the change in refractive index using the Clausius–Mosotti model [49], [114].
- **Quadriwave lateral shearing interferometry, QWLSI:** provides simple and direct measurement of refractive index modifications and detailed information about the 2D spatial map of the changes [149], [150]. This technique is based on Fourier analysis of a bi-dimensional and quasi-bi-sinusoidal interferogram, which results in both OPD and intensity image of the modified sample.

6.2 Principle of Quadriwave Lateral Shearing Interferometry (QWLSI)

Figure 6-1 shows the experimental configuration using an oil immersion objective of magnification 100X and $NA_{obj} = 1.3$ with condenser illumination of $NA = 0.15$ along with commercially available equipment SID4Bio from PHASICS Inc having a spatial resolution of 250 nm.

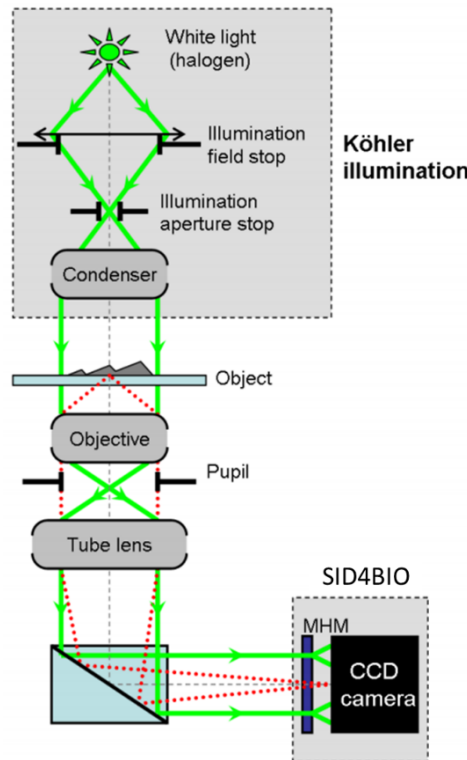


Figure 6-1 : Schematic layout of QWLSI setup for determination of OPD. MHM - Modified Hartmann Mask [150].

A direct measurement of the refractive index variation (Δn) between the pristine CaF_2 and the modified zone was measured by a phase-contrast microscopy method using a commercial wavefront sensor, quadriwave lateral shearing interferometer, QWLSI (SID4BIO, Phasics Inc.) directly plugged onto a lateral video port of an inverted microscope (Zeiss Axiovert 200 M Microscope, Göttingen, Germany).

In our case, a Modified Hartmann Mask (MHM) is used as multiwave interferogram. For example, for a given disturbed wavefront in 1D, the projections deviate by an amount δ as

shown in Figure 6-2 (a). The MHM has been optimized to diffract four first orders carried by four wave vectors. With these four replicas, the 2D phase gradients are recovered from the fringe deformation, by means of a Fourier deconvolution around the interferogram fringe frequency. In general, using Fourier analysis of interferograms, we can get both the OPD and the intensity images of the modified sample as shown in Figure 6-2 below.

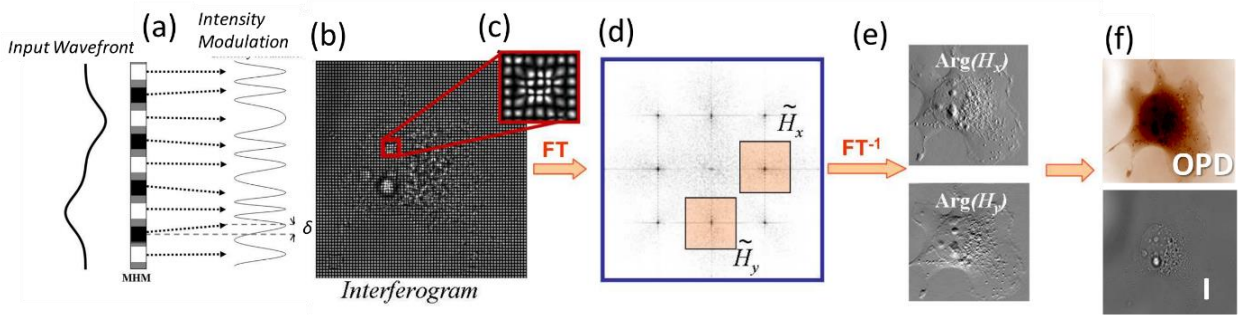


Figure 6-2: (a) 1D interferogram formation by a MHM in the case of a disturbed input wavefront; geometrical approach. (b) Interferogram obtained with an aberrant wavefront. (c) Zoom on a part of (b), visualization of the local frequency modulations. (d) Fourier Transform of (b). (e) Obtaining of 2 OPD orthogonal gradients by Inverse Fourier Transform of 2 sub-images of (b). (f) 2D Integration of the gradients to reconstruct the OPD and intensity (I) images. The figure is copied and modified from [150].

After the OPD of the modified sample is determined, the refractive index change modifications of our DLW inscribed waveguides can be determined by the following simplified formula as:

$$\Delta n = \frac{OPD}{t} \quad (6.1)$$

Where Δn is the refractive index change, OPD is the optical path difference; and t is the thickness of the element contributing to the refractive index change.

6.3 QWLSI Experimental Setup

Since the waveguides are written only a few hundred micrometers ($\approx 210 \mu\text{m}$) underneath the surface, the measurement of the 2D longitudinal (xz) view of the double tracks OPD spatial

map requires the illuminating beam to propagate all the way through the waveguide. Since the waveguides are more than 11 mm long, to avoid phase contributions from Fresnel Reflections from the surface of the sample, we need thin sliced samples. Therefore, the sample was sliced and polished down to a thickness of 1.37 mm by the Forschungsinstitut für Mineralische und Metallische Werkstoffe -Edelsteine/Edelmetalle- GmbH (FEE), Idar-Oberstein, Germany.

The setup is illuminated by a Halogen-Tungsten bulb with emission maximum centered at 709 nm which together with the silicon CCD spectral response gives a source centered at 550 nm. In order to deliver linearly polarized light, we placed a thin-film polarizer between the illumination field stop and aperture stop. Once the sample is placed on the slide (object in Figure 6-1), oil is dropped to the collecting objective which together with the tube lens forms well contrasted images that satisfy the Nyquist criterion on to the QWSLI interferogram. In the following section, we will discuss in detail the 3D-OPD measurement technique that we implemented for our specific case.

6.4 OPD Measurements

In order to access to the 3D refractive index map of the sample shown in Figure 6-3 below, we can either use a deconvolution of z -stack images or 2D-OPD measurements with different orientations. The different orientations of the sample can be lateral, or in the xz plane, which gives access to the contributions from the entire length of the tracks, and while the lateral, or xy plane, gives cumulative contributions limited to the zone in the vicinity of the tracks.

In general, a deconvolution of 2D z -stack images can be used to model the 3D structures of the modifications. This technique can, potentially, give us the direct measurement of the refractive index change by a simultaneous determination of the thickness of the structure, which contributes to the cumulative OPD, and the direct measurement of the OPD on the object plane. However, this approach requires a deconvolution of the 2D-sliced images by using the theoretical 3D-modulation transfer function (MTF) while considering the effect of the QWSLI gratings on the spatial frequencies. Furthermore, the thickness of modifications which contribute to the phase change are more or less equivalent to the size of the tracks that are so large as compared to the wavelength of the source and the resolution of the system. Thus, the

structures can no longer be considered by a point source approximation, which makes it even more complex to determine the exact mathematical analysis [151]. Therefore, we opted for making lateral (xy -plane) and longitudinal (xz -plane) 2D direct OPD measurements with polarizations parallel and perpendicular to the tracks. The different polarization measurements are done to determine the birefringence/retardance at least between the fundamental orthogonal axes with respect to the orientation of the tracks.

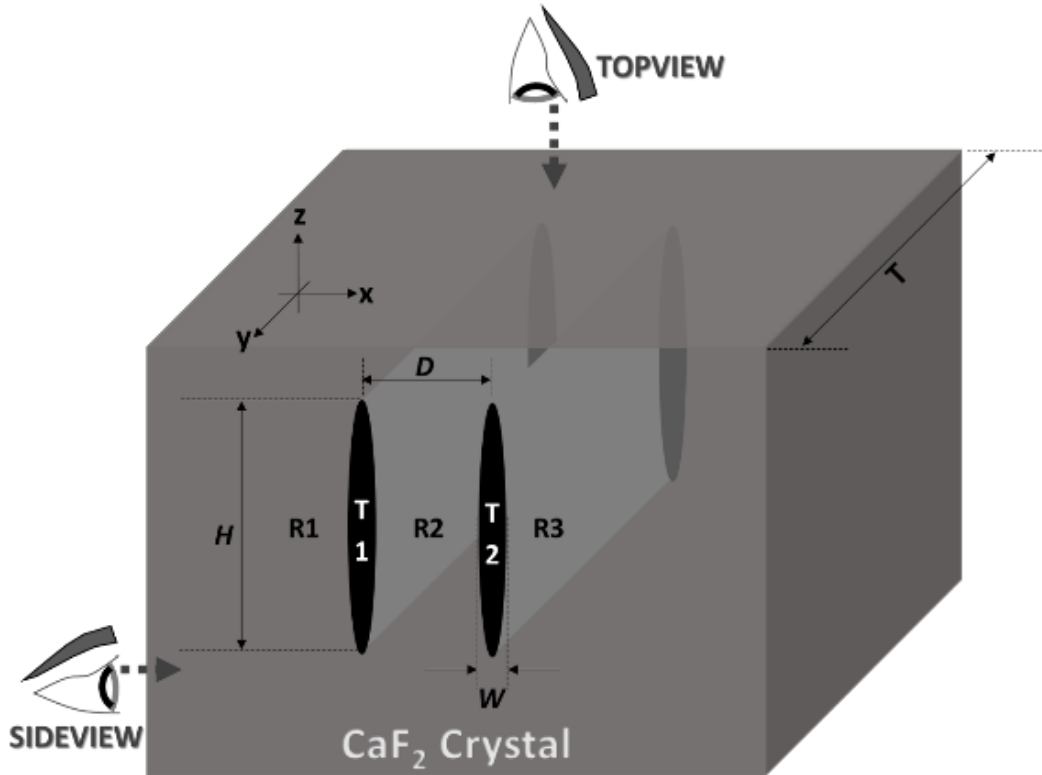


Figure 6-3 : 3D schematic of the double track waveguide inscribed inside the CaF₂ crystal. T1 and T2 are the modified pairs of track; R2 is the region in between the tracks; R1 and R3 are the sidelobe regions of the tracks T1 and T2, respectively; $W \approx 6 \mu\text{m}$ and $H \approx 40 \mu\text{m}$ are the average width and height of the tracks, respectively; $D = 20 \mu\text{m}$ is the distance between the tracks T1 and T3; and $T = 1.37 \text{ mm}$ is the thickness of the sample.

In addition, since the tracks are inscribed at a depth of around 0.21 mm, for the given thickness of a sliced sample, $T = 1.37 \text{ mm}$, the condenser NA should be below 0.15 for OPD measurements in the xz -plane, sideview. We placed the sample using piezoelectric controlled stages in order to align the center of the CCD approximately at the midpoint between the double tracks. Figure 6-4 shows the OPD measurements of lateral and longitudinal 2D-OPD distributions of all the five waveguides written with different energies.

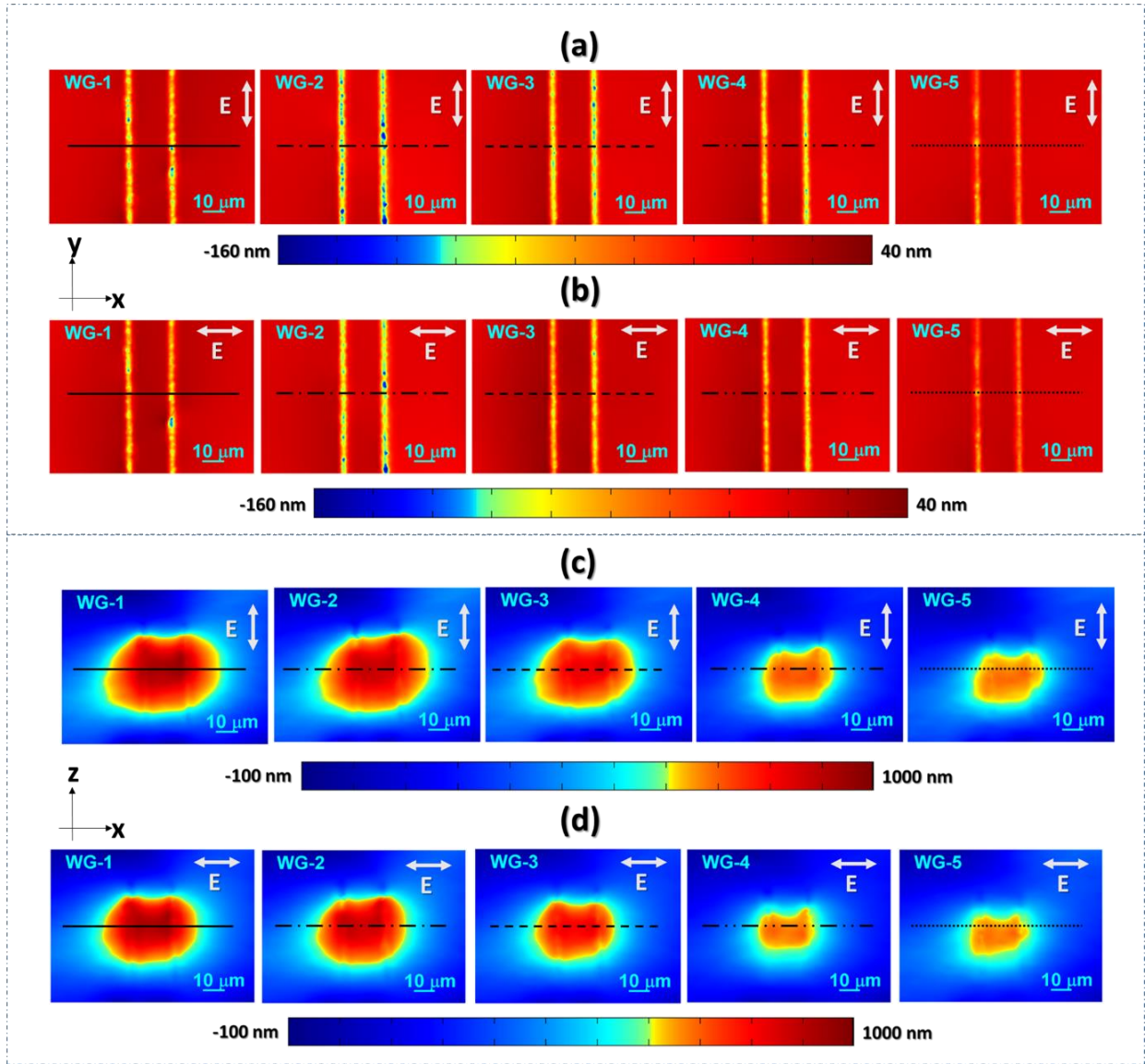


Figure 6-4 : OPD measurements along the double tracks of the waveguides. (a) and (b) show the OPD measurement in the lateral (xy-plane), while (c) and (d) show the longitudinal (xz-plane) measurements. (a) and (c) are measurements with the polarization parallel to the track while (b) and (d) show OPD measurements for the polarization perpendicular to the tracks.

As it is shown in the figure above, (a) and (b) show the OPD measurements in the xy-plane. The maximum OPD that can be measured in this case is less than 40 nm which is close to the error tolerance of the OPD measurement set up, which is ± 10 nm. Therefore, although the OPD measurement along the tracks has relatively larger absolute values as compared to the system error value, the OPD measurement in the vicinity will not be considered due to its relatively small value. Similarly, as it is shown in (c) and (d), the OPD measurement in the vicinity of the tracks in the xz-plane results in a value much larger than the measurement in the xy-plane, which shows that the thickness of the material contributing to the change in refractive

index is much bigger than the thickness of the tracks, H , being between 30 μm and 40 μm . However, the OPD measurements along the tracks in the xz -plane, sideview, is totally overwhelmed due to diffractions from the tracks, which are 1-2 μm and nearly comparable to the system resolution. Furthermore, since there is strong guiding in the vicinity of the tracks the diffraction is enhanced, and thus the tracks are not clearly mapped.

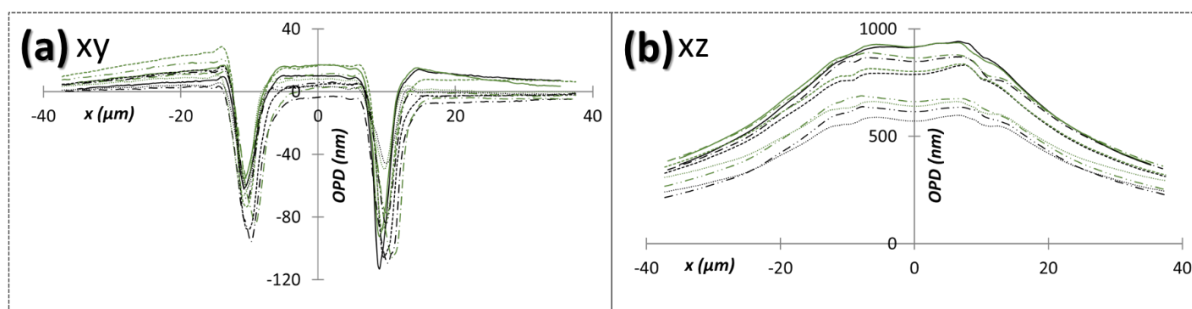


Figure 6-5 : Line profile of the OPD measurements. (a) xy -plane. (b) xz -plane. The solid line shows WG-1; the broken line with one dot shows WG-2; the broken line shows WG-3; the broken line with two dots shows WG-4; and the dotted line shows WG-5. Black color indicates measurements with the polarization parallel to the track, while green color indicates measurements perpendicular to the tracks.

Figure 6-5 shows the line profile of the topview and sideview in (a) and (b), respectively. The corresponding lines are also sketched in the 2D-profiles of Figure 6-4 above. As it can be seen in the figure, the difference between the measurements of the two polarizations are always less than 5 %. Therefore, we can neglect birefringence and consider the refractive index modifications to be symmetrical in all directions. Given this approximation, we can model the 3D refractive index change of the tracks by using the 2D-OPD measurements divided by the thickness of the elements that are contributing to the change. Particularly, as it was explained above, we will consider OPD measurements in the vicinity of the tracks for the xz -plane and the OPD measurements along the tracks for the xy -plane in the following section to determine the 3D-profiles of the refractive index change of the double track waveguides. Furthermore, the small pixel shifts and misalignments at the center between measurements are corrected by cropping and rescaling the 2D-OPD profiles using a Matlab program to align the tracks perfectly.

6.5 OPD measurements to 3D Refractive Index Map

In order to calculate the 3D refractive index map from the 2D-OPD measurements, the thickness of the modified index object contributing to the phase change in the OPD measurement should be known. It is important to state that this thickness could be lower than the real object dimension, and it must be considered as an equivalent diffraction length of the object contributing to the OPD. Once the thickness of the diffracting object is known for a given point in the OPD measurement, it is straight forward to calculate the 2D refractive index change.

6.5.1 Thickness of Longitudinal Elements

6.5.1.1 *Relationship between Fresnel Number and Depth of View*

Consider a plane wave diffracted at a slit of defined dimension, $2a$, as shown in Figure 6-6. The structure of diffracted light on the screen S at a position, Z , is directly related to the size of the aperture, a , the wavelength, λ , and the distance Z . Theoretically, these different regimes of diffraction both in the near field and far field can be described by:

- Full wave Helmholtz equation, $Z \lesssim \lambda$.
- Rayleigh-Sommerfeld and Fresnel-Kirchoff integrals for $Z \gg \lambda$.
- Fresnel scalar approximation for $Z \gg \sqrt{\frac{\pi}{4\lambda} [(x - x_0)^2 + (y - y_0)^2]_{max}^2}$.
- Fraunhofer approximation for $Z \gg \frac{\pi(x_0^2 + y_0^2)}{\lambda}$.

For the setup described in the previous section, the objective acts as a low pass spatial filter in which the contributions of the OPD that is formed onto the CCD camera comes from the refractive index difference observed in the near field. This can be defined as the number of Fresnel zones that can be fitted when observed at a distance Z from the screen. In other words, this is the result of interference between waves arriving from different Fresnel zones

which can be described quantitatively using the so-called Fresnel number, N_f , as shown in Equation (6.2).

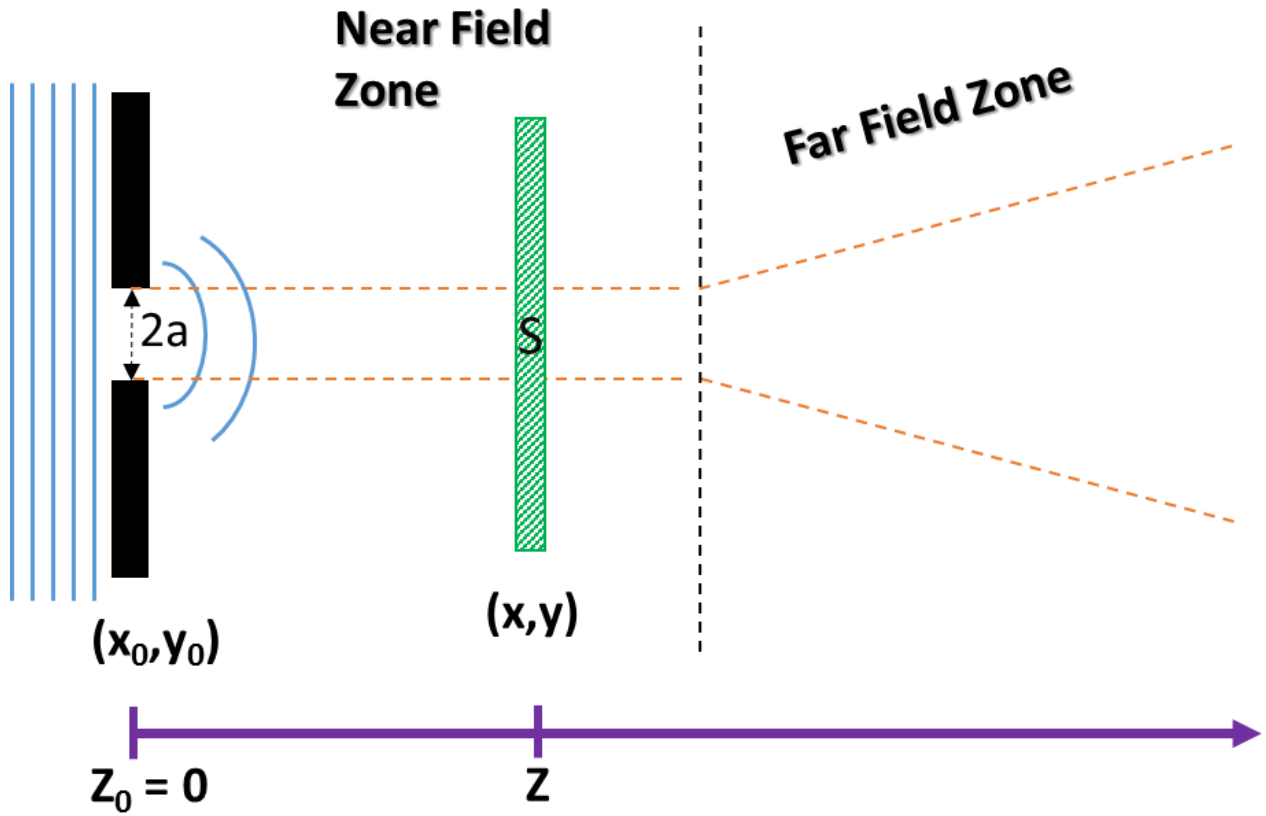


Figure 6-6 : Near-Field and far field diffraction of a plane wavefront at an aperture slit of diameter $2a$.

$$N_f = \frac{a^2}{\lambda Z_{cutoff}} \quad (6.2)$$

Where a is the characteristic radius of the element contributing to the diffraction; λ is the wavelength of the source; Z_{cutoff} is the cutoff distance between the screen and the element.

Therefore, the Fresnel number is intrinsic for the optical setup we consider and it is calculated based on the dimensions of the contributing element and their distance from the screen.

Thus, the total OPD contributions observed in the longitudinal plane of laterally extended waveguide tracks from the object plane, one end facet, to 1.3 mm, another end facet, can be summarized as the sum of m Fresnel zone contributions.

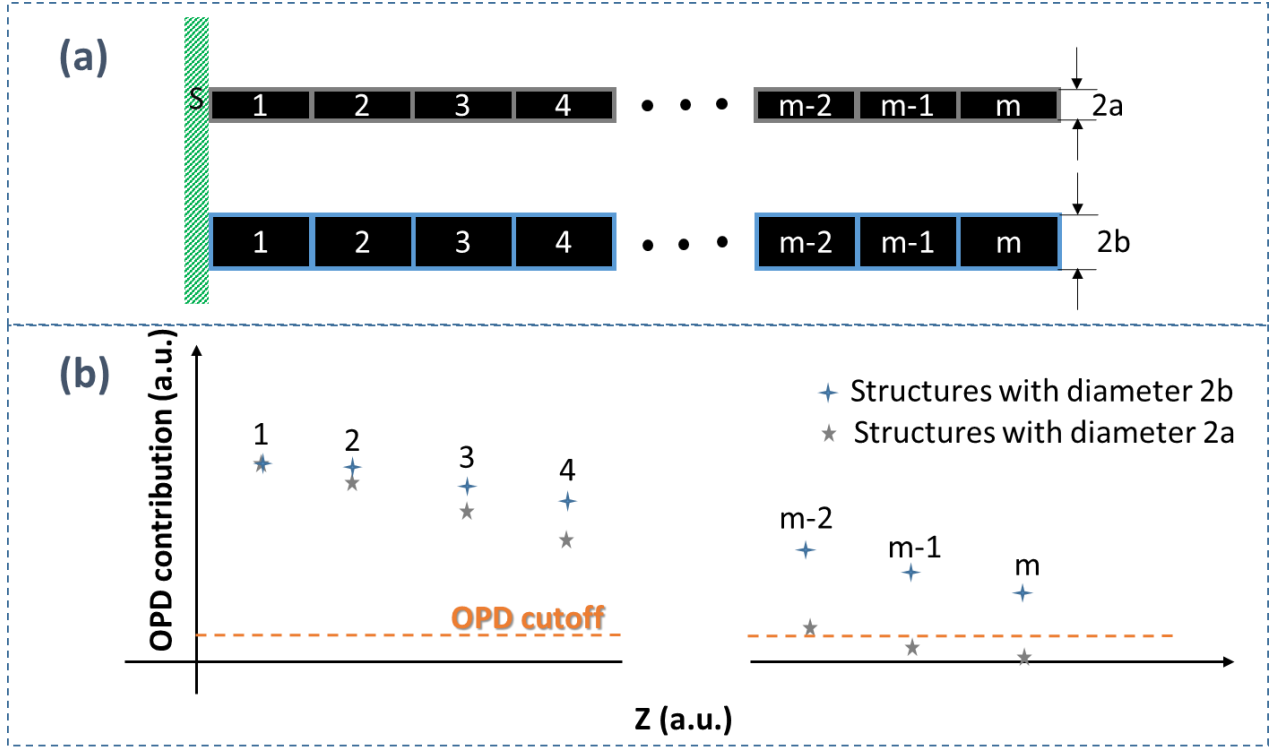


Figure 6-7 : (a) Sketch of waveguides with the OPD contributions with discrete elements for different Fresnel zones. (b) The plot of evolution of the OPD contributions from different layers of discrete Fresnel zones with radii $b > a$.

As shown in Figure 6-7, the total OPD contribution from the waveguides is divided into several layers of Fresnel zones of which the contribution from each layer is plotted in (b). It can be theoretically observed that the OPD contribution from the layers decays slowly for bigger size elements, in this case the OPD contributions for a waveguide with dimension, b , decay slower than for a waveguide with dimension, a . Since the Fresnel number is dependent solely on the imaging system, for the given threshold of OPD contribution, the Fresnel number stays constant. Therefore, in the coming sections we will be discussing a way to find the Fresnel number of the OPD measurement setup especially for longitudinal plane measurements. Once the Fresnel number is determined, we will apply it on our waveguide OPD measurements to calculate the spatial map of the refractive index changes of the waveguides.

6.5.1.2 *Determination of Depth of Field for Longitudinal OPD Measurements*

When the track is viewed on its two-dimensional longitudinal view under the microscope, in which the track transverses all the way through the thickness, it will be the contribution from all path differences along the whole thickness that will arrive at the objective aperture. As it is evident that, in the k-domain, the microscope/lens acts as a low pass filter, for the NA=1.3 oil immersion objective, only contributions coming from points within the spatial cutoff frequency, due to the focusing setup, can be considered. This limit is also called depth of field of the focusing system. Thus, to determine the depth of field, we started by inscribing micro-stairs of 500 nm in length with an average power (P_{av}) of 1.54 W at 10 MHz using a 20x NA=0.4 objective. Since the stairs are inscribed in the thermal regime [42], we assume the profile of refractive index change is of spherical shape as it is depicted in Figure 6-8, refer to Section 2.1.3 for more explanation. The diffraction limited beam diameter at the waist for the given microscope objective is 3.1 μm , thus the translation of the stairs is too short as compared to the expected focal diameter.

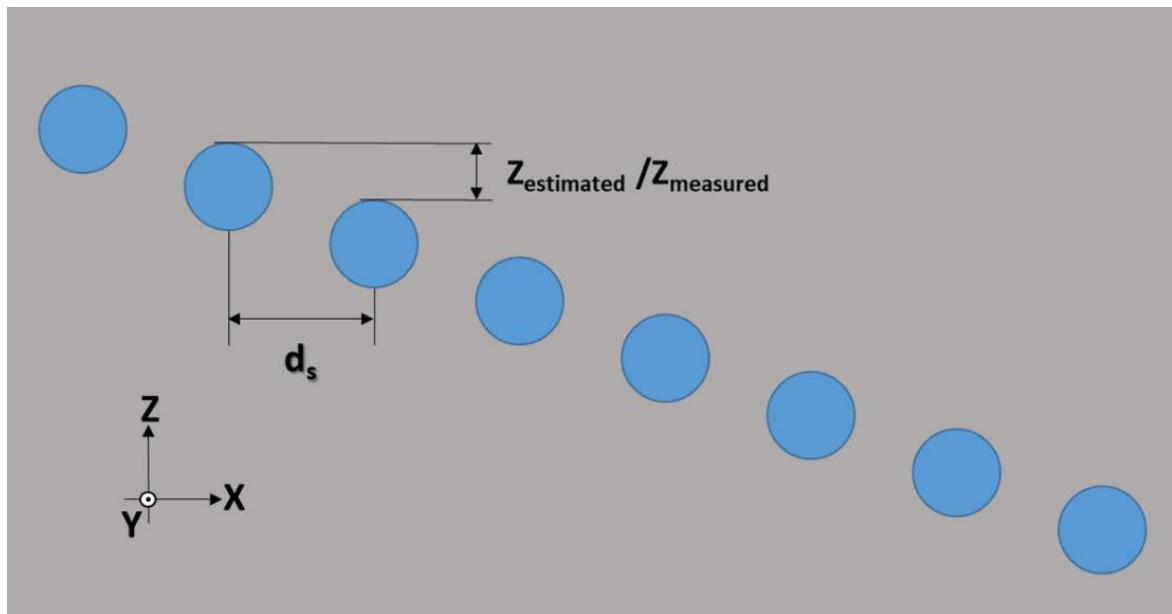


Figure 6-8 : 0.5 μm long stairs written with 0.15 μJ at 10 MHz with different distance between them (d_s) and different step in depth (Z).

A total of 12 types of stairs are written with different steps in depth ($Z_{\text{estimated}}/Z_{\text{measured}}$), distance between the stairs (d_s) at speed of $10 \mu\text{m/s}$ as it is depicted in Figure 6-8. For each type of beads, the obtained OPD images show that the modifications are localized and circular, Figure 6-9.

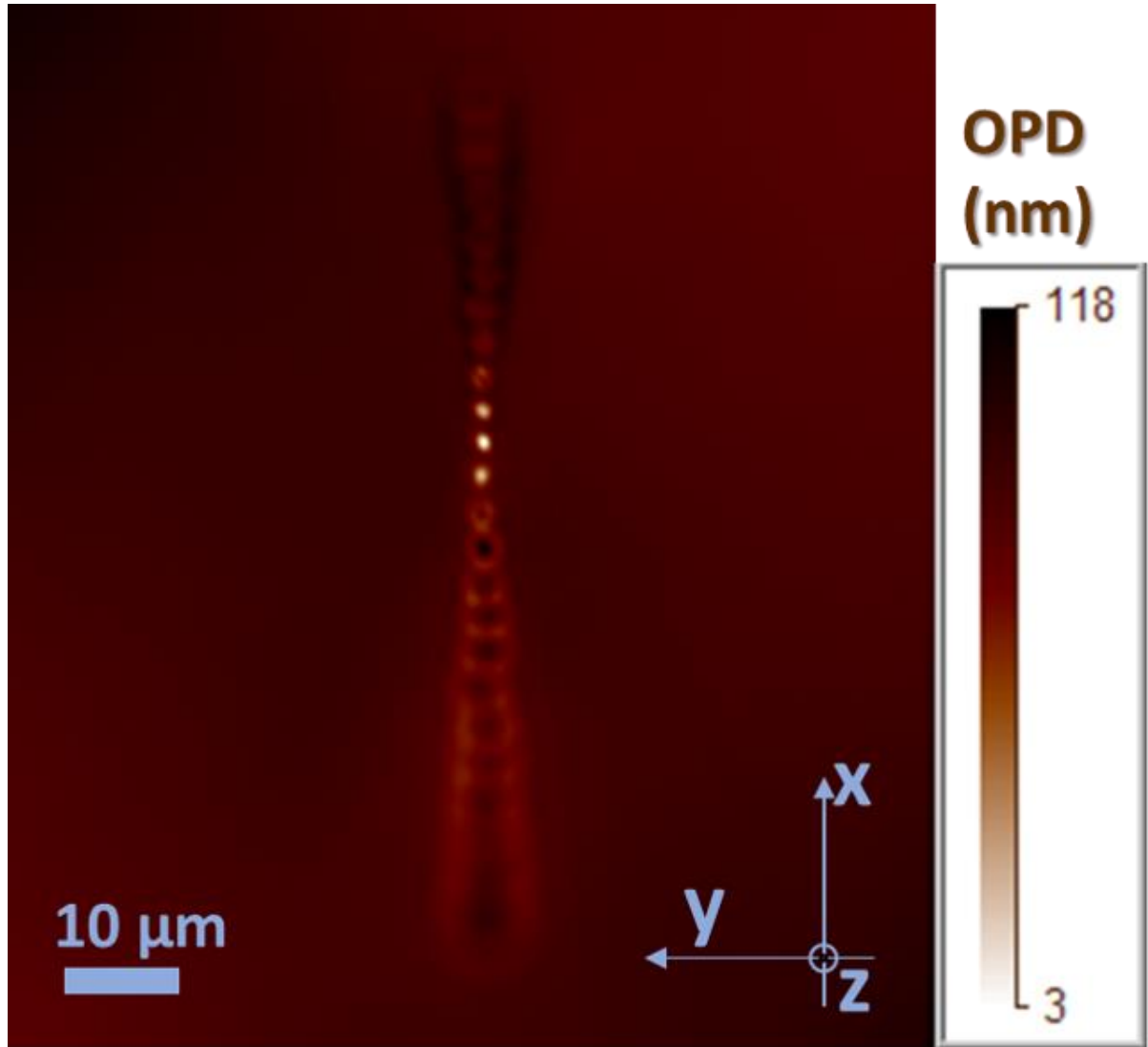


Figure 6-9 : OPD (nm) measurement of stairs with an d_s of $2 \mu\text{m}$ and mechanical depth step of $0.1 \mu\text{m}$.

As it can be observed from the figure, beads near the focal plane are smaller and more localized while the circles get wider and blurry further from the focal plane. The blurred circles with the solid centers and the void center show that the image plane is localized before and after the object plane, respectively. It is shown, in this particular example that, the raw measurement of

the phase image of one of the stairs with three stairs in the middle, i.e. around the object plane, clearly visible.

Table 6-1: Different parameters of the stairs selected for post processing. Exp # - Experiment parameter number; d_s - distance between the stairs; Estimated z (μm) - mechanical depth multiplied by the refractive index of CaF₂ at the wavelength of 1030 nm; Measured z (μm) - measured depth under the microscope; P (W) is the writing power measured just after the AOM in the writing setup; Total # stairs is the number of stairs inscribed for each given parameter.

Exp #	d_s (μm)	Estimated z (μm)	Measured z (μm)	P (w)	Total # stairs
12	3	0.29	0.2	1.54	50
10	2	0.29	0.38	1.54	30
9	3	0.29	0.44	1.54	30
6	2	0.72	0.78	1.54	25
5	3	0.72	0.87	1.54	25
8	2	1.43	1.55	1.54	15
7	3	1.43	1.57	1.54	15

Table 6-1 shows the parameters of some of the stairs which were selected for post processing. The post processing is performed using a MATLAB program. For each experiment, the OPD images were normalized and inverted to give the image as shown in Figure 6-10. As it is clear on the transformed image, the stair fabrication is localized for the length of 0.5 μm and a theoretical beam diameter of 2.2 μm . Thus, the inscribed stairs can be approximated by a 2D Gaussian profile to find the smallest stair radius, which is assumed to be the closest stair to the object plane. Only stairs with non-overlapping vertical and horizontal boundaries are selected for processing as shown in Figure 6-10 (b) below.

The phase images of the selected non-overlapping stairs were taken and fitted with a Gaussian profile for reconstruction with a 2D-Gaussian formula as shown in Equation (6.3) below.

$$I = A_0 e^{-\frac{(x-\mu_x)^2}{2\sigma_x^2} - \frac{(y-\mu_y)^2}{2\sigma_y^2}} + A_b \quad (6.3)$$

Where A_0 is the maximum intensity of the 2D-Gaussian profile; μ_x and μ_y are mean values, centers of the profile in horizontal and vertical directions, respectively; σ_x and σ_y are the standard distributions of the profile in horizontal and vertical directions which are related with the 4σ –diameters as $\omega_x/2$ and $\omega_y/2$, respectively; A_b is the background intensity.

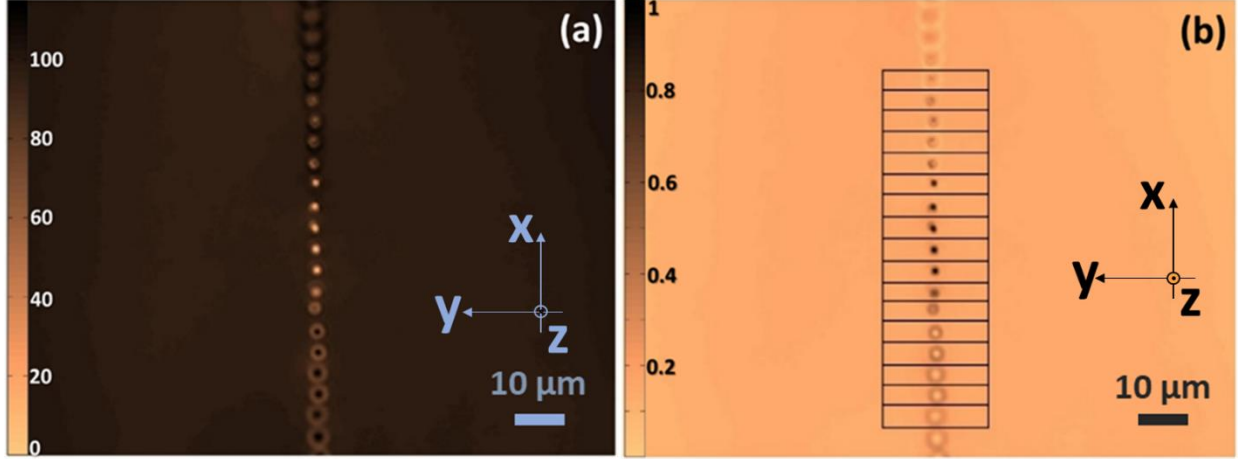


Figure 6-10 : (a) Raw measurement of OPD (nm) of the stairs of Exp # 5 ($d_s = 3 \mu\text{m}$ and step of depth $= 0.5 \mu\text{m}$) with $0.15 \text{ NA}_{\text{condenser}}$, (b) Normalized, inverted and selected stairs after transformation.

Given the fact that the sample is illuminated by a very small $\text{NA}_{\text{condenser}}$ and the aperture of the imaging is only 2 mm for an approximate illuminated beam diameter of 6 mm, we can reasonably approximate the illumination as a plane wave. With this assumption, the contributions to the OPD are coming within the area bounded by the stair closest to the object plane of the imaging system [151], thus the OPD of the stairs coming from “out-of-focus” area can be masked with the fitted profile smallest stairs as shown in Figure 6-11.

As shown in Figure 6-11 below, after masking the stairs with the smallest element, discrete 2D spatial integration of the masked intensity image of each stair is calculated according to Equation (6.4) by implementing the Trapezoidal rule. Then for each given integral value, the equivalent elliptical cylindrical volume with the x and y radius of the smallest element and height is calculated as a OPD contribution.

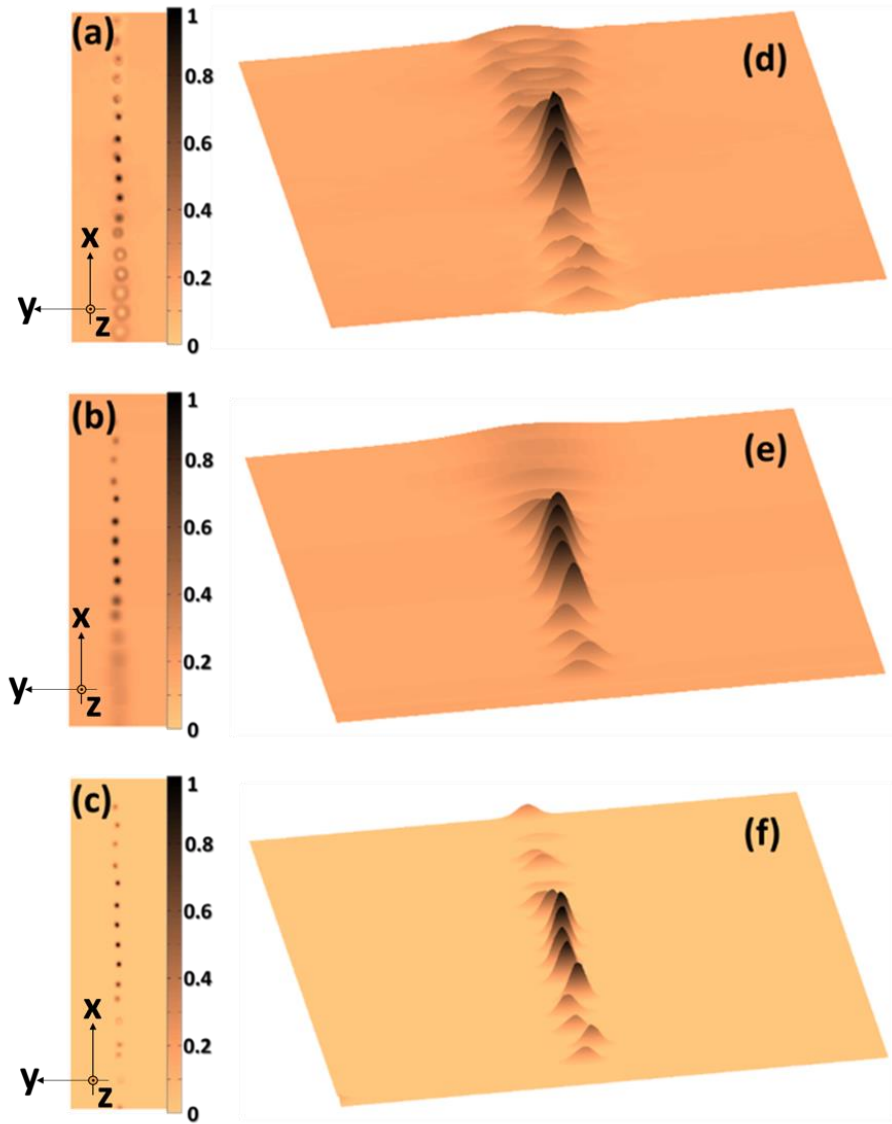


Figure 6-11 : 2D- and 3D-images of post processing of the selected stairs (Exp#5). (a) Selected and normalized stairs. (b) Fitted stairs to find the smallest element and (c) masked stairs based on the smallest element. (d), (e) and (f) show the respective 3D-images.

Consequently, for each stair experiment, i.e. different writing parameter stairs, the OPD contributions are plotted against the measured/calculated depth z . The z -intercept is assumed to be at the point where the OPD contribution is at its maximum and can be calculated based on simple Gaussian/parabolic fit just for the sake of centering the maximum value on the z -axis, i.e. with the physical meaning of centering the OPD contributions at the object plane, as shown below in Figure 6-12.

$$I_{2D} \approx \frac{h_x h_y}{4} \left\{ \begin{aligned} &f(x_0, y_0) + f(x_0, y_f) + f(x_f, y_0) + 4 \sum_{i=2}^{n_y} \sum_{j=2}^{n_x} f(x_j, y_i) + \\ &2 \sum_{i=2}^{n_y} [f(x_0, y_i) + f(x_f, y_i)] + 2 \sum_{j=2}^{n_x} [f(x_j, y_0) + f(x_j, y_f)] \end{aligned} \right\} \quad (6.4)$$

Where x_0, y_0 are the initial coordinates; x_f, y_f are the final coordinates; h_x, h_y are steps in x and y directions, respectively; n_x, n_y are the total number of pixels in the x and y directions, respectively.

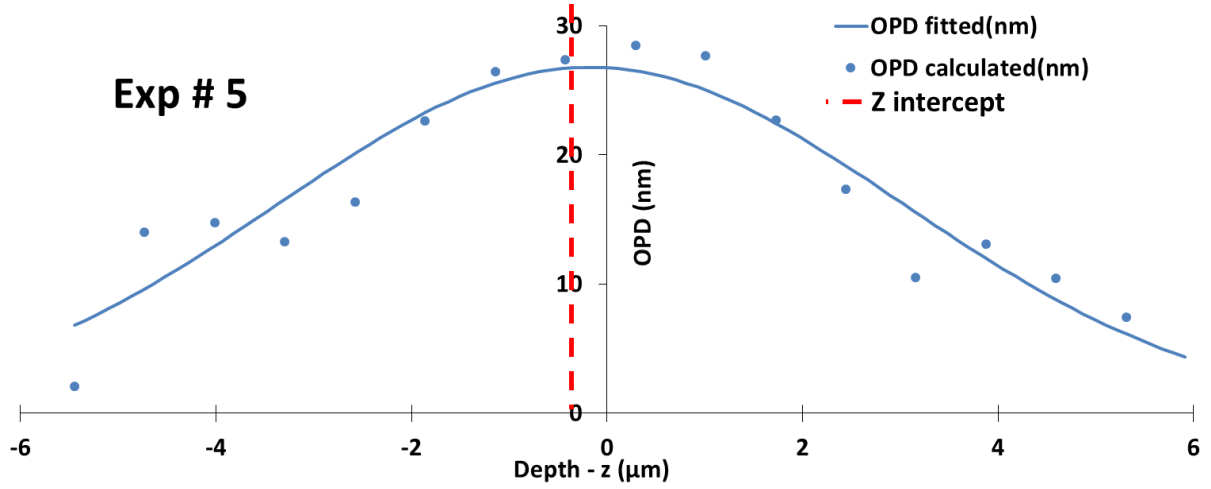


Figure 6-12 : Equivalent OPD contribution of the stairs in Exp # 5 with blue dots – equivalent OPD calculated as the height of the elliptical cylinder for the same volume of the masked stair; solid blue line – fitted parabolic curve to find the Z intercept, and the red broken line indicates the z intercept at $-0.29 \mu\text{m}$.

Since the different experiments have different depth and distance between consecutive stairs, we can superimpose the OPD contributions from all experiments as shown in Figure 6-12.

By considering the integral of all the normalized OPD contributions as shown in Equation (6.5), we can calculate the depth of field for the collective OPD contributions of the stairs as an equivalent rectangular area where the OPD contributions of all the stairs are assumed to be 100 % bounded within this rectangular area.

$$\begin{aligned}
 DoF &= \frac{1}{2} OPD_{int} = \frac{1}{2} \int_{z_{min}}^{z_{max}} OPD(z) dz \\
 &\approx \sum_{k=1}^N \frac{OPD(Z_{k-1}) + OPD(Z_k)}{4} (Z_k - Z_{k-1})
 \end{aligned} \tag{6.5}$$

Where DoF is the Depth of Field (μm); OPD_{int} is the total integral of all the OPD contributions of the stairs from all the experiments; $OPD(z)$ is the OPD contribution of a stair at z ; while the approximation on the right side of the equation shows the numerical integration of all the OPD contributions using Trapezoidal rule.

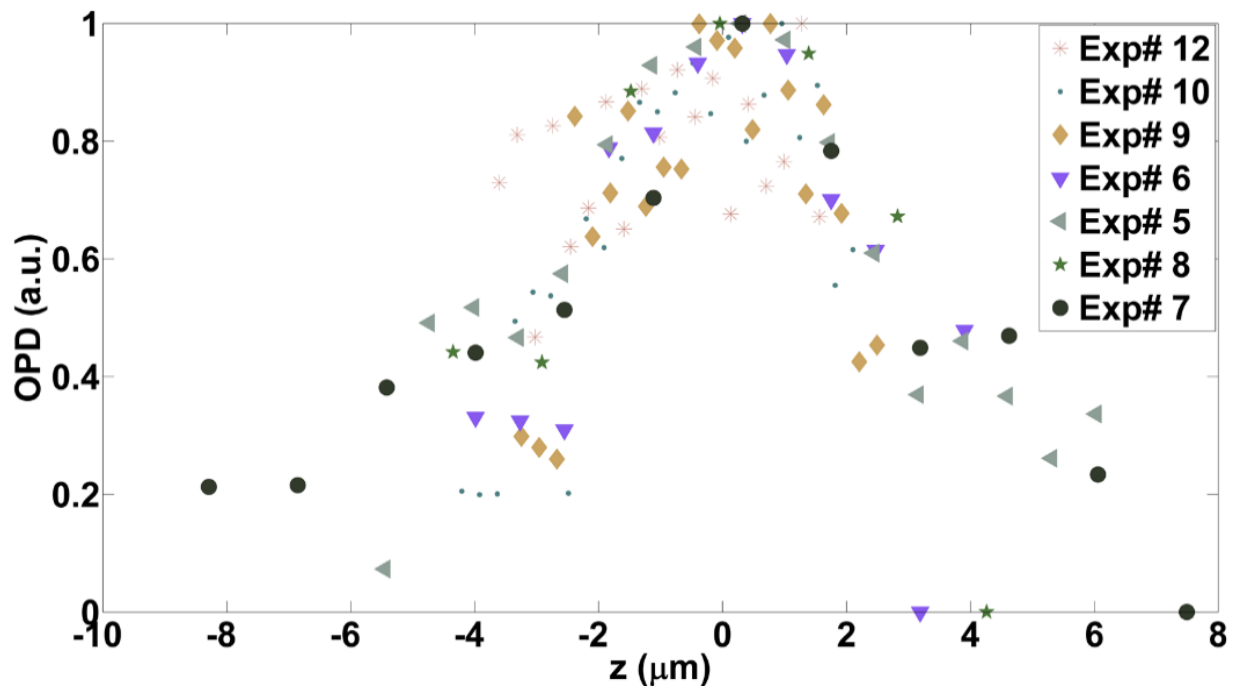


Figure 6-13 : The OPD contribution of stairs of different experiments with different step and distance between stairs superimposed together.

Once the DoF is calculated and the characteristic radius of the stairs is determined, we can calculate the Fresnel Number, N_f , of the OPD setup described in Section 6.5.1.1 with Equation (6.2). This results in an N_f value of 0.181 for the determined characteristic radius $a = 0.6 \pm 0.043 \mu\text{m}$, given the wavelength of $0.55 \mu\text{m}$ of the halogen source and calculated DoF of $3.62 \mu\text{m}$.

For the given Fresnel number of the OPD setup, we can calculate the longitudinal depth of field for the OPD measurements in the xz -plane. As the refractive index has the highest value in between the tracks as shown in Figure 6-4 and since the guided mode is confined between the tracks, the mode field radii of the guided fundamental mode are assumed to be the characteristic radii as shown in Table 6-2 below. However, it should be understood that the refractive index change extends on both sides of the tracks, although the part of refractive index change in between the tracks is more significant and consequently the gaussian mode field radii will result the smallest depth of field that can be calculated.

Table 6-2 : Calculated Depth of Field for the xz -plane of refractive index measurements.

Parameters	WG-1	WG-2	WG-3	WG-4	WG-5
<i>MFR_x (μm)</i>	9.08	8.06	8.21	7.61	9.16
<i>MFR_z (μm)</i>	17.88	16.25	15.85	17.18	16.39
<i>DoF_{calc} (mm)</i>	1.63	1.32	1.31	1.31	1.51
<i>DoF_{real} (mm)</i>	1.37	1.32	1.31	1.31	1.37

As it is shown in Table 6-2 above, the calculated longitudinal thicknesses based on the above assumptions are greater than the thickness of the slice itself for WG-1 and WG-5 in which we will consider the thickness of the sample. For the rest of the double tracks, we will consider the calculated values to determine the refractive index change from the OPD measurements in the upcoming sections.

6.5.2 Thickness of Lateral Elements

As it was shown in Section 6.4, the refractive index change is localized around the double tracks of the waveguides, it is reasonable to consider the thickness of the tracks to be the thickness of the structure contributing to the OPD in the xy -plane. The length of the tracks, H , can be determined by generating a binary mask from the intensity images in the xz -plane as shown in the figure below.

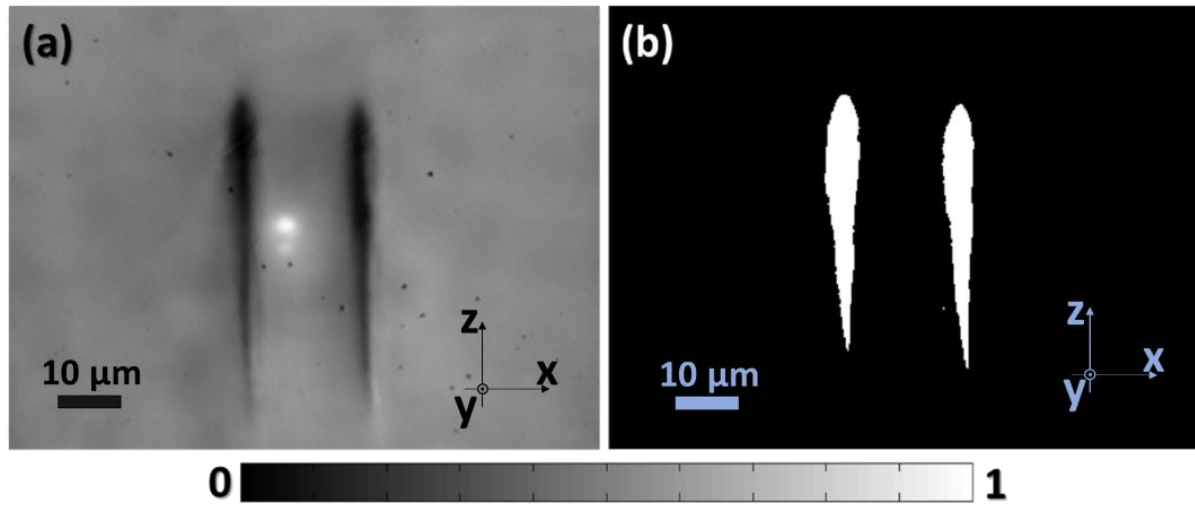


Figure 6-14 : Generating a binary mask of double tracks of WG-1. (a) Intensity image of WG-1; (b) Binary mask of double tracks after post processing. The scale bar represents the normalized intensity based on the maximum intensity values.

The xz -plane intensity image shown in Figure 6-14 (a) is obtained from the OPD measurement of WG-1 in the xz -plane. By using the Igor Pro Image Processing plugin, we can invert, set the threshold and use binary dilation to obtain the binary mask shown in (b). By scaling based on the number of pixels between the tracks and the known distance between the tracks, $20\text{ }\mu\text{m}$, we can determine the average length of the tracks, i.e. thickness that contributes to the phase change, for the waveguides, WG-1, WG-2, WG-3, WG-4 and WG-5, as $40\text{ }\mu\text{m}$, $40\text{ }\mu\text{m}$, $39\text{ }\mu\text{m}$, $28\text{ }\mu\text{m}$ and $32\text{ }\mu\text{m}$, respectively.

6.5.3 3D Refractive Index Change Profile

Once we know the thickness of the structures contributing to the OPD measurement both in the xz -plane and in the xy -plane, it is straight forward to generate the 2D refractive index spatial maps as it is shown in Equation (6.1). As a result, assuming that the refractive index modifications are symmetrical in all dimensions, the refractive index profile in 3D will be the lateral repetition of longitudinal 2D modifications. The 2D xz -plane, longitudinal, refractive

index profile can be generated by blending the lateral refractive index change measurement in the xy -plane along the tracks with the longitudinal refractive index measurements in the vicinity of the tracks in the xz -plane.

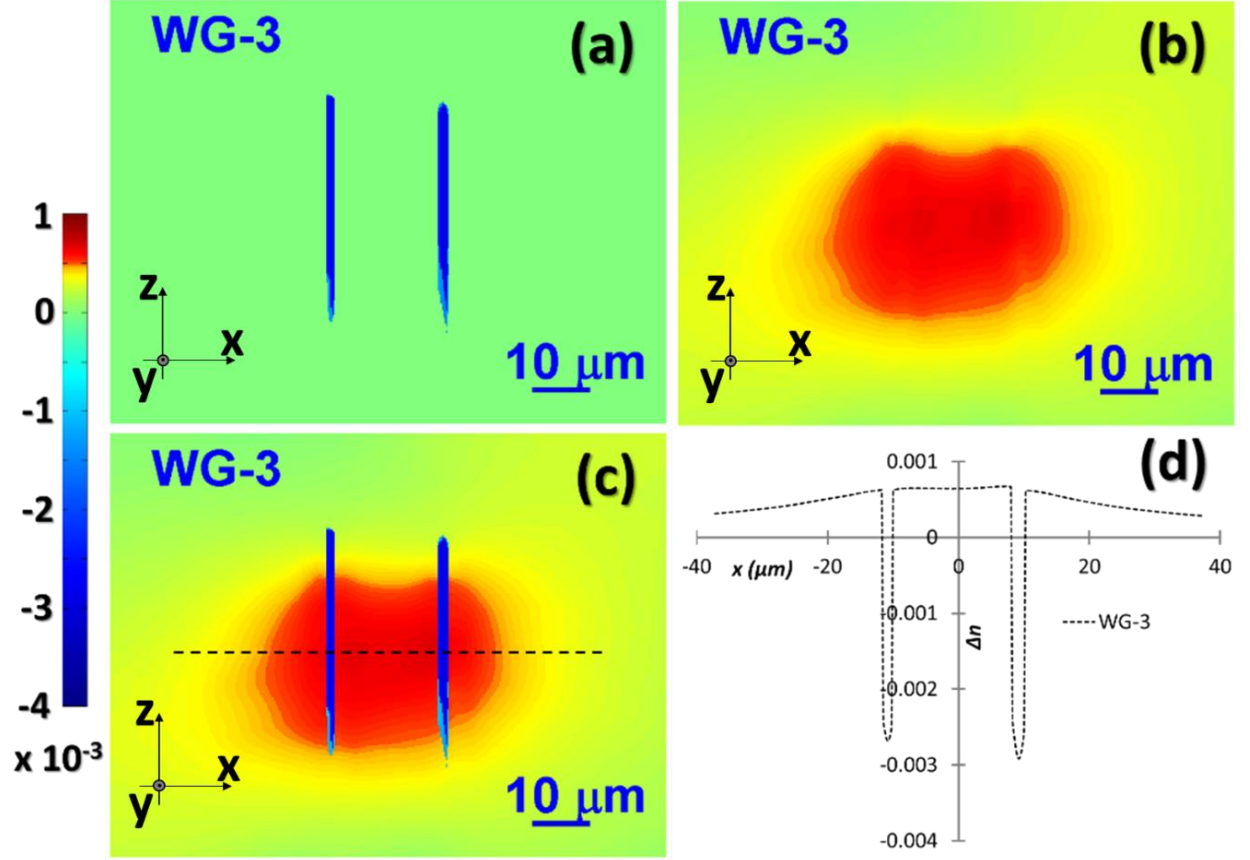


Figure 6-15 : Spatial map of refractive index change (Δn) measurement of WG-3. (a) Spatial map of Δn along the tracks. (b) Spatial map of Δn in the vicinity of the tracks. (c) Spatial map of Δn by blending (a) in to (b). (d) Line profile Δn at the middle of the tracks along the x -axis.

For example, the above Figure 6-15, shows the spatial refractive index change measurement of WG-3. The lateral measurements of negative refractive index change along the tracks are attributed to the longitudinal, xz -plane, binary image of the tracks. Then these results are later blended into the 2D spatial map of Δn in the xz -plane to obtain the total 3D spatial map of Δn .

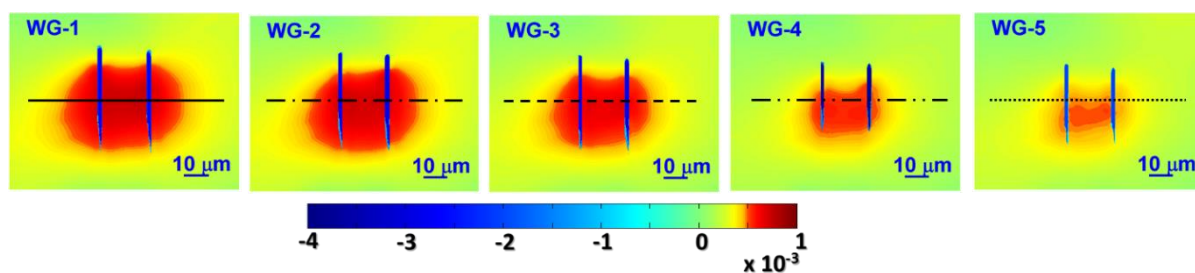


Figure 6-16 : The three-dimensional spatial Δn of all the five waveguides.

As it can be derived from Figure 6-16, the 3D spatial map of Δn for the five waveguides are in the range of values around 10^{-3} in the vicinity of the waveguides to around -4×10^{-3} along the tracks.

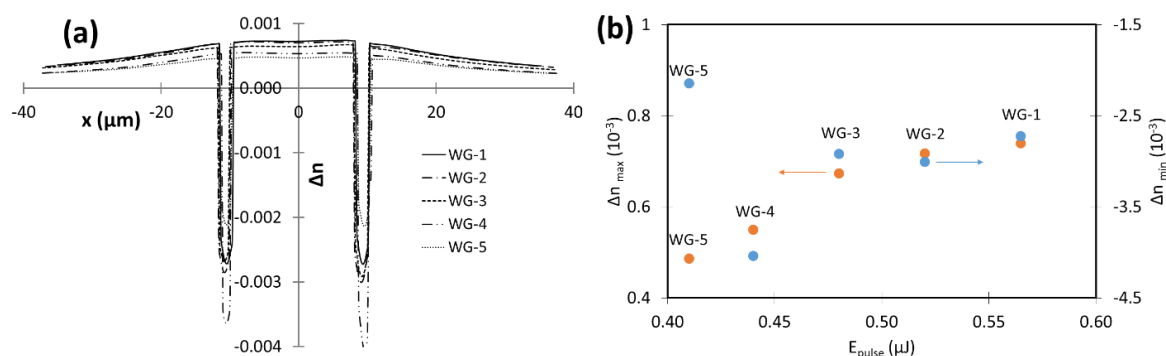


Figure 6-17 : (a) Line profile of Δn for all the waveguides as it is shown in Figure 6-16 above. (b) The minimum and maximum Δn values of the waveguides.

As it can be seen in Figure 6-17 above, the maximum value of Δn increases as the writing energy, E_{pulse} (μJ) increases. While for the minimum Δn , there is no particular trend which indicates that in addition to the writing energy, intrinsic crystallographic modifications play a major role for the negative refractive index change along the tracks.

6.6 Simulation

Once the 3D spatial map of the refractive index is determined, we can simulate the waveguides using FDTD solver to identify the modes that are supported. One of the numerical computation approaches to solve the modes of the waveguides is by using Eigen solutions of the Maxwell's equations [152], [153]. We used Finite Difference Eigenmode (FDE) solver of Lumerical

MODE Solutions, from Lumerical Inc. to calculate the spatial profile of modes on a cross-sectional mesh of the waveguide. In this case, the solver is applied to determine the mode field profiles and effective index.

6.6.1 Method of Simulation

For the given coordinates of the CaF_2 sample shown in Figure 6-3, the Eigenmode solver of propagation along the y-axis can be described as $E(x,y) e^{i(-\omega t + \beta y)}$, where ω is the angular frequency; and β is the propagation constant. The modal effective index, n_{eff} , is then given as:

$$n_{eff} = \frac{c\beta}{\omega} \quad (6.6)$$

Lumerical FDE finds these modes by solving Maxwell's equation on cross-sectional meshes of the waveguide. FDE basically implements a 2D Yee-mesh across the surface of the structures. Once the structures are meshed, the Maxwell's equations are then formulated in to a matrix of eigenvalues. This matrix is then solved by using sparse matrix techniques with some proprietary modifications which are described in [154]. This results the effective index and mode profiles of the waveguides.

Given the determined 3D spatial map of Δn , we can find the 3D refractive index map of the waveguides by simply adding the refractive index of CaF_2 at 632.8 nm, $n = 1.4348$, on each pixel. We have chosen this wavelength because we wanted to compare the simulated modes with the measured mode field diameters of the waveguides for the Helium-Neon laser (HeNe) source. The 3D spatial distributions of refractive index are then imported using Import object for (n,k) data tool in the Lumerical software.

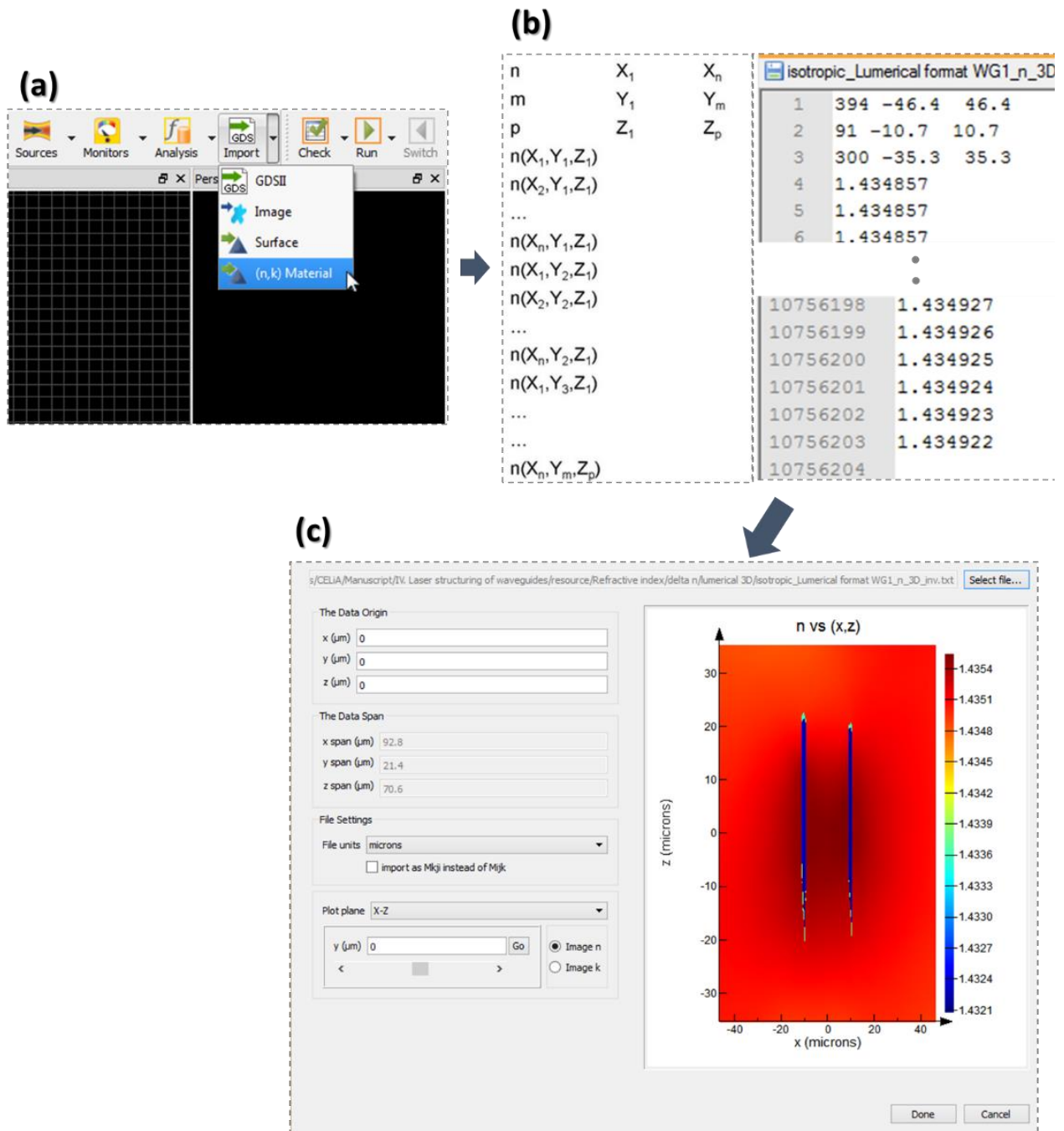


Figure 6-18 : Importing the 3D spatial map of waveguides for simulation using Mode Solutions of Lumerical Inc. (a) screenshot of the (n,k) material import wizard; (b) File format for isotropic material and on the left example for WG-1; and (c) Index monitor to view the imported material (in this case for WG-1).

Figure 6-18 shows the import GUI for the 3D refractive index distribution of the waveguides. In this case, as shown in (b) and (c), the refractive index profile of WG-1 is considered. After the 3D Δn spatial map is imported, we use the Eigensolver Analysis to solve the mode of the waveguides. For example, we calculated the first five TE modes of WG-1. Then, an overlap

with the circular Gaussian source at 633 nm with a waist of $7.5\ \mu\text{m}$, as it was shown in the waveguiding experiment, was performed.

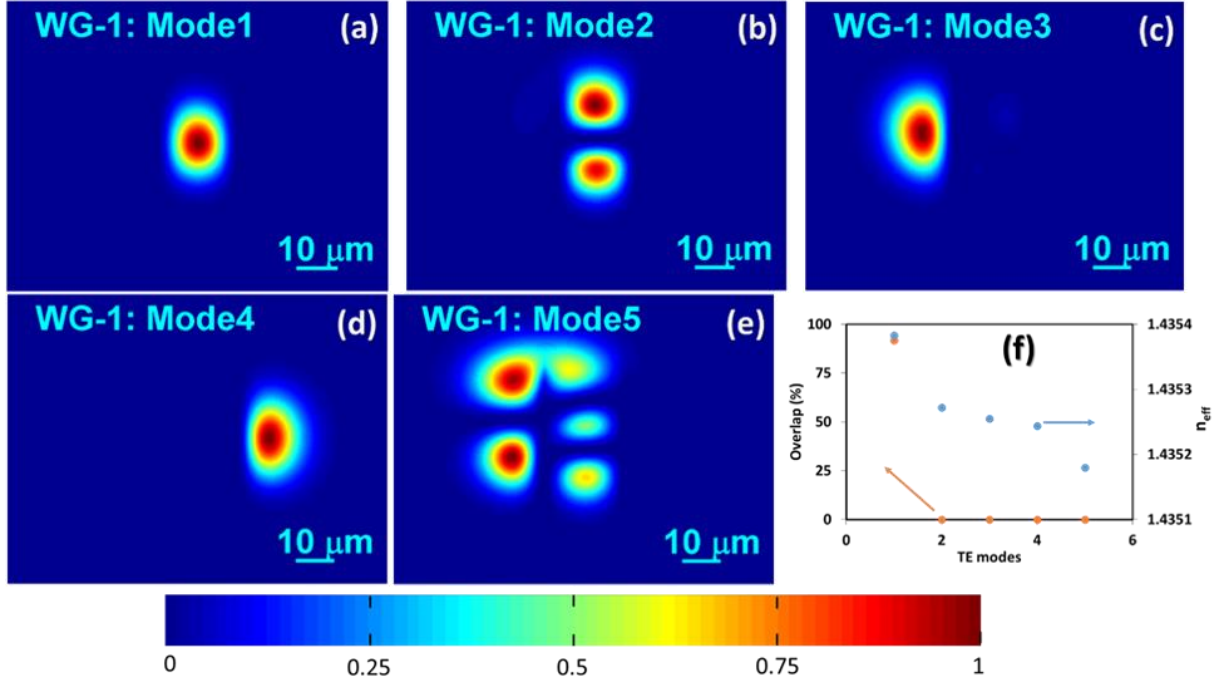


Figure 6-19 : (a) - (e) show the first five TE modes of WG-1 determined by simulation. (f) shows the plot of overlap between the assumed HeNe source at 633 nm with a waist of $7.5\ \mu\text{m}$, and the effective refractive index of the five TE modes of WG-1.

As it is shown in Figure 6-19 above, the overlap between the fundamental mode and the assumed HeNe source at 633 nm is 91 % while it is less than 1 % for the consecutive four TE modes. Given the fact that the Eigenmode simulation is on a single 2D-layer and the beam expands after injection and good numerical aperture matching between the mode and the injected beam, we can reasonably assume that the overlap is even more than 91 %. As it can be observed, we can conclude that the excited mode for our given source is gaussian.

6.6.2 Comparison between Experiment and Simulation of Guided Modes

Since it was shown in the previous section that the fundamental mode of the simulation is a gaussian mode which is also true for our experiments, we simulated the waveguides and consider the power density distribution of the fundamental modes for all the five waveguides.

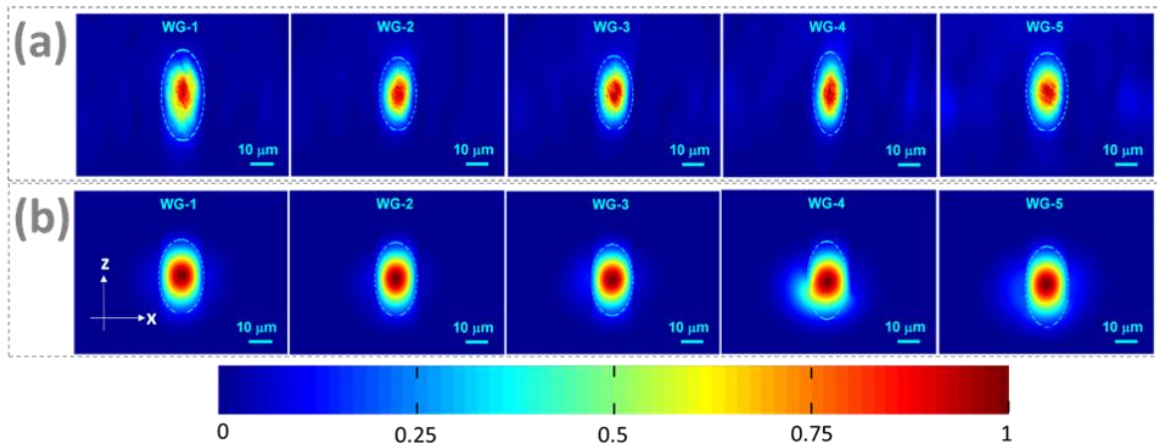
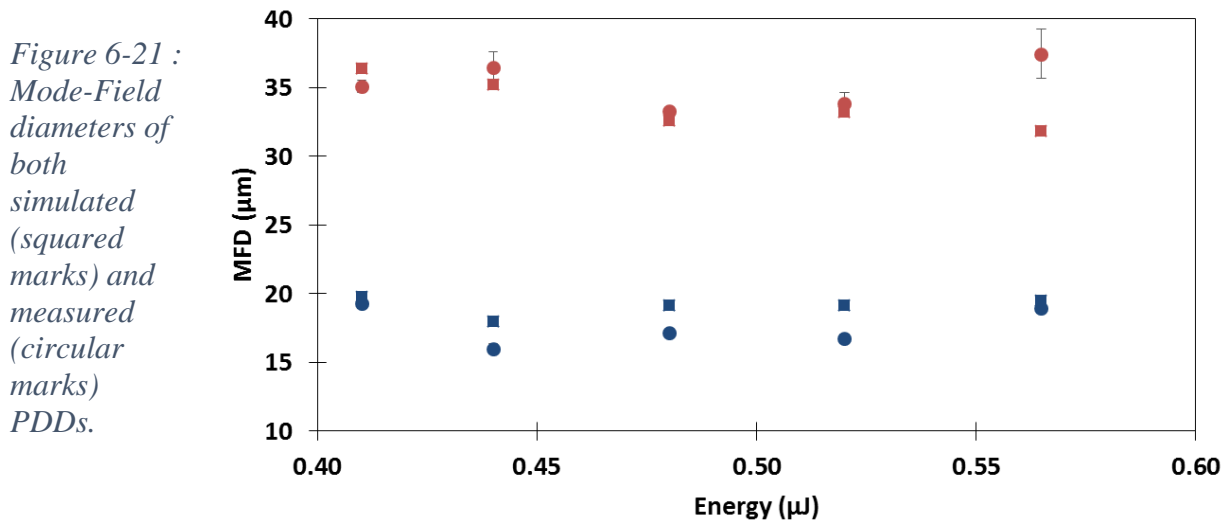


Figure 6-20 : Fundamental power density distribution (PDD) of both simulated (a) and experimental (b) profiles of all the five waveguides.

As shown in Figure 6-20, we have observed a high similarity between the fundamental mode of the simulated results and the guided modes from our waveguiding experiment. The MFD of both the simulated and experimental results are calculated.



It can be observed from the simulated results that there are backgrounds which look like leaking modes. Assuming these result from the weak refractive index change and weakly guided mode, to identify the MFD of the simulated fundamental modes, we used the mode from the longitudinal refractive index change profile without the tracks as the profile of the background weakly guided mode. Thus, by subtracting the weakly guided mode from the total simulated

mode, we were able to get MFD values very close to the experimental results as shown in Figure 6-21.

Table 6-3 : Simulated results of the effective refractive index (n_{eff}) of all the five waveguides for fundamental modes. The third row shows the effective numerical aperture (NA_{eff}) that should be considered. The last row shows the overlap between the source and the fundamental modes.

Waveguide	WG-1	WG-2	WG-3	WG-4	WG-5
$E_{pulse} (\mu J)$	0.56	0.52	0.48	0.44	0.41
n_{eff}	1.435383	1.435369	1.435314	1.435228	1.43518
NA_{eff}	0.041	0.040	0.038	0.035	0.033
<i>Overlap (%)</i>	91.8	90.3	90.7	85.5	84.3

Furthermore, we calculated the effective refractive indices of the fundamental modes of the five waveguides as shown in Table 6-3. The effective numerical aperture ranges between 0.041, for WG-1, to 0.033, for WG-5. In our experiment, the injection objective had a numerical aperture of 0.13 and a rear aperture of 12 mm, while the beam had a diameter around 2.8 mm. This results in 0.03 for the NA of the injected beam. Since the value of the calculated effective NA (NA_{eff}) of the waveguides is greater than this value, we must have attained an almost “perfect” mode matching and coupling efficiency and that most of the unguided mode should be the result of mismatch between the ellipticity of the PDD of the guided mode and the injected source which is not explainable by considering only a single equivalent value like an effective refractive index, n_{eff} , and the error due to micrometer level control of the injection optics.

It is also shown that the overlap integral between the source and the fundamental mode of the simulated mode result shows that the overlap is at least 85 % which proves that the guided

modes in both, waveguide and transmission loss experiments, are gaussian modes for all the waveguides.

6.7 Conclusions

Until this point, several attempts have been made and determining the refractive index change of ultrafast laser modified waveguides inside crystals has been a big challenge. In this chapter, we have presented a new approach for the refractive index change measurement and provided a very accurate experimental evidence to it. In conclusion, it is impressive that using a direct refractive index measurement technique, which involves the Fresnel number determination approach demonstrated, we can get a high-resolution complete refractive index map of the micro-sized waveguides which otherwise would have required expensive and difficult polishing of the samples down to tens of micrometers in thickness.

7 Conclusion and Future Work

In conclusion, we presented a photonic device fabrication technique by using a femtosecond laser writing setup. Once again, this technique had proven to be simple and effective for the miniaturization of optical components to pave the way to smaller on-chip solutions. Most of the work in this thesis is dedicated to femtosecond inscription of double track waveguides inside CaF_2 crystals and their qualitative and quantitative characterization. A thorough description of the characterization methods is given as well.

Along with the double-track waveguide inscriptions inside those CaF_2 crystals, smooth modification and non-reciprocal writing were observed. Additionally, the process window for these types of modifications is systematically identified concerning the writing parameters and crystallographic orientations. In Chapter 5, the simplified model of linearly polarized light coupling into the waveguide was employed and implemented to find an upper limit of the transmission losses. These estimations were calculated to be between 1.9 dB/cm and 2.7 dB/cm, which are comparable with the propagation properties of double-track waveguides in similar laser crystals.

In Chapter 6, an elegant method for the determination of the three-dimensional refractive index modification, Δn , spatial map along and in the vicinity of the double-track waveguides is shown. A special type of phase contrast microscopy, QWLSI, was used to obtain the detailed OPD map of the waveguides. This was coupled with a hands-on analytical approach for determining the thickness of the elements and resulting in a detailed three-dimensional Δn spatial map with values that are in the order of 10^{-3} . These results were confirmed by the similarity of an Eigenmode simulation and experimentally guided fundamental modes.

Finally, it can be concluded that both experimental and analytical approaches demonstrated in this work can be further refined to obtain highly effective waveguides, and the methodologies can be considered as benchmarks for further simplified hands-on characterization of waveguides written inside crystals if not bulk materials in general.

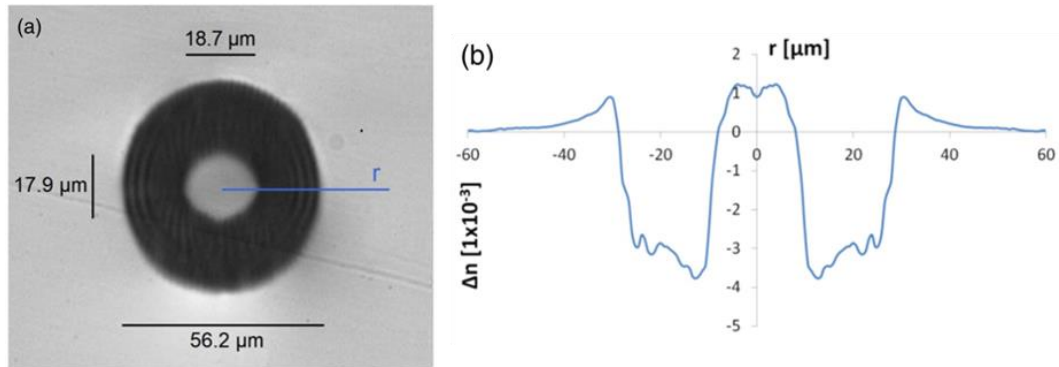


Figure 7-1: (a) Image of the cross section and (b) radial refractive index profile of a depressed cladding waveguide inscribed in sapphire. The profile is computed along the solid blue line, and data are plotted symmetrically on both sides of the central axis. (copied from [155])

For example, Figure 7-1 shows a recent work by J. Bérubé et al. which is a depressed cladding single-mode mid-infrared waveguide in sapphire with highly efficient coupling and propagation losses of as low as 0.37 dB/cm thanks to highly symmetrical, uniform, and homogeneous waveguides with smooth negative refractive index change. This is similar to the case of smooth modification inside CaF_2 crystals which was discussed in Chapter 4 and can be implemented to inscribe efficient low loss depressed claddings.

Appendix A

In addition to double track waveguides inside CaF_2 , we have also performed double track waveguides inside Nd:YAG as a proof of concept. This work was presented in the Proceedings of the 41st International Conference on Advanced Ceramics and Composites: Ceramic Engineering and Science Proceedings, Volume 38, Issue 3, Volume 38 (2018) and is cited below.

CHARACTERIZATION APPROACHES OF FEMTOSECOND DIRECT LASER WRITING (DLW) MODIFICATIONS INSIDE CUBIC YAG CRYSTALS

W. Gebremichael^{1,2}, I. Manek-Hönniger¹, S. Rouzet¹, M. Chamoun¹, A. Fargues², V. Jubera⁵, T. Cardinal⁵, Y. Petit^{1,5}, L. Canioni¹

¹ Centre Lasers Intenses et Applications (CELIA - University of Bordeaux-CNRS-CEA UMR5107), Talence, France

² Amplitude Systèmes, Cité de la Photonique, 11 Avenue de Canteranne, 33600 Pessac

⁵ Institut de Chimie de la Matière Condensée de Bordeaux (ICMCB-CNRS-UPR9048), Pessac, France

ABSTRACT

This study is focused on direct laser writing (DLW) of waveguides inside cubic $\text{Y}_3\text{Al}_5\text{O}_{12}$ (YAG) crystals doped with Nd^{3+} and their characterization. We show a mode-field analysis at 633 nm for different double track waveguides and first results on gain measurements at 1064 nm and compare the result with free propagation in the bulk material.

INTRODUCTION

Recent developments in femtosecond DLW allow for realizing a vast range of photonic devices which is a driving force behind industrial interest for rapid prototyping of optical components. Thus, it is necessary to have a better understanding and approach for qualitative and quantitative characterizations in both waveguide and luminescence properties of modified transparent materials. Yttrium aluminium garnet (YAG) is a common crystal widely used as gain medium in solid state lasers. Owing to its crystallographic structure, optical specificities and restrictions of low-symmetry crystal optics are neglected which enables a simple systematic approach to study modifications due to femtosecond DLW inside crystals along the damaged tracks.

Waveguides based on a permanent refractive index modification by femtosecond lasers were first inscribed in glasses [1], and later also in crystalline optical materials like silicon [2]. Doped YAG crystals have been used for waveguide inscription by DLW and waveguide laser demonstration [3-5], even with curved forms of waveguides showing a slope efficiency of 79 % [6]. DLW waveguides and waveguide lasers in rare earth doped YAG ceramics are also reported for different active ions like Neodymium [7-9] and Ytterbium [10] for laser operation at 1 μm , and with Holmium, Erbium [11] and Thulium [12] for lasers in the mid-infrared.

In glasses, the refractive index is typically increased along the damage line, and the guiding of the light takes place within the damage track. However, in crystals, the refractive index is usually lowered, demanding more complex structures for guiding between damage tracks. The simplest form of a waveguide consists of double lines forming a channel where the light is guided between the two writing tracks. A study of the refractive index change mechanisms by DLW in Nd:YAG ceramic waveguides can be found in [13]. Reference [14] gives a very nice review on optical waveguides in crystals describing the writing mechanism and giving an exhaustive overview over the different crystalline materials.

SAMPLE PREPARATION

A rectangular piece with the dimensions of 11.3 mm x 9.0 mm x 0.9 mm of Nd:YAG (doped at 0.8 % wt.) was cut out of a standard laser rod with the original dimensions of 100 mm length and 16.5 mm diameter and was then polished to optical quality. A femtosecond laser beam (see Fig. 1) at 800 nm with an energy of 0.63 mJ delivered by a commercial Ti:Sapphire amplifier system (RegA, Coherent) is focused by a microscope objective with NA = 0.9 focusing at 100 μm mechanically below the crystal surface, and thus leading to a focal point at 184 μm underneath the crystal surface taking into account the refractive index of around 1.8 of the material. Due to the elongated form of the focalized laser beam, the damage tracks are elliptical as can be easily understood from Fig. 1.

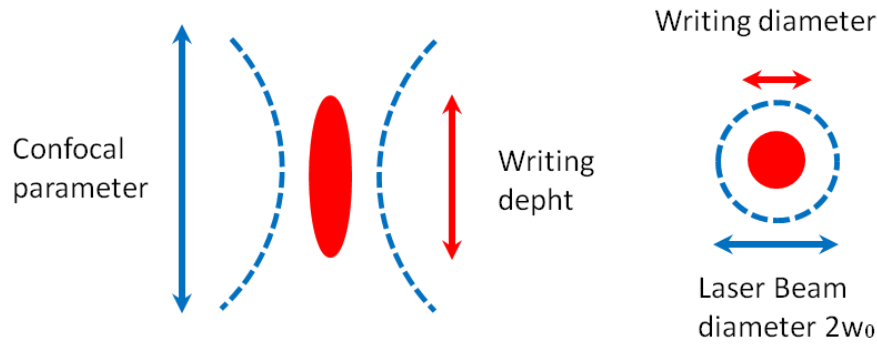


Figure 1. Schematic drawing of the laser beam for DLW on the Nd:YAG crystal.

The sample was translated perpendicularly to the laser beam with a translation speed of $v=10 \mu\text{m/s}$ writing speed. All DLW parameters that were applied in this experiment are summarized in Table 1.

Table 1. Laser source, beam parameters and writing parameters for waveguide writing in Nd:YAG.

Laser source parameters		Writing parameters		Beam parameters	
Wavelength	$\lambda = 800 \text{ nm}$	Speed	$v = 10 \mu\text{m/s}$	Beam waist	$w_0 = 0.97 \mu\text{m}$
Energy	$E = 0.63 \mu\text{J}$	# of pulses	$N = 48\,570$	Rayleigh range	$z_R = 3.7 \mu\text{m}$
Pulse duration	$\tau = 150 \text{ fs}$			Irradiance	$I = 226 \text{ TW/cm}^2$
Repetition rate	$f = 250 \text{ kHz}$	Objective	$\text{NA} = 0.9$	Energy deposition	$E_{\text{dep}} \sim 30.6 \text{ mJ}$

We chose to write 3 different series consisting each of three equal double lines forming each pair of tracks a waveguide channel. We opted for 3 series of double tracks with a distance between the lines of $10 \mu\text{m}$, $20 \mu\text{m}$ and $25 \mu\text{m}$, respectively. The distance between two double tracks of the same series was $200 \mu\text{m}$ which should be sufficiently large to avoid cross talking between the different waveguide channels. The distance between two series was chosen to be $350 \mu\text{m}$ in order to easily distinguish between two different series. The resulting double track waveguides are schematically illustrated in Fig. 2 showing a top view (a) and a side view (b).

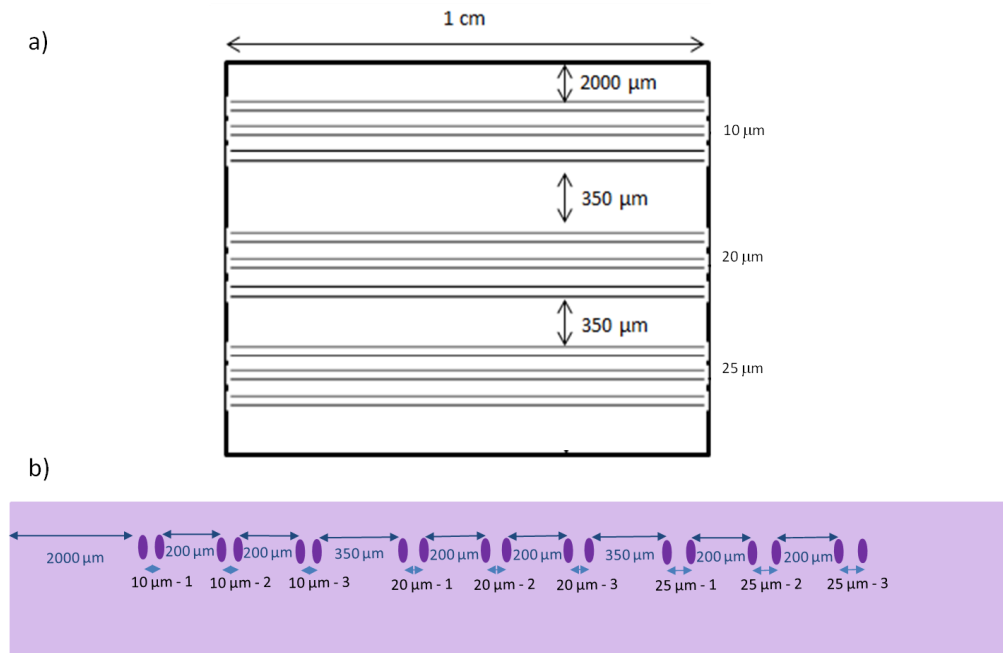


Figure 2. Schematic view seen from the top (a) and from the side (b) of the DLW structured Nd:YAG crystal.

GUIDING PROPERTIES

In order to study the guiding properties of the double tracks, we injected a HeNe laser beam at 633 nm using a microscope objective of x20 with an NA of 0.5 into the waveguides. The transmitted beam was imaged on a CCD camera (Thorlabs, BC106N-VIS/M) using exactly the same type of objective. The objectives and the sample were mounted on a three axes translation stage allowing for accurate injection into the waveguides and good and reproducible alignment.

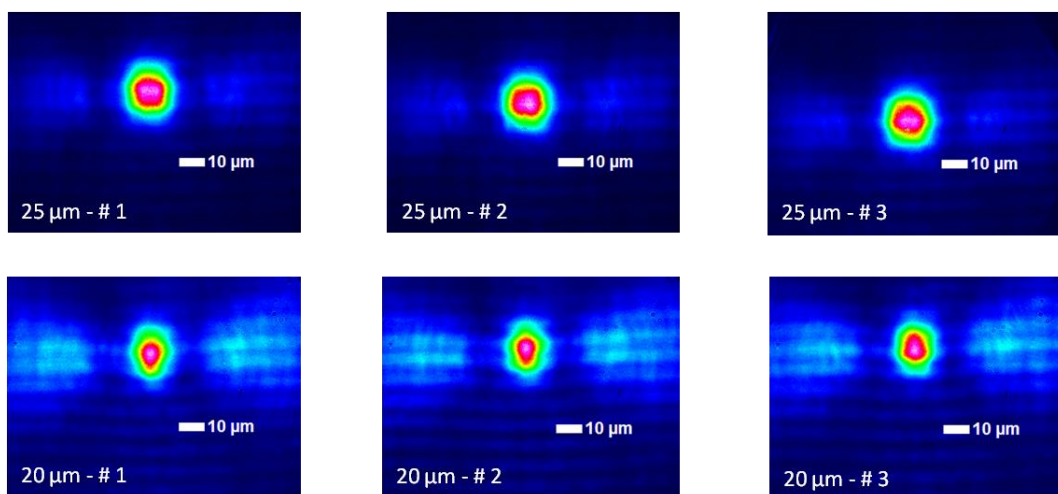


Figure 3. Images of the beam profile of the guided modes in the 25 μm double tracks (upper row) and in the 20 μm double tracks (lower row) taken with a CCD camera, respectively.

As can be seen on Fig. 3, we obtained good guiding with Gaussian beam profiles for the 25 μm and 20 μm double tracks, however with some small side lobes in the x direction, especially in the case of the 20 μm waveguide channels. We observed no guiding in the 10 μm double tracks due to a too high numerical aperture of the microscope objective. This can be overcome by using a lens for focusing the injected beam.

We studied furthermore the polarization dependence of the waveguides. Therefore, we turned the polarization by a half wave-plate just before injection into the waveguides. The results are depicted in Fig. 4 for the 20 μm and 25 μm double tracks and show a Malus law behavior with a maximum transmission corresponding to s-polarized light. The minimum transmission for p-polarized light is on the order of 20 %. Further work is needed to identify if these 20% truly result from the p-polarized transmission of the waveguide, or if it results from non-spatially filtered light not being guided but still collected after free propagation since (i) the waveguides were not so long and (ii) the numerical aperture of the injecting objective was visibly higher than that of the waveguiding structures. Still, our double track waveguides are likely to be stress-induced corresponding to their polarization-selective behavior.

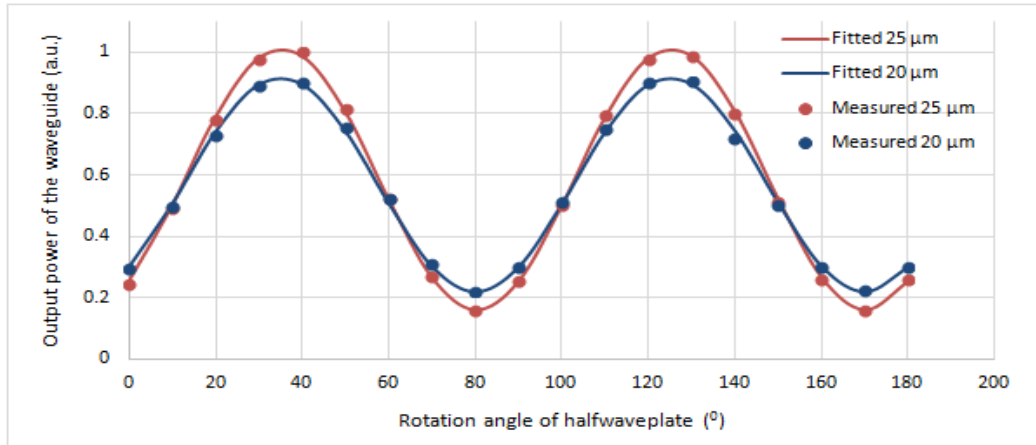


Figure 4. Transmitted output power of the waveguide as a function of the rotation angle of the halfwave-plate.

GAIN MEASUREMENTS

In order to compare the amplification potential within the waveguides with respect to ordinary bulk propagation, we performed gain measurements. Therefore, we injected a pump beam around 808 nm, corresponding an absorption maximum of Nd:YAG, delivered by a Ti:Sapphire laser (Cameleon, Coherent) into the sample. We carefully mode-matched a signal beam at 1064 nm delivered by a diode-pumped microchip laser (Teemphotonics) and overlapped the two laser beams for single-pass injection. The gain was measured for different pump power and signal power levels for all three waveguide series and for non guided free propagation in the bulk. The injected seed power was 0.07 mW, 0.21 mW, 0.66 mW and 1.08 mW, respectively, whereas the pump power was varied up to 750 mW. Using a lens of focal

length $l' = 75$ mm for injection allowed us to have a better coupling efficiency, and especially to be able to inject into the 10 μm double tracks. In fact, considering the Fresnel losses of 8.8% per face, the measured coupling efficiencies of the pump / seed were 88% / 76%, 73% / 58% and 27% / 19% for the 25 μm , 20 μm and 10 μm waveguide channels, respectively.

Fig. 5 depicts the single-pass gain as a function of the injected pump power for the three different waveguide channels and for bulk propagation. It is clearly visible that the smaller the waveguide the higher the gain. For the 25 μm double tracks the gain is still comparable to the bulk propagation and no advantage of waveguide propagation is visible.

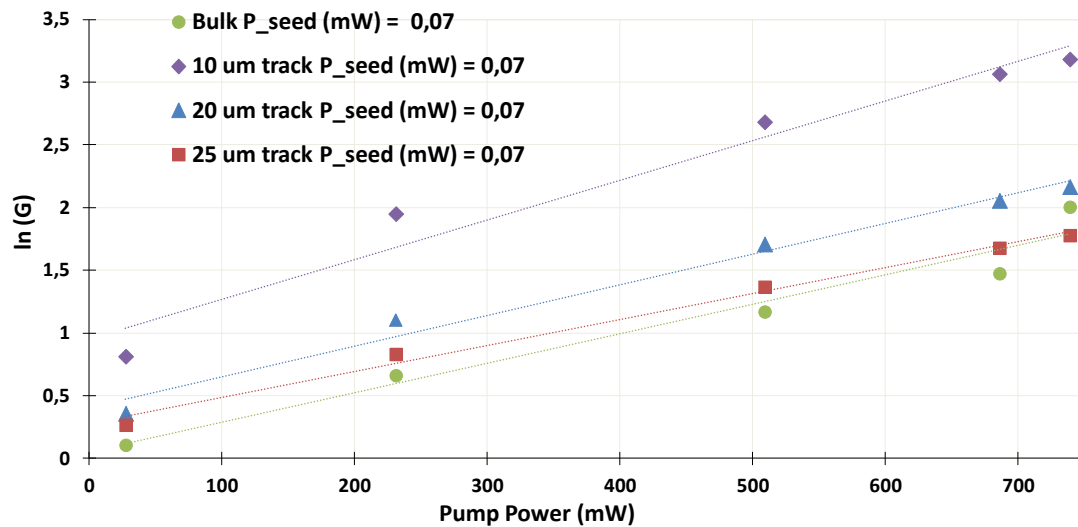


Figure 5. Single-pass gain as a function of injected pump power for the three different waveguide channel series and bulk propagation in comparison; the injected seed power at 1064 nm was $P_{\text{seed}} = 0.07$ mW.

CONCLUSION AND PERSPECTIVES

We have successfully written double track waveguides by direct femtosecond laser writing into a Neodymium-doped YAG crystal. The guided modes are Gaussian in both x and y direction. However, some side lobes are visible in the x direction due to leakage but can be filtered out easily. Moreover, the waveguides are polarization sensitive and mainly guide s-polarized light. We furthermore studied the gain properties at 1064 nm using a pump centered at 808 nm for different levels of seed and pump. Under the same conditions, the 10 μm double tracks show the best gain properties compared to the bigger double tracks or the non guided gain in the same bulk material.

ACKNOWLEDGEMENTS

This study has been carried out with financial support from the French State, managed by the French National Research Agency (ANR) in the frame of “the Investments for the future” Programme IdEx Bordeaux – LAPHIA (ANR-10-IDEX-03-02).

REFERENCES

- ¹ K.M. Davis, K. Miura, N. Sugimoto, and K. Hirao, “Writing waveguides in glass with a femtosecond laser,” *Opt. Lett.* vol. 21 (no. 21), pp. 1729-1731 (1996).
- ² A.H. Nejadmalayeri, P. Herman, J. Burghoff, M. Will, S. Nolte, and A. Tünnermann, “Inscription of optical waveguides in crystalline silicon by mid-infrared femtosecond laser pulses,” *Opt. Lett.* Vol. 30 (no. 9), pp. 964-966 (2005).
- ³ J. Siebenmorgen, K. Petermann, G. Huber, K. Rademaker, S. Nolte, A. Tünnermann, “Femtosecond laser written stress-induced Nd:Y₃Al₅O₁₂ (Nd:YAG) channel waveguide laser,” *Appl. Phys. B* 97, pp. 251-255 (2009).
- ⁴ J. Siebenmorgen, T. Calmano, K. Petermann, and G. Huber, “Highly efficient Yb:YAG channel waveguide laser written with a femtosecond-laser,” *Opt. Express*, vol. 18, no. 15, pp. 16035–16041 (2010).
- ⁵ T. Calmano, J. Siebenmorgen, O. Hellmig, K. Petermann, and G. Huber, “Nd:YAG waveguide laser with 1.3 W output power, fabricated by direct femtosecond laser writing,” *Appl. Phys. B*, vol. 100, no. 1, pp. 131–135 (2010).
- ⁶ T. Calmano, A.-G. Paschke, S. Müller, C. Kränkel, and G. Huber, “Curved Yb:YAG waveguide lasers, fabricated by femtosecond laser inscription,” *Opt. Express*, vol. 21, no. 21, pp. 25501–25508 (2013).
- ⁷ G. A. Torchia, A. Ródenas, A. Benayas, E. Cantelar, L. Rosso, and D. Jaque, “High efficient laser action in femtosecond-written Nd:yttrium aluminium garnet ceramic waveguides”, *Appl. Phys. Lett.*, vol. 92, 111103 (2008).
- ⁸ A. Ródenas, G. Zhou, D. Jaque, and M. Gu, “Direct laser writing of three-dimensional photonic structures in Nd:yttrium aluminium garnet ceramics”, *Appl. Phys. Lett.*, vol. 93, 151104 (2008).
- ⁹ H. Liu, Y. Jia, J.R. Vazquez de Aldana, D. Jaque, and F. Chen, “Femtosecond laser inscribed cladding waveguides in Nd:YAG ceramics: Fabrication, fluorescence imaging and laser performance”, *Opt. Express*, vol. 20, no. 17, pp. 18620-18628 (2012).
- ¹⁰ T. Calmano, A. G. Paschke, J. Siebenmorgen, S. T. Fredrich-Thornton, H. Yagi, K. Petermann, and G. Huber, “Characterization of an Yb:YAG ceramic waveguide laser, fabricated by the direct femtosecond-laser writing technique,” *Appl. Phys. B*, vol. 103, no. 1, pp. 1–4 (2011).
- ¹¹ A. Ródenas, A. Benayas, J.R. Macdonald, J. Zhang, D.Y. Tang, D. Jaque, and A.K. Kar, “Direct laser writing of near-IR step-index buried channel waveguides in rare earth doped YAG”, *Opt. Lett.*, vol. 36, pp. 3395-3397 (2011).
- ¹² Y. Ren, G. Brown, A. Rodenas, S. Beecher, F. Chen, and A.K. Kar, “Mid-infrared waveguide lasers in rare-earth-doped YAG”, *Opt. Lett.*, vol. 37, pp. 3339-3341 (2012).
- ¹³ A. Ródenas, G. A. Torchia, G. Lifante, E. Cantelar, J. Lamela, F. Jaque, L. Roso, and D. Jaque, “Refractive index change mechanisms in femtosecond laser written ceramic Nd:YAG waveguides: Micro-spectroscopy experiments and beam propagation calculations,” *Appl. Phys. B*, vol. 95, no. 1, pp. 85–96 (2009).

¹⁴ F. Cheng and J.R. Vazquez, "Optical waveguides in crystalline dielectric materials produced by femtosecond-laser micromachining", *Laser & Photonics Reviews*, vol. 8, no. 2, pp. 251-275 (2014).

Bibliography

- [1] K. O. Hill, Y. Fujii, D. C. Johnson, and B. S. Kawasaki, “Photosensitivity in optical fiber waveguides: Application to reflection filter fabrication,” *Appl. Phys. Lett.*, vol. 32, no. 10, pp. 647–649, 1978.
- [2] K. M. Davis, K. Miura, N. Sugimoto, and K. Hirao, “Writing waveguides in glass with a femtosecond laser,” *Opt. Lett.*, vol. 21, no. 21, p. 1729, Nov. 1996.
- [3] K. Sugioka and Y. Cheng, “Ultrafast lasers—reliable tools for advanced materials processing,” *Light Sci. Appl.*, vol. 3, no. 4, pp. e149–e149, Apr. 2014.
- [4] G. Della Valle, R. Osellame, and P. Laporta, “Micromachining of photonic devices by femtosecond laser pulses,” *J. Opt. A Pure Appl. Opt.*, vol. 11, no. 1, p. 013001, Jan. 2009.
- [5] M. Malinauskas *et al.*, “Ultrafast laser processing of materials: from science to industry,” *Light Sci. Appl.*, vol. 5, no. 8, p. e16133, 2016.
- [6] S. Engelhardt, “Direct Laser Writing BT - Laser Technology in Biomimetics: Basics and Applications,” V. Schmidt and M. R. Belegatis, Eds. Berlin, Heidelberg: Springer Berlin Heidelberg, 2013, pp. 13–65.
- [7] S. C. Jones, P. Braunlich, R. T. Casper, X.-A. Shen, and P. Kelly, “Recent Progress On Laser-Induced Modifications And Intrinsic Bulk Damage Of Wide-Gap Optical

- Materials,” *Opt. Eng.*, vol. 28, no. 10, p. 281039, 1989.
- [8] S. M. Eaton, G. Cerullo, and R. Osellame, “Fundamentals of femtosecond laser modification of bulk dielectrics,” *Top. Appl. Phys.*, vol. 123, pp. 3–18, 2012.
- [9] R. R. Gattass and E. Mazur, “Femtosecond laser micromachining in transparent materials,” *Nat. Photonics*, vol. 2, no. 4, pp. 219–225, 2008.
- [10] R. Osellame, G. Cerullo, and R. Ramponi, *Femtosecond Laser Micromachining*. Milano, Italy: Springer US, 2012.
- [11] A. G. Okhrimchuk and P. A. Obraztsov, “11-GHz waveguide Nd:YAG laser CW mode-locked with single-layer graphene,” *Sci. Rep.*, vol. 5, no. 1, p. 11172, 2015.
- [12] W. Koechner, *Solid-State Laser Engineering - 6th Edition*. 2014.
- [13] M. Siebold *et al.*, “Yb:CaF₂ — a new old laser crystal,” *Appl. Phys. B*, vol. 97, no. 2, pp. 327–338, Oct. 2009.
- [14] S. S. Mao *et al.*, “Dynamics of femtosecond laser interactions with dielectrics,” *Appl. Phys. A*, vol. 79, no. 7, pp. 1695–1709, Nov. 2004.
- [15] A. Royon, Y. Petit, G. Papon, M. Richardson, and L. Canioni, “Femtosecond laser induced photochemistry in materials tailored with photosensitive agents [Invited],” *Opt. Mater. Express*, vol. 1, no. 5, p. 866, Sep. 2011.
- [16] F. Chen and J. R. V. de Aldana, “Optical waveguides in crystalline dielectric materials

-
- produced by femtosecond-laser micromachining,” *Laser Photon. Rev.*, vol. 8, no. 2, pp. 251–275, Mar. 2014.
- [17] G. Agrawal, “Pulse Propagation in Fibers,” in *Nonlinear Fiber Optics*, G. B. T.-N. F. O. (Fifth E. Agrawal, Ed. Boston: Elsevier, 2013, pp. 27–56.
- [18] J. H. Marburger, “Self-focusing: Theory,” *Prog. Quantum Electron.*, vol. 4, pp. 35–110, 1975.
- [19] M. D. Feit and J. A. Fleck, “Effect of refraction on spot-size dependence of laser-induced breakdown,” *Appl. Phys. Lett.*, vol. 24, no. 4, pp. 169–172, Feb. 1974.
- [20] W. Theobald *et al.*, “Electron densities, temperatures, and the dielectric function of femtosecond-laser-produced plasmas,” *Phys. Rev. E - Stat. Physics, Plasmas, Fluids, Relat. Interdiscip. Top.*, vol. 59, no. 3, pp. 3544–3553, 1999.
- [21] P. G. Kazansky, W. Yang, E. Bricchi, J. Bovatsek, and A. Arai, “‘Quill’ writing with ultrashort light pulses in transparent optical materials,” *Conf. Lasers Electro-Optics, 2007, CLEO 2007*, pp. 2007–2009, 2007.
- [22] C. B. Schaffer, A. Brodeur, and E. Mazur, “Laser-induced breakdown and damage in bulk transparent materials induced by tightly focused femtosecond laser pulses,” *Meas. Sci. Technol.*, vol. 12, no. 11, pp. 1784–1794, Nov. 2001.
- [23] A. Couairon and A. Mysyrowicz, “Femtosecond filamentation in transparent media,” *Phys. Rep.*, vol. 441, no. 2, pp. 47–189, 2007.
- [24] H. Search, C. Journals, A. Contact, M. Iopscience, and I. P. Address, “Strong-field atomic stabilization : numerical,” vol. 125, 2003.

- [25] I. Shchatsinin, “Free Clusters and Free Molecules in Strong , Shaped Laser Fields,” 2009.
- [26] A. Fuerbach *et al.*, “Refractive index change mechanisms in different glasses induced by femtosecond laser irradiation,” in *Proc. SPIE 9983, Pacific Rim Laser Damage*, 2016, p. 99830W.
- [27] C. Pan, C. Lin, C. Yang, C. Lin, and C. Yang, “Laser Laser Ablation Ablation of of Polymethylmethacrylate Polymethylmethacrylate (PMMA) (PMMA) by by Phase-Controlled Femtosecond Two-Color Synthesized Phase-Controlled Femtosecond Two-Color Synthesized Waveforms Waveforms,” in *Applications of Laser Ablation - Thin Film Deposition, Nanomaterial Synthesis and Surface Modification*, 2016, pp. 335–358.
- [28] L. V. Keldysh, “Ionization in the field of a string electromagnetic wave,” *J. Exp. Theor. Phys.*, vol. 20, no. 5, pp. 1307–1314, 1965.
- [29] N. B. Delone, *Basics of interaction of laser radiation with matter*, 1st ed. Gif-sur-Yvette, France: Frontières, 1993.
- [30] B. C. Stuart, M. D. Feit, S. Herman, A. M. Rubenchik, B. W. Shore, and M. D. Perry, “Nanosecond-to-femtosecond laser-induced breakdown in dielectrics,” *Phys. Rev. B*, vol. 53, no. 4, pp. 1749–1761, 1996.
- [31] I. Langmuir, “Oscillations in Ionized Gases,” *Phys. Rev.*, pp. 627–637, 1928.
- [32] M. Lebugle, N. Sanner, S. Pierrot, and O. Utéza, “Absorption dynamics of a femtosecond laser pulse at the surface of dielectrics,” in *AIP Conference Proceedings*, 2012, vol. 1464, pp. 91–101.

-
- [33] N. Varkentina, O. Utéza, B. Chimier, N. Sanner, M. Sentis, and T. Itina, “Femtosecond laser pulse absorption by dielectrics: Surface experiments and modelling,” in *EDP Sciences*, 2011, vol. 2010, pp. 233–237.
- [34] M. Lebugle, N. Sanner, R. Clady, D. Grojo, O. Uteza, and M. Sentis, “Femtosecond laser pulse absorption at the surface of dielectrics,” in *2013 Conference on Lasers & Electro-Optics Europe & International Quantum Electronics Conference CLEO EUROPE/IQEC*, 2013, pp. 1–1.
- [35] M. Lenzner *et al.*, “Femtosecond optical breakdown in dielectrics,” *Phys. Rev. Lett.*, vol. 80, no. 18, pp. 4076–4079, 1998.
- [36] D. M. Krol, “Femtosecond laser modification of glass,” *J. Non. Cryst. Solids*, vol. 354, no. 2–9, pp. 416–424, Jan. 2008.
- [37] B. Rethfeld, “Free-Electron Generation in Laser-Irradiated Dielectrics,” *Contrib. to Plasma Phys.*, vol. 47, no. 4–5, pp. 360–367, Jul. 2007.
- [38] A. Ferrer, D. Jaque, J. Siegel, A. R. de la Cruz, and J. Solís, “Origin of the refractive index modification of femtosecond laser processed doped phosphate glass,” *J. Appl. Phys.*, vol. 109, no. 9, p. 093107, May 2011.
- [39] V. R. Bhardwaj, P. B. Corkum, D. M. Rayner, C. Hnatovsky, E. Simova, and R. S. Taylor, “Stress in femtosecond-laser-written waveguides in fused silica,” *Opt. Lett.*, vol. 29, no. 12, p. 1312, 2004.
- [40] D. Rayner, A. Naumov, and P. Corkum, “Ultrashort pulse non-linear optical absorption in transparent media,” *Opt. Express*, vol. 13, no. 9, pp. 3208–17, 2005.

- [41] S. Juodkazis, H. Misawa, and I. Maksimov, “Thermal accumulation effect in three-dimensional recording by picosecond pulses,” *Appl. Phys. Lett.*, vol. 85, no. 22, pp. 5239–5241, 2004.
- [42] S. Gross and M. J. Withford, “Ultrafast-laser-inscribed 3D integrated photonics: Challenges and emerging applications,” *Nanophotonics*, vol. 4, no. 1, pp. 332–352, 2015.
- [43] S. Gross *et al.*, “Ultrafast Laser Inscription in Soft Glasses: A Comparative Study of Athermal and Thermal Processing Regimes for Guided Wave Optics,” *Int. J. Appl. Glas. Sci.*, vol. 3, no. 4, pp. 332–348, 2012.
- [44] C. B. Schaffer, A. Brodeur, J. F. García, and E. Mazur, “Micromachining bulk glass by use of femtosecond laser pulses with nanojoule energy,” *Opt. Lett.*, vol. 26, no. 2, p. 93, 2001.
- [45] D. Tan, K. N. Sharafudeen, Y. Yue, and J. Qiu, “Femtosecond laser induced phenomena in transparent solid materials: Fundamentals and applications,” *Progress in Materials Science*, vol. 76, no. September 2015, pp. 154–228, 2016.
- [46] T. Q. Jia *et al.*, “Ultraviolet-infrared femtosecond laser-induced damage in fused silica and CaF₂ crystals,” *Phys. Rev. B - Condens. Matter Mater. Phys.*, vol. 73, no. 5, pp. 1–9, 2006.
- [47] M. Lenzner *et al.*, “Femtosecond Optical Breakdown in Dielectrics,” *Phys. Rev. Lett.*, vol. 80, no. 18, pp. 4076–4079, May 1998.
- [48] J. L. Archambault, L. Reekie, and P. S. J. Russell, “100% reflectivity Bragg reflectors

- produced in optical fibres by single excimer laser pulses,” *Electron. Lett.*, vol. 29, no. 5, p. 453, 1993.
- [49] J. Burghoff, S. Nolte, and A. Tünnermann, “Origins of waveguiding in femtosecond laser-structured LiNbO₃,” *Appl. Phys. A Mater. Sci. Process.*, vol. 89, no. 1, pp. 127–132, 2007.
- [50] A. Rodenas and A. K. Kar, “High-contrast step-index waveguides in borate nonlinear laser crystals by 3D laser writing,” *Opt. Express*, vol. 19, no. 18, pp. 17820–33, 2011.
- [51] J. R. Macdonald, R. R. Thomson, N. D. Psaila, S. J. Beecher, H. T. Bookey, and A. K. Kar, “Ultrafast laser inscription of low loss waveguides in polycrystalline ZnSe,” *2010 23rd Annu. Meet. IEEE Photonics Soc. PHOTINICS 2010*, vol. 35, no. 23, pp. 56–57, 2010.
- [52] H. T. Bookey *et al.*, “Femtosecond laser inscription of low insertion loss waveguides in Z-cut lithium niobate,” *IEEE Photonics Technol. Lett.*, vol. 19, no. 12, pp. 892–894, 2007.
- [53] R. R. Thomson, S. Campbell, I. J. Blewett, A. K. Kar, and D. T. Reid, “Optical waveguide fabrication in z-cut lithium niobate (LiNbO₃) using femtosecond pulses in the low repetition rate regime,” *Appl. Phys. Lett.*, vol. 88, no. 11, p. 111109, Mar. 2006.
- [54] M. Bazzan and C. Sada, “Optical waveguides in lithium niobate: Recent developments and applications,” *Appl. Phys. Rev.*, vol. 2, no. 4, 2015.
- [55] J. Lv, Y. Cheng, W. Yuan, X. Hao, and F. Chen, “Three-dimensional femtosecond laser fabrication of waveguide beam splitters in LiNbO₃ crystal,” *Opt. Mater. Express*, vol. 5, no. 6, p. 1274, Jun. 2015.

- [56] J. Burghoff, C. Grebing, S. Nolte, and A. Tünnermann, "Efficient frequency doubling in femtosecond laser-written waveguides in lithium niobate," *Appl. Phys. Lett.*, vol. 89, no. 8, pp. 14–17, 2006.
- [57] L. Gui, B. Xu, and T. C. Chong, "Microstructure in lithium niobate by use of focused femtosecond laser pulses," *IEEE Photonics Technol. Lett.*, vol. 16, no. 5, pp. 1337–1339, 2004.
- [58] A. Ródenas *et al.*, "Refractive index change mechanisms in femtosecond laser written ceramic Nd:YAG waveguides: Micro-spectroscopy experiments and beam propagation calculations," *Appl. Phys. B Lasers Opt.*, vol. 95, no. 1, pp. 85–96, 2009.
- [59] G. A. Torchia, A. Rodenas, A. Benayas, E. Cantelar, L. Roso, and D. Jaque, "Highly efficient laser action in femtosecond-written Nd:yttrium aluminum garnet ceramic waveguides," *Appl. Phys. Lett.*, vol. 92, no. 11, p. 111103, Mar. 2008.
- [60] A. G. Okhrimchuk, A. V. Shestakov, I. Khrushchev, and J. Mitchell, "Depressed cladding, buried waveguide laser formed in a YAG:Nd³⁺ crystal by femtosecond laser writing," *Opt. Lett.*, vol. 30, no. 17, p. 2248, 2005.
- [61] J. Siebenmorgen, K. Petermann, G. Huber, K. Rademaker, S. Nolte, and A. Tünnermann, "Femtosecond laser written stress-induced Nd:Y₃Al₅O₁₂ (Nd:YAG) channel waveguide laser," *Appl. Phys. B Lasers Opt.*, vol. 97, no. 2, pp. 251–255, 2009.
- [62] A. Benayas *et al.*, "Thermally resistant waveguides fabricated in Nd:YAG ceramics by crossing femtosecond damage filaments," *Opt. Lett.*, vol. 35, no. 3, pp. 330–332, 2010.
- [63] S. J. Beecher, R. R. Thomson, D. T. Reid, N. D. Psaila, M. Ebrahim-Zadeh, and A. K.

- Kar, "Strain field manipulation in ultrafast laser inscribed BiB₃O₆ optical waveguides for nonlinear applications," *Opt. Lett.*, vol. 36, no. 23, pp. 4548–4550, 2011.
- [64] N. Dong *et al.*, "Self-frequency-doubling of ultrafast laser inscribed neodymium doped yttrium aluminum borate waveguides," *Appl. Phys. Lett.*, vol. 98, no. 18, pp. 2–4, 2011.
- [65] C. Grivas, C. Corbari, G. Brambilla, and P. G. Lagoudakis, "Tunable, continuous-wave Ti:sapphire channel waveguide lasers written by femtosecond and picosecond laser pulses," *Opt. Lett.*, vol. 37, no. 22, p. 4630, 2012.
- [66] V. Apostolopoulos *et al.*, "Femtosecond irradiation induced refractive-index changes and channel waveguiding in bulk Ti³⁺:sapphire," in *Conference on Lasers and Electro-Optics/International Quantum Electronics Conference and Photonic Applications Systems Technologies*, 2004, p. CMY4.
- [67] A. Benayas, D. Jaque, B. McMillen, and K. P. Chen, "High repetition rate UV ultrafast laser inscription of buried channel waveguides in Sapphire: Fabrication and fluorescence imaging via ruby R lines," *Opt. Express*, vol. 17, no. 12, pp. 10076–10081, 2009.
- [68] F. M. Bain *et al.*, "Ultrafast laser inscribed Yb:KGd(WO₄)₂ and Yb:KY(WO₄)₂ channel waveguide lasers," *Opt. Express*, vol. 17, no. 25, pp. 22417–22422, 2009.
- [69] S. M. Eaton *et al.*, "Raman gain from waveguides inscribed in KGd(WO₄)₂ by high repetition rate femtosecond laser," *Appl. Phys. Lett.*, vol. 92, no. 8, p. 081105, Feb. 2008.
- [70] S. Zhang *et al.*, "Second harmonic generation of periodically poled potassium titanyl phosphate waveguide using femtosecond laser pulses "Fabrication and characterization of periodically poled lithium niobate waveguide using femtosecond laser pulses," *Opt. Express*, vol. 16, no. 18, p. 14181, 2008.

- [71] N. Dong *et al.*, “Femtosecond laser writing of multifunctional optical waveguides in a Nd:YVO₄+KTP hybrid system,” *Opt. Lett.*, vol. 36, no. 6, pp. 975–977, 2011.
- [72] W. F. Silva *et al.*, “Femtosecond-laser-written, stress-induced Nd:YVO₄ waveguides preserving fluorescence and Raman gain,” *Opt. Lett.*, vol. 35, no. 7, pp. 916–918, 2010.
- [73] Y. Tan *et al.*, “70% slope efficiency from an ultrafast laser-written Nd:GdVO₄ channel waveguide laser,” *Opt. Express*, vol. 18, no. 24, pp. 24994–24999, 2010.
- [74] D. Beckmann, D. Esser, and J. Gottmann, “Characterization of channel waveguides in Pr:YLiF₄ crystals fabricated by direct femtosecond laser writing,” *Appl. Phys. B Lasers Opt.*, vol. 104, no. 3, pp. 619–624, 2011.
- [75] R. Li *et al.*, “Femtosecond-laser-written superficial cladding waveguides in Nd:CaF₂ crystal,” *Opt. Laser Technol.*, vol. 92, pp. 163–167, Jul. 2017.
- [76] F. Hoffmann, “The Fascination of Crystals and Symmetry,” <https://crystalsymmetry.wordpress.com/yt/>, Germany, 2014.
- [77] W. Massa, *Crystal Structure Determination*. Berlin, Heidelberg: Springer, Berlin, Heidelberg.
- [78] T. S. Narasimhamurty, *Photoelastic and Electro-Optic Properties of Crystals*, no. 1. Boston, MA: Springer US, 1981.
- [79] J. F. Nye, *Physical properties of crystals : their representation by tensors and matrices*. Oxford: Calderon Press, 1957.

-
- [80] M. de Jong *et al.*, “Charting the complete elastic properties of inorganic crystalline compounds,” *Sci. Data*, vol. 2, no. 1, p. 150009, Dec. 2015.
- [81] R. M. Hazen and L. W. Finger, “Calcium fluoride as an internal pressure standard in high-pressure crystallography,” *J. Appl. Crystallogr.*, vol. 14, no. 4, pp. 234–236, Aug. 1981.
- [82] Y.-Y. Qi, Z.-G. Li, Y. Cheng, X.-R. Chen, and G.-F. Ji, “First-Principles Study of Electronic, Elastic, and Optical Properties of Yb:CaF₂ Crystals,” *Zeitschrift für Naturforsch. A*, vol. 70, no. 11, pp. 889–896, Oct. 2015.
- [83] “Crystal structure Calcium fluoride,” 2008. [Online]. Available: <https://www.acs.org/content/acs/en/molecule-of-the-week/archive/c/calcium-fluoride.html>.
- [84] D. G. Cahill and R. O. Pohl, “Lattice Vibrations and Heat Transport in Crystals and Glasses,” *Annu. Rev. Phys. Chem.*, vol. 39, no. 1, pp. 93–121, 1988.
- [85] T. Tomie, I. Okuda, and M. Yano, “Three-photon absorption in CaF₂ at 248.5 nm,” *Appl. Phys. Lett.*, vol. 55, no. 4, pp. 325–327, Jul. 1989.
- [86] Y.-Y. Qi, T. Zhang, Y. Cheng, X.-R. Chen, D.-Q. Wei, and L.-C. Cai, “Lattice dynamics and thermal conductivity of calcium fluoride via first-principles investigation,” *J. Appl. Phys.*, vol. 119, p. 095103, 2016.
- [87] M. Siebold *et al.*, “Broad-band regenerative laser amplification in ytterbium-doped calcium fluoride (Yb:CaF₂),” *Appl. Phys. B*, vol. 89, no. 4, pp. 543–547, Dec. 2007.
- [88] V. Petit, J. L. Doualan, P. Camy, V. Ménard, and R. Moncorgé, “CW and tunable laser

- operation of Yb³⁺ doped CaF₂,” *Appl. Phys. B*, vol. 78, no. 6, pp. 681–684, Apr. 2004.
- [89] D. N. Papadopoulos *et al.*, “High Repetition Rate Yb:CaF₂ Multipass Amplifiers Operating in the 100-mJ Range,” *IEEE J. Sel. Top. Quantum Electron.*, vol. 21, no. 1, pp. 464–474, Jan. 2015.
- [90] G. MacHinet *et al.*, “High-gain amplification in Yb:CaF₂ crystals pumped by a high-brightness Yb-doped 976 nm fiber laser,” *Appl. Phys. B Lasers Opt.*, vol. 111, no. 3, pp. 495–500, 2013.
- [91] J. H. Burnett, Z. H. Levine, and E. L. Shirley, “Intrinsic birefringence in calcium fluoride and barium fluoride,” *Phys. Rev. B - Condens. Matter Mater. Phys.*, vol. 64, no. 24, pp. 17–21, 2001.
- [92] M. Weber, *Handbook of Optical Materials*, vol. 19, no. 5. CRC Press, 2002.
- [93] T. D. Shoji *et al.*, “Ultra-low-noise monolithic mode-locked solid-state laser,” *Optica*, vol. 3, no. 9, p. 995, 2016.
- [94] A. I. Ryskin *et al.*, “Stabilization of high-temperature disorder of fluorine sublattice by quenching in calcium fluoride crystals,” *J. Fluor. Chem.*, vol. 200, pp. 109–114, 2017.
- [95] S. Kroesen, W. Horn, J. Imbrock, and C. Denz, “Electro-optical tunable waveguide embedded multiscan Bragg gratings in lithium niobate by direct femtosecond laser writing,” *Opt. Express*, vol. 22, no. 19, p. 23339, 2014.
- [96] Y. Liao *et al.*, “Electro-optic integration of embedded electrodes and waveguides in

- LiNbO₃ using a femtosecond laser,” *Opt. Lett.*, vol. 33, no. 19, p. 2281, 2008.
- [97] S. Ringleb, K. Rademaker, S. Nolte, and A. Tünnermann, “Monolithically integrated optical frequency converter and amplitude modulator in LiNbO₃ fabricated by femtosecond laser pulses,” *Appl. Phys. B Lasers Opt.*, vol. 102, no. 1, pp. 59–63, 2011.
- [98] Y. Ren, J. R. Vázquez de Aldana, F. Chen, and H. Zhang, “Channel waveguide lasers in Nd:LGS crystals,” *Opt. Express*, vol. 21, no. 5, pp. 6503–8, 2013.
- [99] Y. Jia, C. Cheng, J. R. V. De Aldana, and F. Chen, “Three-dimensional waveguide splitters inscribed in Nd:YAG by femtosecond laser writing: Realization and laser emission,” *J. Light. Technol.*, vol. 34, no. 4, pp. 1328–1332, 2016.
- [100] J. Siebenmorgen, T. Calmano, K. Petermann, and G. Huber, “Highly efficient Yb:YAG channel waveguide laser written with a femtosecond-laser,” *Opt. Express*, vol. 18, no. 15, p. 16035, 2010.
- [101] T. Calmano *et al.*, “Characterization of an Yb:YAG ceramic waveguide laser, fabricated by the direct femtosecond-laser writing technique,” *Appl. Phys. B*, vol. 103, no. 1, pp. 1–4, 2011.
- [102] T. Calmano, J. Siebenmorgen, O. Hellmig, K. Petermann, and G. Huber, “Nd:YAG waveguide laser with 1.3 W output power, fabricated by direct femtosecond laser writing,” *Appl. Phys. B Lasers Opt.*, vol. 100, no. 1, pp. 131–135, 2010.
- [103] T. Calmano, M. Ams, P. Dekker, M. J. Withford, and C. Kränkel, “Hybrid single longitudinal mode Yb:YAG waveguide laser with 1.6 W output power,” *Opt. Mater. Express*, vol. 7, no. 8, p. 2777, 2017.

- [104] T. Calmano, A.-G. Paschke, S. Müller, C. Kränkel, and G. Huber, “Curved Yb:YAG waveguide lasers, fabricated by femtosecond laser inscription,” *Opt. Express*, vol. 21, no. 21, pp. 25501–25508, 2013.
- [105] T. Calmano *et al.*, “Diode pumped high power operation of a femtosecond laser inscribed Yb:YAG waveguide laser [Invited],” *Opt. Mater. Express*, vol. 1, no. 3, p. 428, 2011.
- [106] J. Siebenmorgen, T. Calmano, K. Petermann, and G. Huber, “Highly efficient Yb:YAG channel waveguide laser written with a femtosecond-laser,” *Opt. Express*, vol. 18, no. 15, pp. 16035–16041, 2010.
- [107] T. Calmano, A.-G. Paschke, S. Müller, C. Kränkel, and G. Huber, “Q-Switched Operation of a fs-Laser Written Nd:YAG/Cr⁴⁺:YAG monolithic waveguide laser,” in *Lasers, Sources, and Related Photonic Devices*, 2012, p. IF2A.4.
- [108] A. Okhrimchuk, V. Mezentsev, A. Shestakov, and I. Bennion, “Low loss depressed cladding waveguide inscribed in YAG:Nd single crystal by femtosecond laser pulses,” *Opt. Express*, vol. 20, no. 4, pp. 3832–43, 2012.
- [109] A. G. Okhrimchuk *et al.*, “Waveguide-saturable absorber fabricated by femtosecond pulses in YAG:Cr⁴⁺ crystal for Q-switched operation of Yb-fiber laser,” *Opt. Lett.*, vol. 34, no. 24, pp. 3881–3883, 2009.
- [110] A. G. Okhrimchuk and P. a. Obraztsov, “11-GHz waveguide Nd:YAG laser CW mode-locked with single-layer graphene,” *Sci. Rep.*, vol. 5, p. 11172, 2015.
- [111] A. Rodenas *et al.*, “Direct laser writing of near-IR step-index buried channel waveguides

- in rare earth doped YAG,” *Opt. Lett.*, vol. 36, no. 17, p. 3395, 2011.
- [112] Y. Ren, G. Brown, A. Ródenas, S. Beecher, F. Chen, and A. K. Kar, “Mid-infrared waveguide lasers in rare-earth-doped YAG,” *Opt. Lett.*, vol. 37, no. 16, p. 3339, 2012.
- [113] H. Liu, Y. Jia, J. Rodríguez, V. De Aldana, D. Jaque, and F. Chen, “Femtosecond laser inscribed cladding waveguides in Nd: YAG ceramics: Fabrication, fluorescence imaging and laser performance,” *Opt. Express*, vol. 20, no. 17, pp. 24994–24999, 2012.
- [114] A. Ródenas *et al.*, “Refractive index change mechanisms in femtosecond laser written ceramic Nd:YAG waveguides: Micro-spectroscopy experiments and beam propagation calculations,” *Appl. Phys. B Lasers Opt.*, vol. 95, no. 1, pp. 85–96, 2009.
- [115] R. Graf, A. Fernandez, M. Dubov, H. J. Brueckner, B. N. Chichkov, and A. Apolonski, “Pearl-chain waveguides written at megahertz repetition rate,” *Appl. Phys. B Lasers Opt.*, vol. 87, no. 1, pp. 21–27, 2007.
- [116] A. Arriola *et al.*, “Mid-infrared astrophotonics: study of ultrafast laser induced index change in compatible materials,” *Opt. Mater. Express*, vol. 7, no. 3, p. 698, 2017.
- [117] Y. Ren *et al.*, “Switchable single-dual-wavelength Yb,Nd:CaF₂ waveguide lasers operating in continuous-wave and pulsed regimes,” *Opt. Mater. Express*, vol. 8, no. 6, p. 1633, 2018.
- [118] B. H. Babu, T. Billotte, C. Lyu, B. Poumellec, M. Lancry, and X.-T. Hao, “Study of femtosecond laser writing in the bulk of Nd³⁺, Y³⁺ co-doped CaF₂ crystals,” *OSA Contin.*, vol. 2, no. 1, p. 151, 2019.
- [119] W. Gebremichael, I. B. Manek-Hönninger, Y. G. Petit, S. Rouzet, C. Hönninger, and L.

- Canioni, “Direct laser writing of double track waveguides inside calcium fluoride crystals (Conference Presentation),” in *Laser Applications in Microelectronic and Optoelectronic Manufacturing (LAMOM) XXIII*, 2018, p. 30.
- [120] J.-P. Bérubé, J. Lapointe, A. Dupont, M. Bernier, and R. Vallée, “Femtosecond laser inscription of depressed cladding single-mode mid-infrared waveguides in sapphire,” *Opt. Lett.*, vol. 44, no. 1, p. 37, Jan. 2019.
- [121] F. He *et al.*, “Three-dimensional patterning in transparent materials with spatiotemporally focused femtosecond laser pulses,” in *Optoelectronic Imaging and Multimedia Technology III, Proc. SPIE*, 2014, vol. 9273, no. November, p. 927316.
- [122] B. Poumellec, M. Lancry, J.-C. Poulin, and S. Ani-Joseph, “Non reciprocal writing and chirality in femtosecond laser irradiated silica,” *Opt. Express*, vol. 16, no. 22, p. 18354, 2008.
- [123] W. Yang, P. G. Kazansky, and Y. P. Svirko, “Non-reciprocal ultrafast laser writing,” *Nat. Photonics*, vol. 2, no. 2, pp. 99–104, 2008.
- [124] I. Snetkov, A. Vyatkin, O. Palashov, and E. Khazanov, “Drastic reduction of thermally induced depolarization in CaF₂ crystals with [111] orientation,” *Opt. Express*, vol. 20, no. 12, p. 13357, 2012.
- [125] K. Genevrier *et al.*, “Polarization and Crystal-Orientation Dependency of Thermal Effects in Cryogenically Cooled Yb:CaF₂,” 2016, vol. 2016, p. AM5A.6.
- [126] U. Levy, S. Derevyanko, and Y. Silberberg, *Light Modes of Free Space*, 1st ed., vol. 61. Elsevier B.V., 2016.

-
- [127] B. E. A. Saleh and M. C. Teich, *Fundamentals of Photonics*, vol. 5. New York, USA: John Wiley & Sons, Inc., 1991.
- [128] J. I. Vukusic, “Optical Fiber Communications: Principles and Practice,” *Opt. Acta Int. J. Opt.*, vol. 33, no. 6, pp. 685–685, Jun. 1986.
- [129] K. Okamoto, *Fundamentals of Optical Waveguides*, Second Edi. Elsevier, 2006.
- [130] P. Sutton, “Introduction to Fourier Optics,” *Quantum Semiclassical Opt. J. Eur. Opt. Soc. Part B*, vol. 8, no. 5, p. 491, Oct. 1996.
- [131] K. Sugioka, “Progress in ultrafast laser processing and future prospects,” *Nanophotonics*, vol. 6, no. 2, pp. 393–413, Jan. 2017.
- [132] F. Chen and J. R. Vázquez de Aldana, “Three-dimensional femtosecond laser micromachining of dielectric crystals for photonic waveguiding applications,” in *Pacific Rim Laser Damage, Proc. SPIE*, 2015, p. 95320M.
- [133] Y. A. Vlasov and S. J. McNab, “Losses in single-mode silicon-on-insulator strip waveguides and bends,” *Opt. Express*, vol. 12, no. 8, p. 1622, 2004.
- [134] T. Feuchter and C. Thirstrup, “High precision planar waveguide propagation loss measurement technique using a Fabry-Perot cavity,” *Photonics Technol. Lett. IEEE*, vol. 6, no. 10, pp. 1244–1247, 1994.
- [135] Y. Okamura, S. Yoshinaka, and S. Yamamoto, “Measuring mode propagation losses of integrated optical waveguides: a simple method,” *Appl. Opt.*, vol. 22, no. 23, p. 3892, 1983.

- [136] J. Canny, “A Computational Approach to Edge Detection,” *IEEE Trans. Pattern Anal. Mach. Intell.*, vol. PAMI-8, no. 6, pp. 679–698, 1986.
- [137] E. Hecht, *Optics*, 4th Editio. New York, USA: Addison Wesley Longman, 2002.
- [138] T. Calmano and S. Muller, “Crystalline Waveguide Lasers in the Visible and Near-Infrared Spectral Range,” *IEEE J. Sel. Top. Quantum Electron.*, vol. 21, no. 1, p. 1602213, 2015.
- [139] A. Benayas *et al.*, “Ultrafast laser writing of optical waveguides in ceramic Yb:YAG: A study of thermal and non-thermal regimes,” *Appl. Phys. A Mater. Sci. Process.*, vol. 104, no. 1, pp. 301–309, 2011.
- [140] G. Della Valle, R. Osellame, and P. Laporta, “Micromachining of photonic devices by femtosecond laser pulses,” *J. Opt. a-Pure Appl. Opt.*, vol. 11, no. 1, p. 013001, 2009.
- [141] J. Qi *et al.*, “Fabrication of polarization-independent single-mode waveguides in lithium niobate crystal with femtosecond laser pulses,” *Opt. Mater. Express*, vol. 6, no. 8, p. 2554, 2016.
- [142] P. Barritault, M. Brun, P. Labeye, O. Lartigue, J.-M. Hartmann, and S. Nicoletti, “Mlines characterization of the refractive index profile of SiGe gradient waveguides at 215 μm ,” *Opt. Express*, vol. 21, no. 9, p. 11506, 2013.
- [143] P. K. Tien and R. Ulrich, “Theory of Prism–Film Coupler and Thin-Film Light Guides,” *J. Opt. Soc. Am.*, vol. 60, no. 10, p. 1325, 1970.

-
- [144] A. Neyer, "Direct measurement of refractive index profiles of Ti:LiNbO₃ slab waveguides," *Proc. Third Eur. Conf.*, no. ECIO'85, pp. 67–70, 1985.
- [145] L. Mccaughan and E. E. Bergmann, "Index Distribution of Optical Waveguides from Their Mode Profile," *J. Light. Technol.*, vol. 1, no. 1, pp. 241–244, 1983.
- [146] K. Morishita, "Index Profiling of Three-Dimensional Optical Waveguides by the Propagation-Mode Near-Field Method," *J. Light. Technol.*, vol. 4, no. 8, pp. 1120–1124, 1986.
- [147] C. Zhang, N. Dong, J. Yang, F. Chen, J. R. Vázquez de Aldana, and Q. Lu, "Channel waveguide lasers in Nd:GGG crystals fabricated by femtosecond laser inscription," *Opt. Express*, vol. 19, no. 13, pp. 12503–12508, 2011.
- [148] Y. Jia, N. Dong, F. Chen, J. R. V. De Aldana, and S. Zhou, "Ridge waveguide lasers in Nd: GGG crystals produced by swift carbon ion irradiation and femtosecond laser ablation," *Opt. Express*, vol. 20, no. 9, pp. 9763–9768, 2012.
- [149] S. Aknoun, P. Bon, J. Savatier, B. Wattellier, and S. Monneret, "Quantitative retardance imaging of biological samples using quadriwave lateral shearing interferometry," *Opt. Express*, vol. 23, no. 12, p. 16383, 2015.
- [150] P. Bon, G. Maucort, B. Wattellier, and S. Monneret, "Quadriwave lateral shearing interferometry for quantitative phase microscopy of living cells," *Opt. Express*, vol. 17, no. 15, p. 13080, 2009.
- [151] P. Bon, S. Aknoun, S. Monneret, and B. Wattellier, "Enhanced 3D spatial resolution in quantitative phase microscopy using spatially incoherent illumination," *Opt. Express*, vol. 22, no. 7, p. 8654, 2014.

- [152] D. Schmitt and T. Weiland, “2D and 3D computations of eigenvalue problems,” *IEEE Trans. Magn.*, vol. 28, no. 2, pp. 1793–1796, Mar. 1992.
- [153] T. Weiland, “On the unique numerical solution of Maxwellian Eigenvalue Problems in Three Dimensions,” *Part. Accel.*, vol. 17, pp. 227–242, 1985.
- [154] Z. Zhu and T. Brown, “Full-vectorial finite-difference analysis of microstructured optical fibers,” *Opt. Express*, vol. 10, no. 17, pp. 853–64, Aug. 2002.
- [155] J.-P. Bérubé, J. Lapointe, A. Dupont, M. Bernier, and R. Vallée, “Femtosecond laser inscription of depressed cladding single-mode mid-infrared waveguides in sapphire,” *Opt. Lett.*, vol. 44, no. 1, p. 37, Jan. 2019.